Precision measurements with high-energy neutrino beams

Janet M. Conrad and Michael H. Shaevitz

Department of Physics, Columbia University, New York, New York 10027

Tim Bolton

Department of Physics, Kansas State University, Manhattan, Kansas 66506-2601

Neutrino-scattering measurements offer a unique tool for probing the electroweak and strong interactions as described by the standard model. Electroweak measurements are accessible through the comparison of neutrino neutral- and charged-current scattering. These measurements are complementary to other electroweak measurements due to differences in the radiative corrections both within and outside the standard model. Neutrino-scattering measurements also provide a precise method for measuring the $F_2(x,Q^2)$ and $xF_3(x,Q^2)$ structure functions. The predicted Q^2 evolution can be used to test perturbative quantum chromodynamics as well as to measure the strong-coupling constant α_s and the valence, sea, and gluon parton distributions. In addition, neutrino charm production, which can be determined from the observed dimuon events, allows the strange-quark sea to be investigated along with measurements of the CKM matrix element $|V_{cd}|$ and the charm quark mass. [S0034-6861(98)00504-2]

CONTENTS

I. INTRODUCTION

Neutrino-scattering experiments have strongly influenced the development of particle physics over the past three decades. Neutrinos couple to other particles only through the weak interaction, which is well determined in the standard model. For this reason, neutrino-scattering measurements can be used as a probe to measure many of the standard model parameters or to look beyond the standard model for indications of new physics. The effects of the small interaction cross section for neutrinos has been overcome by modern experiments through the use of high-intensity beams coupled with massive detectors which give luminosities in the range of $10^{36}\ \mathrm{cm}^{-2}\,\mathrm{s}^{-1}$. Data samples in excess of one million events are now available, which allow measurements of strong and electroweak parameters comparable in precision to other fixed-target and collider determinations.

This review addresses three broad physics topics accessible to high-energy neutrino deep-inelastic scattering experiments: nucleon structure functions and tests of quantum chromodynamics (QCD) (Sec. III), neutrino-induced charm production (Sec. IV), and electroweak physics with neutrino beams (Sec. V). We begin with a brief introduction to the relevant kinematics and cross-section formulae and follow with a summary of experiments whose results we review (Sec. I.A). We then devote an entire section to the difficult problem of normalizing data through the determination of the neutrino flux and total cross section (Sec. II). The main physics sections follow.

The experiments we review date from roughly 1980 until the present, although in some cases we reach back further if the results are still of interest. We also restrict ourselves to high-energy measurements; thus we emphasize the CERN SPS and Fermilab Main Ring and Tevatron programs. Earlier and lower-energy experiments have been reviewed elsewhere (Barrish, 1978; Fisk and Sciulli, 1982; Diemoz *et al.*, 1986; Mishra and Sciulli, 1989; Winter, 1990).

A. Kinematic formalism

The tree-level diagram for charged-current neutrino-nucleon (νN) scattering is shown in Fig. 1. A neutrino (or antineutrino) with incoming four-momentum k_1 scatters from a quark or antiquark in the nucleon via exchange of a W^+ (W^-) boson with four-momentum q.

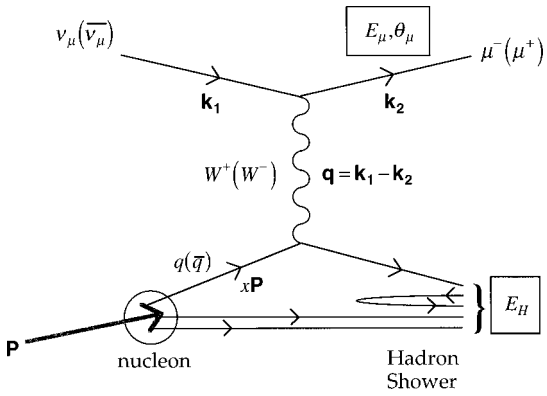

FIG. 1. The first-order Feynman diagram for deep-inelastic neutrino scattering. (E_H is the energy of the final-state hadron system and is referred to as E_{had} in the text.)

In the laboratory frame, the variables that can be measured in this interaction are the energy and angles of the outgoing muon, E_μ, θ_μ, ϕ_μ, and the energy and angles of the outgoing hadrons, E_{had}, θ_{had}, ϕ_{had}. In practice, experiments are located sufficiently far from the neutrino production point that the neutrino beam can be considered, to high accuracy, parallel to the z axis; thus the difficult-to-measure hadron scattering angles are not necessary to specify the kinematics. In the laboratory frame, the four-vectors of the event can then be written in terms of E_μ, θ_μ, ϕ_μ, E_{had}, and M, the proton mass:[1]

$$
\begin{aligned}
&k_1=(E_\nu,0,0,E_\nu),\\
&k_2=(E_\mu,E_\mu\sin\theta_\mu\cos\phi_\mu,E_\mu\sin\theta_\mu\sin\phi_\mu,E_\mu\cos\theta_\mu),\\
&p=(M,0,0,0),\\
&q=k_1-k_2,
\end{aligned}
\tag{1}
$$

with $E_\nu=E_\mu+E_{\mathrm{had}}$.

Useful invariant quantities that describe the interaction are

$$
\begin{aligned}
&\nu=(p\cdot q)/M \quad \text{(energy transfer)},\\
&y=p\cdot q/p\cdot k_1 \quad \text{(inelasticity)},\\
&Q^2=-q^2 \quad \text{(negative squared 4-momentum)},\\
&x=Q^2/(2p\cdot q) \quad \text{(Bjorken scaling variable)},\\
&W^2=(p+q)^2\\
&\qquad \text{(squared invariant mass of final state)}.
\end{aligned}
\tag{2}
$$

In the laboratory, these reduce to

$$
\begin{aligned}
&\nu=E_{\mathrm{had}},\\
&y=\frac{E_{\mathrm{had}}}{E_{\mathrm{had}}+E_\mu},\\
&Q^2=(E_{\mathrm{had}}+E_\mu)E_\mu\theta_\mu^2,
\end{aligned}
$$

[1]We use the conventional units of high-energy physics in this review: $\hbar=c=1$, and all dimensionful quantities are in GeV unless otherwise indicated.

$$x=\frac{(E_{\rm had}+E_\mu)E_\mu\theta_\mu^2}{2ME_{\rm had}},$$

$$W^2=M^2+2ME_{\rm had}+Q^2, \tag{3}$$

using the small-angle approximation and neglecting the muon mass.

If the interaction is with nuclear constituents, generically called "partons," then the kinematic variables x, ν, and Q^2 acquire further physical interpretations. The Bjorken scaling variable x can be considered the fraction of the nucleon's momentum carried by a struck parton in the infinite momentum frame, where the parton mass and transverse momentum are negligible. The four-momentum of the struck parton is $xp+q$. Then $(xp+q)^2=0$ leads to the relation $x=Q^2/(2p\cdot q)$, where $x^2p^2=x^2M^2\ll Q^2$ was used. The variables ν and Q^2 are related to the ability to resolve "free" partons within the nucleon. To resolve partons, the interaction time scale t must be sufficiently small to guarantee that the partons do not interact, while the spatial resolution must be significantly smaller than the nucleon size D. The time scale on which the free partons can then be resolved is given by the uncertainty principle: $\Delta E\approx\nu\gg 1/t$ or $\Delta p\approx\sqrt{Q^2}\gg 1/D$.

In principle, for a given beam of neutrino energy E_ν, the accessible kinematic region is bounded by

$$\frac{m_\mu^4}{8xME_\nu^2}\leqslant\nu\leqslant\frac{E_\nu}{(1+2Mx/E_\nu)}\rightarrow E_\nu,$$

$$\frac{m_\mu^4}{8xME_\nu^3}\leqslant y\leqslant\frac{1}{(1+2Mx/E_\nu)}\rightarrow 1,$$

$$\frac{m_\mu^4}{4E_\nu^2}\leqslant Q^2\leqslant\frac{2ME_\nu x}{(1+2Mx/E_\nu)}\rightarrow 2ME_\nu x,$$

$$\frac{m_\mu^2}{2ME_\nu}\leqslant x\leqslant 1. \tag{4}$$

The lower limits are given to leading order in the final-state lepton mass and can always be set to 0 for the high energies considered; the arrows indicate the high-energy limits of the upper range on the variables, which, for most purposes, are also sufficient. In practice, experimental restrictions to select regions of high acceptance and small corrections reduce the available range. The accessible kinematic range of a given experiment can be described in the plane of any two of the above variables. The resulting kinematic range in the x and Q^2 plane is shown in Fig. 2 for four high-statistics, deep-inelastic neutrino-scattering experiments.

In the case of neutral-current scattering, the scattered neutrino is not reconstructed; all event information must be inferred from the hadron shower. The important kinematic quantities are identical to the charged-current case up to small effects due to the muon mass.

B. The neutrino-scattering cross section

The cross section may be written using Fermi's golden rule:

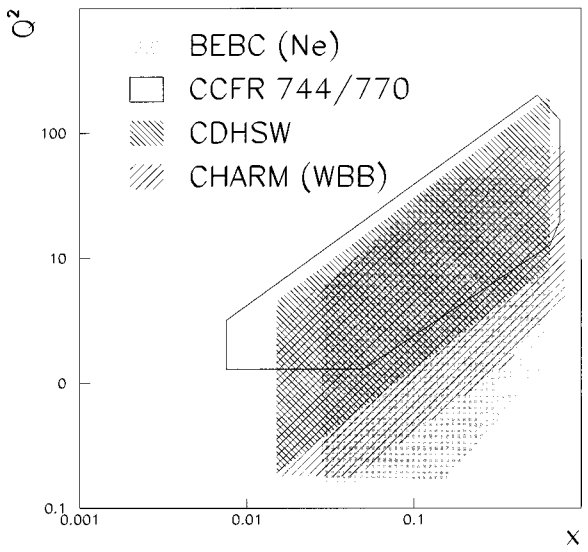

FIG. 2. The kinematic regions accessible to the high-statistics neutrino experiments discussed in this review.

$$d\sigma=d\Gamma\frac{|\mathcal{M}|^2}{\Phi}, \tag{5}$$

where $\mathcal{M}$ is the invariant amplitude for the scattering, $d\Gamma$ is the phase-space factor, that is, the density of final states per incident particle, and Φ is the incident-particle flux. The heart of the physics is in the squared matrix element, and we shall concentrate on this. The deep-inelastic scattering invariant amplitude at the Born level can be factored into a leptonic vertex, a hadronic vertex, and the connecting propagator. In the case of ν charged-current scattering, this is

$$\mathcal{M}=\sqrt{2}G_F\overline{u}(k')\gamma^\alpha(1-\gamma_5)u(k)\frac{1}{1+Q^2/M_W^2}\times\langle X|J_\alpha^{Weak}|p,\sigma\rangle. \tag{6}$$

The square of this matrix element can be written in terms of two tensors describing each vertex:

$$|\mathcal{M}|^2=\frac{2G_F^2}{(1+Q^2/M_W^2)}L_{\alpha\beta}W^{\alpha\beta}. \tag{7}$$

The leptonic tensor is

$$L_{\alpha\beta}=[\overline{u}(k)\gamma_\alpha(1-\gamma_5)u(k')][\overline{u}(k')\gamma_\beta(1-\gamma_5)u(k)]$$
$$=8[k'_\alpha k_\beta+k'_\beta k_\alpha-(k\cdot k'-m_\mu^2)g_{\alpha\beta}\mp i\epsilon_{\alpha\beta\gamma\delta}k^\gamma k'^\delta],$$

where $\epsilon_{\alpha\beta\gamma\delta}$ is the totally antisymmetric tensor: $+1$ for ϵ_{0123} and all even permutations, -1 for all odd permutations, and 0 if two or more indices are the same. The most general form for the hadronic vertex must be constructed from the only two independent vectors, p and q, and the identity matrix:

$$W^{\alpha\beta}=-g^{\alpha\beta}W_1+\frac{p^\alpha p^\beta}{M^2}W_2-\frac{i\epsilon^{\alpha\beta\gamma\delta}p_\gamma q_\delta}{2M^2}W_3 \tag{8}$$

$$+\frac{q^\alpha q^\beta}{M^2}W_4+\frac{p^\alpha q^\beta+p^\beta q^\alpha}{M^2}W_5 \tag{9}$$

$$+i\frac{p^\alpha q^\beta - p^\beta q^\alpha}{2M^2}W_6. \tag{10}$$

Evaluating $L_{\alpha\beta}W^{\alpha\beta}$, we find

(i) the W_6 is eliminated because $L_{\alpha\beta}W^{\alpha\beta} \rightarrow \epsilon^{\alpha\beta\gamma\delta}k_\alpha k'_\beta(p^\alpha q^\beta - q^\alpha p^\beta)=0$, where $q=k-k'$ is used.

(ii) the W_4 and W_5 terms are neglected because they are proportional to the mass of the lepton: $q^\alpha L_{\alpha\beta} \propto m_\ell^2 k^\beta$ and $q^\beta L_{\alpha\beta} \propto m_\ell^2 k^\alpha$.

This leaves three remaining terms, proportional to W_1, W_2, and W_3.

If the nucleon has constituents that are resolvable for $\sqrt{Q^2}, \nu \gg M$, then these W terms would be functions of the kinematic variables ν and Q^2:

$$W_1 \rightarrow W_1(Q^2,\nu),$$

$$\text{where } 2MW_1(Q^2,\nu)=\frac{Q^2}{2M\nu}\delta\left(1-\frac{Q^2}{2M\nu}\right),$$

$$W_2 \rightarrow W_2(Q^2,\nu), \quad \text{where } \nu W_2(Q^2,\nu)=\delta\left(1-\frac{Q^2}{2M\nu}\right),$$

$$W_3 \rightarrow W_3(Q^2,\nu), \quad \text{where } \nu W_3(Q^2,\nu)=\delta\left(1-\frac{Q^2}{2M\nu}\right).$$

In the deep-inelastic scattering regime, where $Q^2 \rightarrow \infty$ and $\nu \rightarrow \infty$ with $x=Q^2/2M\nu$ fixed, "Bjorken scaling" is expected, and the W functions are rewritten as the traditional structure functions:

$$MW_1(Q^2,\nu) \rightarrow F_1(x),$$

$$\nu W_2(Q^2,\nu) \rightarrow F_2(x),$$

$$\nu W_3(Q^2,\nu) \rightarrow F_3(x).$$

However, experimentally Bjorken scaling is observed to be violated, leading to Q^2 dependences of the structure functions. This can be interpreted as direct evidence for QCD, as discussed in the following section.

Often, the cross-section formula is written in terms of the structure function $R_L(x,Q^2)$ rather than $F_1(x,Q^2)$. $R_L(x,Q^2)$ can be interpreted as the ratio of the longitudinal to transverse virtual-boson absorption cross section. The two structure functions are related by

$$R_L(x,Q^2)=\frac{\sigma_L}{\sigma_T} = \frac{F_2(x,Q^2)(1+4M^2x^2/Q^2)-2xF_1(x,Q^2)}{2xF_1(x,Q^2)}. \tag{11}$$

In this review, we shall describe the cross section for scattering from an isoscalar target in terms of the structure functions F_2, xF_3, and R_L defined by

$$\frac{d^2\sigma^{\nu(\bar\nu)N}}{dx\,dy}=\frac{G_F^2 M E_\nu}{\pi(1+Q^2/M_W^2)^2}\left[F_2^{\nu(\bar\nu)N}(x,Q^2)\times\left(\frac{y^2+(2Mxy/Q)^2}{2+2R_L^{\nu(\bar\nu)N}(x,Q^2)}+1-y-\frac{Mxy}{2E_\nu}\right)\pm xF_3^{\nu(\bar\nu)N}y\left(1-\frac{y}{2}\right)\right], \tag{12}$$

where the $\pm$ is $+(-)$ for $\nu(\bar\nu)$ scattering.

Analogous functions $F_2^{e(\mu)N}(x,Q^2)$ and $R_L^{e(\mu)N}(x,Q^2)$ appear in the cross section for deep-inelastic charged-lepton scattering. The function $xF_3(x,Q^2)$ appears only in the cross section for the weak interaction because it originated from the parity-violating term in the product of the leptonic and hadronic tensors.

C. Neutrino scattering from partons

The cross section presented in Eq. (12) makes no assumptions about the underlying structure of the hadron involved in the interaction. However, the results of early experiments provided clear evidence that the neutrinos were interacting with quarks in the nucleon (Perkins, 1975). This section discusses neutrino-parton scattering at the simplest level. The interpretation of the cross section within QCD is discussed in greater detail in Sec. III.

The "naive" quark-parton model describes the structure functions in terms of momentum-weighted parton distribution functions (PDFs). For neutrino interactions with the partons in the proton,

$$F_{2,QPM}^{\nu p}(x)=2x[d(x)+\bar u(x)+s(x)+\bar c(x)], \tag{13}$$

$$xF_{3,QPM}^{\nu p}(x)=2x[d(x)-\bar u(x)+s(x)-\bar c(x)]. \tag{14}$$

In these equations u, d, s, and c indicate the PDFs for up, down, strange, and charm quarks, respectively, in the proton. These PDFs describe the probability that the interacting parton carries a fraction x of the proton's four-momentum.[2] Note that because the neutrino interacts via emission of a W^+, only the negatively charged quarks contribute to the interaction.

In a similar way, neutron structure functions can be written in terms of the proton PDFs by invoking isospin invariance,

$$F_{2,QPM}^{\nu n}(x)=2x[u(x)+\bar d(x)+s(x)+\bar c(x)], \tag{15}$$

$$xF_{3,QPM}^{\nu n}(x)=2x[u(x)-\bar d(x)+s(x)-\bar c(x)]. \tag{16}$$

When neutron and proton structure functions are combined for an isoscalar target, one obtains

$$F_{2,QPM}^{\nu N}(x)=x[u(x)+d(x)+2s(x)+\bar u(x)+\bar d(x)+2\bar c(x)], \tag{17}$$

[2]This interpretation of x is an approximation that we employ due to its intuitive appeal and because, at high energies, this definition of x differs negligibly from its more rigorous interpretation as a light-cone variable (see Sec. I.A).

$$xF_{3,QPM}^{\nu N}(x)=x[u(x)+d(x)+2s(x) -\overline{u}(x)-\overline{d}(x)-2\overline{c}(x)]. \quad (18)$$

Antineutrino interactions proceed via emission of a W^- boson. Therefore only the positively charged quarks contribute. Following the prescription for the neutrino case and assuming that $s(x)=\overline{s}(x)$ and $c(x)=\overline{c}(x)$, we obtain the antineutrino structure functions

$$F_{2,QPM}^{\overline{\nu}N}(x)=F_{2,QPM}^{\nu N}(x), \quad (19)$$

$$xF_{3,QPM}^{\overline{\nu}N}(x)=xF_{3,QPM}^{\nu N}(x)-4x[s(x)-c(x)]. \quad (20)$$

In this review $xF_3=\frac{1}{2}(xF_3^{\nu N}+xF_3^{\overline{\nu}N})$ will refer to the average of the neutrino and antineutrino measurements; $\Delta(xF_3)=xF_3^{\nu N}-xF_3^{\overline{\nu}N}$ will indicate the difference between the neutrino and antineutrino structure functions. We use F_2 to refer to either neutrino or antineutrino scattering because the structure functions are equivalent.

In the quark-parton model, the interaction probability for each PDF depends on the square of the charge associated with the interaction. In the weak interaction, this is unity. For charged-lepton scattering mediated by a virtual photon,

$$F_{2,QPM}^{e(\mu)N}(x)=\frac{5}{18}x\left\{u(x)+d(x)+\overline{u}(x)+\overline{d}(x) +\frac{2}{5}[s(x)+\overline{s}(x)]+\frac{8}{5}[c(x)+\overline{c}(x)]\right\}. \quad (21)$$

The structure-function definitions of the quark-parton model must be modified to accommodate strong interactions between the partons and to include mass effects. Within the framework of QCD, discussed in Sec. III.A.1, the parton distributions acquire a Q^2 dependence. Small transverse-momentum quark-gluon interactions may occur at the time of the scatter. The probability that the interaction resolves such processes depends on Q^2 and modifies the parton distributions, leading to a Q^2 dependence known as "scaling violations." Thus at leading order in QCD, the structure functions are

$$F_{2,LO}=\sum_{i=u,d..} xq_i(x,Q^2)+x\overline{q_i}(x,Q^2), \quad (22)$$

$$xF_{3,LO}=\sum_{i=u,d..} xq_i(x,Q^2)-x\overline{q_i}(x,Q^2). \quad (23)$$

(In the above equations and subsequent sections, q and $\overline{q}$ are introduced as the generic notation for the various parton distributions in the proton.) Parton mass effects further modify the parton distributions, an effect called "slow rescaling" (see Sec. IV.B), which leads to $q(x,Q^2)\rightarrow q(\xi,Q^2)$, where ξ depends on the mass of the parton.

To leading order, $R_L(x,Q^2)=0$, and the Callan-Gross relation (Callan and Gross, 1969), $F_2(x,Q^2)=2xF_1(x,Q^2)$, is valid because spin-$\frac{1}{2}$ massless quarks cannot absorb a longitudinally polarized virtual boson, reverse direction in the center of momentum frame, and still conserve helicity. A nonzero $R_L(x,Q^2)$ is a manifestation of nonperturbative and higher-order QCD effects and is described in Sec. III.A.1. In all formulations that we are aware of, the structure function R_L is the same for neutrino and antineutrino scattering.

These tree-level expressions can be used to point out some of the interesting information accessible from νN scattering:

(i) $F_2^{\nu N}(x,Q^2)$ and $F_2^{\overline{\nu}N}(x,Q^2)$ measure the sum of quark and antiquark PDFs in the nucleon.

(ii) The average of $xF_3^{\nu N}(x,Q^2)$ and $xF_3^{\overline{\nu}N}(x,Q^2)$ measure the valence-quark PDFs,

$$xF_3=u(x,Q^2)+d(x,Q^2)-\overline{u}(x,Q^2)-\overline{d}(x,Q^2) \equiv u_V(x,Q^2)+d_V(x,Q^2). \quad (24)$$

(iii) $F_2^{\nu N}(x,Q^2)$ and $F_2^{e(\mu)N}(x,Q^2)$ together confirm the fractional electric charge assignment to the quarks and provide sensitivity to the strange-quark PDF.

(iv) The difference $\Delta(xF_3)=xF_3^{\nu N}(x,Q^2)-xF_3^{\overline{\nu}N}(x,Q^2)$ is sensitive to the strange and charm quark content in the nucleon.

Neutrino scattering from d or s quarks can produce a c quark in the final state, which can be identified by either a lifetime or, more easily, a semileptonic decay tag. This ability to tag final-state charm permits a series of unique strong and electroweak tests, including the direct measurement of $s(x,Q^2)$ and $\overline{s}(x,Q^2)$, extraction of the Cabibbo-Kobayashi-Maskawa (CKM) elements V_{cd} and V_{cs}, a measurement of the mass of the charm quark m_c, and a sensitive probe of the dynamics of leading-order and next-to-leading-order QCD. This physics is described in Sec. IV.

Neutral-current νN scattering is described by a closely related set of structure functions. While these can be measured, the primary interest in this process lies in inclusive cross-section measurements for electroweak physics tests of the standard model. The detailed description of νN neutral-current scattering will be discussed in Sec. V.

D. Overview of experiments

This section provides an overview of the beams and experimental apparatus used in deep-inelastic neutrino scattering. Table I summarizes the data samples obtained by the high-precision neutrino experiments that are discussed below.

1. CCFR experiment

The CCFR collaboration has performed a series of experiments at Fermi National Accelerator Laboratory (hereafter, "Fermilab") using the Lab E neutrino detector. This paper includes results from data runs E616, E701, E744, and E770, spanning a period from 1979 through 1988. A new experiment, E815, is presently taking data.

TABLE I. Overview of high precision neutrino experiments. Target refers to the bulk of the material in the experimental target. Total events vary for each type of analysis depending on cuts; the numbers here are approximate.

Experiment	Beam energy (GeV)	Target	ν events	$\bar{\nu}$ events	Flux method	Ref.
CCFR (E616)	30–300	Fe	150 000	23 000	Secondary monitoring	MacFarlane *et al.*, 1984
CCFR (E701)	30–300	Fe	35 000	7 000	Secondary monitoring y-int.	Auchincloss *et al.*, 1990
CCFR (E744/770)	30–360	Fe	1 300 000	270 000	Fixed ν_0	Selyman *et al.*, 1997a,1997b
CDHSW	20–212	Fe	640 000	550 000	Iterative y fit	Berge *et al.*, 1991
CHARM	10–160	$CaCO_2$	116 000	6000	Secondary monitoring	Allaby *et al.*, 1988
CHARM II	5–100	Glass	750 000 Q.E.	1 300 000 Q.E.	$\sigma^{\nu}_{\rm tot}$	Geiregat *et al.*, 1993
BEBC	15–160	Ne (D_2)	15 000 (12 000)	10 000 (11 000)	Iterative y fit	Allport *et al.*, 1989

The E616 and E701 experiments took data using the Fermilab dichromatic neutrino beam. The primary protons had an energy of 400 GeV. The secondary beam traversed a 60-m chain of magnets and collimators, which selected pions and kaons based on energy and charge. The neutrino energy spectrum from this beam has two relatively narrow peaks from the pion and kaon decays, which gives the beam its dichromatic nature.

The most recent results from the CCFR Collaboration come from the 1985 (E744) and 1987 (E770) fixed-target runs at Fermilab. The CCFR neutrino beam resulted from decays of pions and kaons produced in interactions of the 800-GeV FNAL proton beam with a beryllium target. The FNAL Quadrupole Triplet beam line, which had no sign-selecting magnets, was used to transport the secondaries. This resulted in a wideband beam of neutrinos and antineutrinos, with a relatively uniform energy spectrum ranging in energy up to 600 GeV. This beam resulted in approximately 86.4% ν_μ, 11.3% $\bar{\nu}_\mu$, and 2.3% ν_e and $\bar{\nu}_e$ events.

Neutrino events were observed in the Lab E neutrino detector (Sakamoto *et al.*, 1990), shown in Fig. 3. The detector is constructed as a target calorimeter followed by a toroid muon spectrometer. The 690-ton calorimeter consists of eighty-four 3 m×3 m×10 cm iron plates interspersed with scintillators and drift chambers, with a measured hadronic energy resolution $\sigma/E_{\rm had} = 0.89/\sqrt{E_{\rm had}}$. The toroid spectrometer has five sets of drift chambers for muon tracking as well as hodoscopes for triggering; its momentum resolution is limited by multiple Coulomb scattering to $\Delta p/p = 0.11$. The detector was periodically calibrated by a test beam of pions and muons.

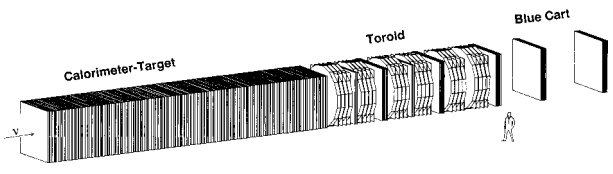

FIG. 3. Schematic representation of the CCFR detector. The neutrino beam travels from left to right. The target calorimeter is on the left and the muon spectrometer (toroid) is on the right. (The ''Blue Cart'' refers to downstream chambers that extend the angle measurement for precise momentum determination.)

NuTeV (Bolton *et al.*, 1990), the next generation of deep-inelastic neutrino scattering experiments at Fermilab, began taking data in May, 1996. NuTeV has modified the beam line to select the sign of the charged pions and kaons (Bernstein *et al.*, 1994). The resulting beam is almost purely ν_μ or $\bar{\nu}_\mu$, depending on the sign selection. The enhanced purity of the antineutrino sample will improve a number of QCD studies, especially those concerned with small-x physics. Separate running will also permit the first high-statistics simultaneous measurements of the electroweak mixing parameter $\sin^2\theta_W$ and neutral-to-charged-current coupling strength ratio ρ. The substantially upgraded Lab E neutrino detector is continuously calibrated with a test beam of pions, electrons, or muons throughout the running. The new test beam also provides a broader range of hadron and muon energies than were available to CCFR.

2. The CDHSW experiment

The CDHSW experiment (Holder *et al.*, 1978a, 1978b; Abromowicz *et al.*, 1981) measured the total neutrino cross section using 100-, 160-, and 200-GeV narrow-band neutrino beams and performed precision electroweak and structure-function measurements with a wideband beam during the early 1980s. Primary protons from the CERN SPS were used to produce secondary pions and kaons. For the wideband running, the secondary beam was focused using a magnetic horn. Depending on the sign selection set by the magnetic field, the tertiary beam consisted mainly of neutrinos or antineutrinos. An antineutrino contamination in a neutrino beam will result in single-muon events with a muon that has positive rather than negative charge. This contamination is therefore called the ''wrong-sign'' background. The fraction of wrong-sign background events for CDHSW neutrino running was 2.3%. For antineutrino running, the wrong-sign background was 17% (Berge *et al.*, 1991).

This experiment used the upgraded CDHS detector, which consisted of toroidally magnetized iron plates

sandwiched between planes of scintillator and drift chambers. The calorimeter was 3.75 m in diameter, 21 m long, and had a total mass of approximately 1100 tons. The hadronic energy resolution of the detector varied, depending on the segmentation of the iron, from $\sigma/E_{\rm had}\approx 0.58/\sqrt{E_{\rm had}}$ to $0.70/\sqrt{E_{\rm had}}$. The momentum of the muon was determined by the bend in the magnetic field, with an average resolution of 9%. The field of the toroid was chosen to focus μ^+ or μ^- based on the setting of the magnetic horn.

3. The CHARM experiment

The CHARM experiment (Jonker *et al.*, 1982) made high-precision measurements using the 160-GeV narrow-band neutrino and antineutrino beam and the wideband beam at the CERN SPS during the early 1980s. The CHARM detector was composed of a fine-grained calorimeter followed by a muon spectrometer. The calorimeter consisted of 78 marble plates ($CaCO_3$), hence an isoscalar target, of dimension 3 m×3 m×8 cm. Scintillation counters, proportional drift tubes, and streamer tubes were located between the plates. The fiducial mass of the target was approximately 90 tons, with a mean target density of 1.38 g/cm^3. The muon spectrometer consisted of an iron toroid spectrometer surrounded by a magnetized iron frame and instrumented with proportional chambers. The calorimeter was calibrated with electron and pion beams.

The CHARM apparatus could resolve hadronic shower angle as well as the shower energy, muon energy, and angle. The detector was capable of measuring hadronic shower energies as low as 2 GeV. The resulting hadronic energy resolution was $\sigma/E_{\rm had}=0.49\%/\sqrt{E_{\rm had}}$. The hadronic shower angle could be measured with a resolution function given by $\sigma(\theta_{\rm had})\approx\sqrt{0.16/E_{\rm had}+0.2/E_{\rm had}}$, where $E_{\rm had}$ is measured in GeV. The muon momentum resolution, $\Delta p/p$, was 15% to 20% on average. The CHARM detector had a resolution on muon angle of 5 mrad at 50 GeV and 2 mrad at 150 GeV. The vertex position resolution was 3 cm at $E_{\rm had}=50$ GeV. The neutrino energy resolution was ≈10% to 20%.

4. The CHARM II experiment

The CHARM II experiment (Geiregat *et al.*, 1993) collected data during the period 1987–1991, using the wideband neutrino beam described in the above CDHSW experiment section. This experiment was optimized for detection of electrons. The combination of low-Z target material and high granularity was used to achieve good electron-hadron separation and shower angle resolution. The detector's target was composed of 48-mm (0.5 radiation length)-thick plates of glass, with a total mass of 690 tons. Interspersed between the plates were streamer tubes with 1-cm wire spacing, which provided digital hit information. The tube layers were also instrumented with 2-cm-wide pickup strips, which were read out as analog signals. Between every five sets of plates and streamer tubes were scintillation counters.

Test beams of electrons, pions, and muons were used to calibrate the detector. The electromagnetic energy resolution from the digital readout of the streamer tubes was $\sigma/E=0.09+0.15/\sqrt{E}$, where the energy is in GeV. The resolution for hadronic showers from neutrino interactions using the streamer tubes was $\sigma_{\rm had}/E_{\rm had}=0.02+0.52/\sqrt{E_{\rm had}}$. The electromagnetic energy resolution using the pickup strips was $\sigma/E=0.05+0.23/\sqrt{E}$. The muon spectrometer consisted of magnetized iron toroids instrumented with scintillation counters and drift chambers. The resolution was $\Delta p/p=13\%$ at 20 GeV.

5. The BEBC experiment

The Big European Bubble Chamber (BEBC) experiment (Baruzzi *et al.*, 1983) ran with both narrow-band and wideband beams provided by the CERN SPS during a series of experiments that began in the late 1970s and continued during the 1980s using a variety of targets. This review discusses results mainly from the high-statistics BEBC runs with deuterium (WA25) and neon (WA59) targets. The cryogenic bubble chamber had a 10-m^3 fiducial volume surrounded by a 3-T superconducting magnet and supplemented with a two-plane, 150-m^2 external muon identification system.

II. NEUTRINO FLUX AND TOTAL-CROSS-SECTION MEASUREMENTS

Accurate measurement of the flux of neutrinos in a beam is necessary for all of the analyses discussed in this review. Flux monitoring is a difficult task for a beam of neutral weakly interacting particles; hence indirect methods must be employed. Flux determinations can be based on measurements of the secondary pion and kaon rates. This secondary measurement technique has been used for narrow-band neutrino beams to determine the total scattering cross section as a function of energy for neutrinos and antineutrinos. The measured total cross sections can then be combined with the observed number of events in a wideband beam to determine the neutrino flux as a function of energy. Alternatively, wideband neutrino beam fluxes can be obtained from fits to the y distribution of the data or integration over the observed low-y events. These methods rely upon the relation between the cross section, flux ($\Phi_{\nu,\bar\nu}$), and number of events ($N_{\nu,\bar\nu}$):

$$\frac{dN_{\nu,\bar\nu}}{dy}=\Phi_{\nu,\bar\nu}(E_\nu)\,\frac{d\sigma^{\nu,\bar\nu}}{dy}. \tag{25}$$

The flux measurement errors are among the largest systematic errors associated with neutrino precision measurements; therefore an extended discussion of the subject is presented here.

A. Absolute flux determination

Neutrino beams result mainly from the decay of secondary pions and kaons, which are produced when a proton interacts with a target. Most pion and kaon de-

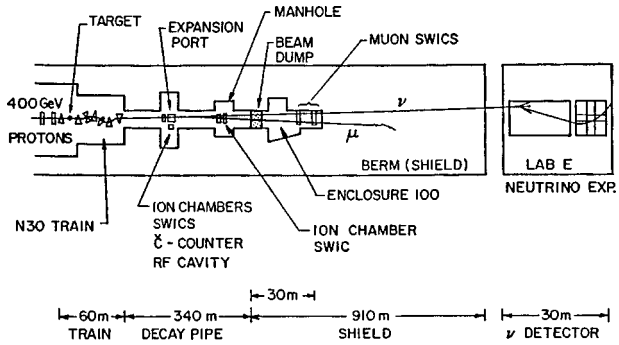

FIG. 4. Schematic of the CCFR E616 neutrino beam line and beam-monitoring ports. The figure has not been drawn to scale.

cays are two-body, thus the neutrino energy and flux can be determined using kinematic constraints if the integrated intensity, energy, and spatial distribution of the secondary beam are known. This method is most successful when applied to narrow-band beams and was employed by many experiments to measure structure functions and the total cross section. These experiments include CCFR E616 (Auchincloss *et al.*, 1990; Oltman *et al.*, 1992), CDHSW (Berge *et al.*, 1987), and CHARM (Allaby *et al.*, 1988).

The primary and secondary beams are monitored using a variety of detectors, including RF cavities, toroids, Cerenkov counters, segmented wire ionization chambers, and hodoscopes. Redundancy is important to reduce the systematic errors in the measurement of the secondary beams. As an example of a typical experimental setup, Fig. 4 shows a schematic diagram of the CCFR E616 beam line including the locations of the various monitoring devices. As an additional constraint to reduce errors, the CHARM and CDHSW collaborations also monitored the muon flux from the tertiary beam.

Two uncertainties associated with this technique result from three-body decays of kaons and pion or kaon decays that occur before the momentum selection magnets (Auchincloss *et al.*, 1990). The former are largely from $K\rightarrow\pi\mu\nu$, which can be corrected using a Monte Carlo simulation of the neutrino flux. The latter can be measured directly by placing a dump in the beam after the magnet, thus absorbing the sign-selected secondary beam. All interactions in this mode would result from neutrinos produced in decays before the magnet.

B. Relative flux

The structure-function measurements described in Sec. III are very sensitive to the accurate determination of the relative flux among the various energy bins and between neutrinos and antineutrinos. Therefore it is important to establish methods of normalizing between neutrino energy bins that have small systematic errors and little dependence on assumptions of nucleon structure. These methods are crucial for experiments using wide-band neutrino beams, where beam monitoring methods cannot provide sufficient accuracy. In a narrow-band beam, these methods can be used to test the accuracy of the measurements from secondary-beam monitoring.

The energy-dependent neutrino flux can be obtained from a Monte Carlo simulation of the beam optics combined with measurements of parent spectra. Uncertainties in the inputs to these types of simulations have led experiments to use other techniques. For example, the energy-dependent flux can be calculated from the distribution of observed neutrino and antineutrino events assuming a total cross section that rises linearly with energy. Total-cross-section measurements have shown that the rise is linear within 2 to 4% (see Sec. II.D). This method also requires an input set of structure functions in order to correct the observed events for acceptance and resolution smearing.

Other methods of flux extraction have been developed in which the events used for the flux extraction are almost independent of the events used for the structure-function measurements. The "y-intercept technique" relies on the premise that near zero hadronic energy transfer, $y=E_{\rm had}/E_\nu\rightarrow 0$, the differential inelastic cross section divided by energy is independent of energy and is the same for neutrinos and antineutrinos. The differential cross section for neutrino scattering, given by Eq. (12), in the $y\rightarrow 0$ limit reduces to

$$\left[\frac{1}{E_\nu}\frac{d\sigma^\nu}{dy}\right]_{y=0}=\left[\frac{1}{E_\nu}\frac{d\sigma^{\overline{\nu}}}{dy}\right]_{y=0}=\frac{G_F^2 M}{\pi}\int_0^1 F_2(x,Q^2\rightarrow 0)dx\approx C, \quad (26)$$

where C is a constant independent of energy. This is true independent of incident-neutrino energy or neutrino type for scattering on an isoscalar target. Thus, for each bin in energy, the flux of neutrinos or antineutrinos is given by

$$\lim_{y\rightarrow 0}\left(\frac{1}{E_\nu}\frac{dN^{\nu(\overline{\nu})}(E_\nu)}{dy}\right)=C\times\Phi^{\nu(\overline{\nu})}(E_\nu). \quad (27)$$

This method was applied by CCFR (E616) to cross-check the flux obtained from secondary-beam measurements for the determination of the neutrino total cross section.

For wideband neutrino beams, the beam energy and radial distribution are usually determined through iterating the Monte Carlo simulation of the neutrino events, successively varying the input flux and structure functions until the Monte Carlo matches the observed distribution of events. Initial distributions for the structure functions are taken from previously published results. These structure functions and initial distributions for the neutrino flux are used to generate events, which are then put through the Monte Carlo simulation of the detector. The ratio of simulated events to detected events in each x-y-E_ν bin provides the correction factors for the flux and structure functions for the next iteration. Variations on this method are used by both the CDHSW and the CCFR Collaborations.

The CCFR E744/E770 "fixed-ν_0 method" provides a specific example of one iterative technique for extracting the relative flux (Seligman *et al.*, 1997a, 1997b). This method exploits the y dependence of the data to obtain the flux. The relationships of Eqs. (25) and (12) can be extended to small ν as a polynomial in terms of $y = \nu/E_\nu$,

$$\frac{dN_{\nu,\bar{\nu}}}{d\nu} = \Phi(E_\nu)[A_{\nu,\bar{\nu}} + B_{\nu,\bar{\nu}}(\nu/E_\nu) + (C_{\nu,\bar{\nu}}/2)(\nu/E_\nu)^2], \tag{28}$$

where A, B, and C are given by

$$A = \frac{G_F^2 M}{\pi} \int_0^1 F_2(x,Q^2)dx,$$

$$B = -\frac{G_F^2 M}{\pi} \int_0^1 [F_2(x,Q^2) \mp xF_3(x,Q^2)]dx,$$

$$C = B - \frac{G_F^2 M}{\pi} \int_0^1 F_2(x,Q^2)\tilde{R}(x,Q^2)dx, \tag{29}$$

with

$$\tilde{R}(x,Q^2) \equiv \frac{1+2Mx/\nu}{1+R_L(x,Q^2)} - \frac{Mx}{\nu} - 1. \tag{30}$$

Except for small variations due to the scaling violations of the structure functions, A, B, and C are relatively independent of ν and E_ν. Integrating Eq. (28), we find that the number of events with $\nu < \nu_0$ for a given energy, $N^{\text{Obs}}_{\nu<\nu_0}(E_\nu)$, is given by

$$N^{\text{Obs}}_{\nu<\nu_0}(E_\nu) = \Phi(E_\nu) \int_0^{\nu_0} d\nu\, A \times \left[1 + \frac{\nu}{E_\nu}\frac{B}{A} - \frac{\nu^2}{2E_\nu^2}\left(\frac{B}{A} - \frac{\int F_2 \tilde{R} dx}{\int F_2 dx}\right)\right]. \tag{31}$$

From the values of $N^{\text{Obs}}_{\nu<\nu_0}(E_\nu)$, $\Phi(E_\nu)$ can be determined for both neutrinos and antineutrinos up to an overall normalization constant. The overall normalization is determined from the world-average cross section for νFe (Sec. II.D) (Seligman *et al.*, 1997a, 1997b),

$$\sigma^{\nu Fe}/E_\nu = (0.677 \pm 0.014) \times 10^{-38} \text{ cm}^2/\text{GeV}.$$

The assumption that the integrals over the structure functions are independent of ν is only approximately true. Recall that $Q^2 = 2M\nu x$. Therefore for fixed ν, using F_2 as an example,

$$\int_0^1 F_2(x,Q^2)dx = \int_0^1 F_2(x,2M\nu x)dx \equiv F_2^{\text{int}}(\nu). \tag{32}$$

The systematic error introduced by this residual ν dependence was studied by varying the ν range from which the flux was extracted and found to be less than 0.5% (Seligman *et al.*, 1997a, 1997b).

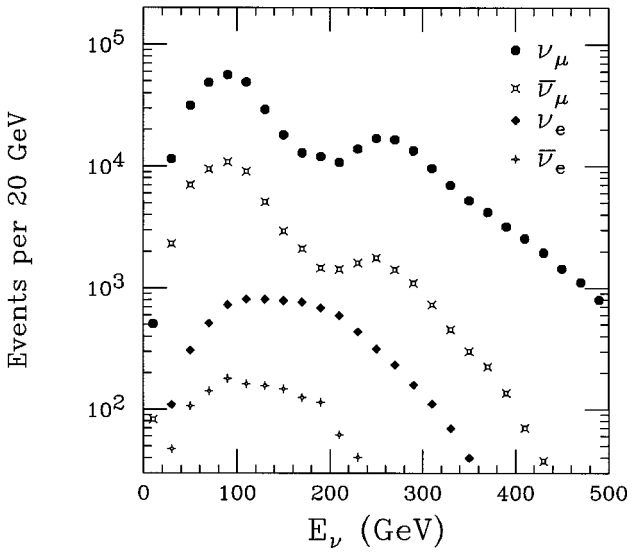

FIG. 5. The CCFR 744/770 neutrino and antineutrino event spectrum.

C. Electron neutrino flux

Most neutrino beams are composed mainly of muon-type neutrinos and antineutrinos, with a small contamination from the electron flavor. Accurate determination of this contamination is important for the precision measurement of $\sin^2\theta_W$ discussed later. The $\nu_e/\bar{\nu}_e$ flux is evaluated through detailed Monte Carlo simulations, which are tied to the direct muon-flavor flux measurements. As an example of the magnitude of the contamination, the CCFR E744/770 Monte Carlo flux determination is shown in Fig. 5 (King, 1994). As a test of the accuracy of this method, a recent analysis of the CCFR data to determine directly the total number of ν_e interactions has confirmed the Monte Carlo prediction (Romosan *et al.*, 1997).

D. Measurements of the total cross section

The total neutrino and antineutrino cross sections have been measured in a large number of experiments. For these measurements, the neutrino flux is determined by monitoring the secondary pion and kaon rates of a narrow-band beam and combining this flux with the number of observed events corrected for experimental acceptance. The number of observed events is separated into those from pion-decay neutrinos and kaon-decay neutrinos using the kinematic correlation between the neutrino energy and angle, as shown in Fig. 6.

This section reports on those experiments which have measured the total cross section to an accuracy of at least 10%. The BEBC (Bosetti *et al.*, 1982; Aderholz *et al.*, 1986), CCFR E616 (MacFarlane *et al.*, 1984), CDHSW (Berge *et al.*, 1987), CHARM (Allaby *et al.*, 1988), and CCFR E701 (Auchincloss *et al.*, 1990) results are from experiments described in detail above. Two older experiments, the 15-ft Bubble Chamber at Fermilab (Baker *et al.*, 1983; Taylor *et al.*, 1983) and FNAL

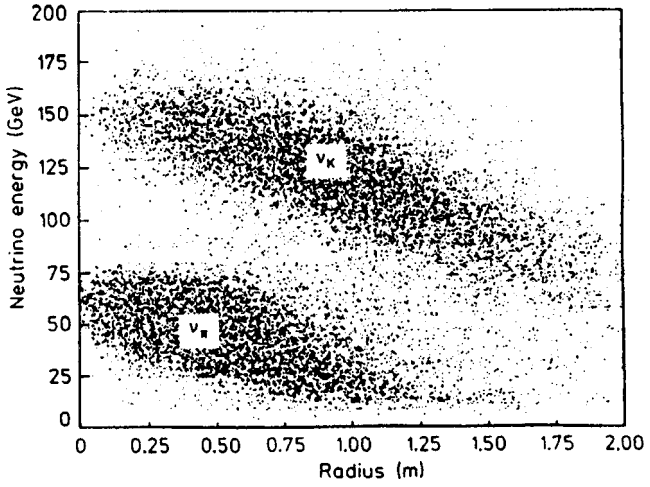

FIG. 6. Neutrino data from the CDHSW experiment for a secondary-beam energy setting of 160 GeV as a function of measured energy $E_\nu = E_{\rm had} + E_\mu$ and radial distance from the beam axis.

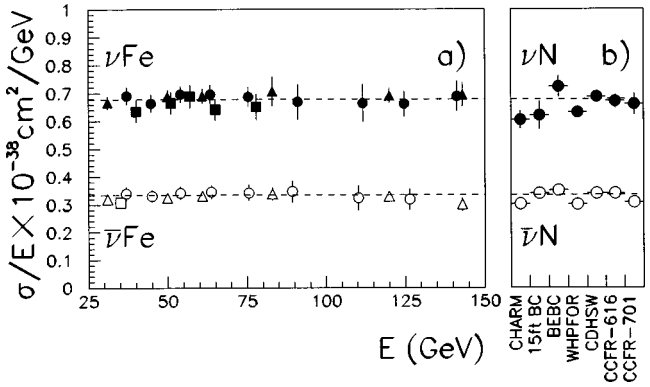

FIG. 7. Neutrino (solid) and antineutrino (open) measurements of $\sigma_{\rm tot}/E_\nu$. (a) $\sigma_{\rm tot}/E_\nu$ vs E_ν for iron targets: ○,●, CCFR E616; □,■, CCFR E701; △,▲, CDHSW. (b) Average $\sigma_{\rm tot}/E$ for a variety of targets (isoscalar corrected). Dashed lines indicate average for iron data (see text). (The error bars include both statistical and systematic errors.)

E310 (WHPFOR), a counter experiment with an iron target (Heagy *et al.*, 1981), also have results with small errors and are discussed below. All results are presented for interactions with an isoscalar target, and a correction has been applied to the iron data to compensate for the neutron excess.

A linear dependence of the total cross section on energy is expected if pointlike scattering between neutrinos and quarks dominates the scattering mechanism. This behavior is observed in the neutrino-iron total-cross-section measurements from CCFR E616 (MacFarlane *et al.*, 1984), CDHSW (Berge *et al.*, 1987), and CCFR E701 (Auchincloss *et al.*, 1990), as shown in Fig. 7. The ratio $\sigma_{\rm tot}/E_\nu$ as a function of E_ν is in agreement with a straight line with no slope for both neutrino and antineutrino interactions.

The total cross section for neutrino scattering on iron is used to provide the overall normalization of the flux for the CCFR E744/E770 experiment. Table II summarizes the isoscalar-corrected measurements for neutrino-iron experiments. The world averages for these experiments are indicated by the dashed lines in Fig. 7(a). The data from all experiments are in good agreement with these averages. The E744/E770 data also yield a measurement of $\sigma^{\bar\nu}/\sigma^{\nu} = 0.509 \pm 0.010$ (Seligman *et al.*, 1997a, 1997b), which is listed with the other measurements in Table II.

The world-average $\bar\nu/\nu$ cross-section ratio, in combination with the world-average neutrino cross section, sets the overall normalization for CCFR E744/E770 data. Given this normalization, CCFR has measured the energy dependence of $\sigma_{\rm tot}/E_\nu$ up to energies of 400 GeV. The result is shown in Fig. 8, where systematic and statistical errors have been added in quadrature. The data have been fitted to a model that allows a slope in $\sigma_{\rm tot}/E_\nu$, denoted $\varepsilon_{\nu(\bar\nu)}$ for neutrinos (antineutrinos),

$$\sigma_{\rm tot}^{\nu,\bar\nu}/E_\nu = \sigma^{\nu,\bar\nu}(1 + \varepsilon_{\nu,\bar\nu} E_\nu). \tag{33}$$

The results are

$$\varepsilon_\nu = (-2.2 \pm 0.7)\%/(100\ \text{GeV}) \quad \text{(CCFR)},$$

$$\varepsilon_{\bar\nu} = (-0.2 \pm 1.3)\%/(100\ \text{GeV}) \quad \text{(CCFR)}.$$

A small slope for the neutrino cross section is expected as a consequence of QCD and heavy-quark effects (Hinchliffe and Smith, 1977).

Figure 7(b) shows the average total-cross-section measurement for neutrino-iron targets as well as neutrino-nucleon scattering from various isoscalar targets by CHARM (Allaby *et al.*, 1988), the 15-ft Bubble Chamber (Baker *et al.*, 1983; Taylor *et al.*, 1983), and BEBC (Aderholz *et al.*, 1986; Bosetti *et al.*, 1982). The approximate average beam energy of these lower-energy measurements is 25 GeV. The results are in good agreement with the average for the high-energy neutrino-iron cross section indicated by the dashed line.

TABLE II. Measurements of the neutrino total cross section on iron. (The CHARM result has not been included in the averages since the systematic errors are correlated with CDHSW.)

Experiment	σ^{ν}/E	$\sigma^{\bar\nu}/E$	$\sigma^{\bar\nu}/\sigma^{\nu}$	Ref.
CCFR (E616)	0.669±0.024	0.340±0.020	0.499±0.025	(MacFarlane *et al.*, 1984)
CDHSW	0.686±0.020	0.339±0.009	0.495±0.010	(Berge *et al.*, 1987)
CHARM	0.686±0.020	0.335±0.011	0.488±0.013	(Allaby *et al.*, 1988)
CCFR (E701)	0.659±0.039	0.307±0.020	0.467±0.028	(Auchincloss *et al.*, 1990)
CCFR (E744/770)			0.509±0.010	(Seligman *et al.*, 1997a, 1997b)
World Ave.	0.677±0.014	0.334±0.008	0.500±0.007	

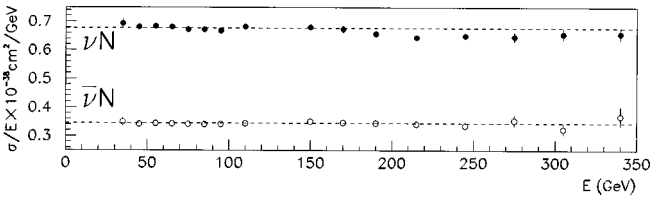

FIG. 8. $\sigma^{\nu,\overline{\nu}}/E_\nu$ for ν_μ and $\overline{\nu}_\mu$ from CCFR E744/E770. Normalization is based on the world averages given in Table II.

III. MEASUREMENTS OF NUCLEON STRUCTURE FROM INCLUSIVE SCATTERING

Precision deep-inelastic neutrino-scattering experiments provide opportunities to test QCD evolution and extract the QCD parameter Λ, which sets the scale of the strong interaction. In the kinematic regions where the structure of the nucleon can be interpreted in terms of quarks, neutrino scattering possesses high sensitivity to many individual parton distributions. Probing the nucleon with neutrinos complements charged-lepton scattering experiments, and comparisons between neutrino and charged-lepton deep-inelastic experiments provide tests of the universality of the structure functions. Global analyses that include the neutrino data and other cross-section measurements yield the best parametrizations of the individual parton distributions.

This section reviews the contributions of neutrino deep-inelastic scattering experiments to precision measurements of nucleon structure. A brief review of the theory of the structure functions is provided. Experimental techniques and issues that must be considered in the analyses are reviewed. Results of the high-precision neutrino measurements are compared between experiments and to charged-lepton scattering results. Finally, the QCD analysis of the structure functions is presented.

A. Theoretical framework

This section describes the theoretical framework in which the structure-function measurements will be interpreted. The QCD expectation is described along with a discussion of nonperturbative and nuclear effects.

1. The structure functions within QCD

The general form for the differential cross section depends upon three structure functions, F_2, R_L, and xF_3, as shown in Eq. (12). In the quark-parton model, the neutrino structure functions can be written as functions of sums and differences of the momentum-weighted quark probability densities, as described in Sec. I.C. Quantum chromodynamics modifies this parton-model interpretation in order to account for the interactions between the partons.

Within QCD, partons with higher fractional momentum may contribute to interactions at any lower x through radiation or gluon splitting. The probability that the interaction resolves such a splitting depends on Q^2, as described by the Dokshitser-Gribov-Lipatov-Altarelli-Parisi (DGLAP) equations (Gribov and Lipatov, 1972; Altarelli and Parisi, 1977; Dokshitser *et al.*, 1978; Dokshitser *et al.*, 1980):

$$\frac{dq^{NS}(x,Q^2)}{d\ \ln\ Q^2}=\frac{\alpha_S(Q^2)}{2\pi}\int_x^1\frac{dy}{y}q^{NS}(y,Q^2)P_{qq}(x/y),$$

$$\frac{dq^{S}(x,Q^2)}{d\ \ln\ Q^2}=\frac{\alpha_S(Q^2)}{2\pi}\int_x^1\frac{dy}{y}[q^{S}(y,Q^2)P^{S}_{qq}(x/y)+G(y,Q^2)P_{qG}(x/y)],$$

$$\frac{dG(x,Q^2)}{d\ \ln\ Q^2}=\frac{\alpha_S(Q^2)}{2\pi}\int_x^1\frac{dy}{y}[q^{S}(y,Q^2)P_{Gq}(x/y)+G(y,Q^2)P_{GG}(x/y)]. \tag{34}$$

The splitting functions, $P_{ij}(x/y)$, give the probability that parton j with momentum y will be resolved as parton i with momentum $x<y$. The symbols $q^{NS}=\Sigma_i(q_i-\overline{q}_i)$ and $q^S=\Sigma_i(q_i+\overline{q}_i)$ refer to the nonsinglet and singlet quark distributions, respectively. The probability of finding a gluon in the nucleon carrying a fractional momentum x is represented by $G(x,Q^2)$.

From the DGLAP equations, it can be seen that the change in the structure functions with Q^2 as a function of x depends on α_s. At next-to-leading order, α_S is given by

$$\alpha_S(Q^2)=\frac{4\pi}{\beta_0\ln(Q^2/\Lambda^2)}\left\{1-\frac{\beta_1}{\beta_0}\frac{\ln[\ln(Q^2/\Lambda^2)]}{\ln(Q^2/\Lambda^2)}\right\}, \tag{35}$$

where $\beta_0=11-2n_f/3$, $\beta_1=102-38n_f/3$, and n_f is the number of quark flavors participating in the interaction at this Q^2. The QCD parameter Λ must be introduced when the renormalization technique is applied to remove the divergences within QCD. For the discussion here, the modified minimal subtraction scheme ($\overline{\text{MS}}$) is used.

The structure function $R_L=\sigma_L/\sigma_T$ is zero in the simple parton model. However, QCD effects, such as quark-gluon bremsstrahlung and $q\overline{q}$ pair-production, introduce transverse momentum leading to a small, nonzero value of R_L, which has a predicted x and Q^2 dependence (Altarelli and Martinelli, 1978). Given well-measured quark distributions and α_S from xF_3 and F_2, a precise measurement of R_L can be a sensitive probe of the gluon distribution.

2. Nonperturbative QCD effects

Nonperturbative QCD processes that contribute to the structure-function measurements are collectively termed higher-twist effects. These effects occur at small Q^2, where the impulse approximation of scattering from massless noninteracting quarks is no longer valid. Examples include target-mass effects, diquark scattering, and other multiparton effects. Because neutrino experiments use heavy targets in order to obtain high interaction rates, nuclear effects must also be considered.

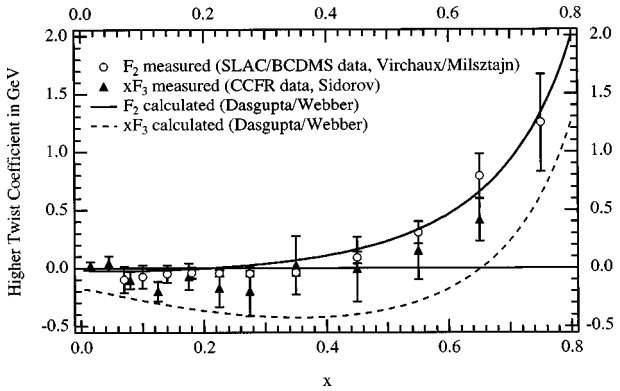

FIG. 9. Coefficients of the higher-twist parametrization. ▲, xF_3 from Sidorov (1996); open data points, F_2 from Virchaux and Milsztajn (1992); solid line, the F_2 result from Dasgupta and Webber (1996); dashed line, xF_3 result from Dasgupta and Webber (1996).

a. Target-mass and higher-twist effects

The target-mass correction (Georgi and Politzer, 1976) to the structure functions accounts for the mass of the nucleon M by rescaling the apparent fractional momentum of the quark: $x \to \xi = 2x/(1+k)$, where $k = (1+4x^2M^2/Q^2)^{\frac{1}{2}}$. The structure functions are then

$$F_2^{TMC} = \frac{x^2}{k^2}\frac{F_2^{QCD}}{\xi^2} + \frac{6M^2}{Q^2}\frac{x^3}{k^4}I_1 + \frac{12M^4}{Q^4}\frac{x^4}{k^5}I_2,$$

$$xF_3^{TMC} = \frac{x^2}{k^2}\frac{xF_3^{QCD}}{\xi^2} + \frac{2M^2}{Q^2}\frac{x^3}{k^3}I_3. \tag{36}$$

In the above equations,

$$I_1 = \int_\xi^1 du\, F_2^{QCD}(u,Q^2)/u^2,$$

$$I_2 = \int_\xi^1 du \int_u^1 dv\, F_2^{QCD}(v,Q^2)/v^2,$$

$$I_3 = \int_\xi^1 du\, xF_3^{QCD}(u,Q^2)/u^2. \tag{37}$$

For the QCD analysis presented in Sec. III.E, the structure functions are corrected to remove the target-mass effect.

The remaining higher-twist effects cannot be calculated a priori from perturbative QCD, but must be measured. Virchaux and Milsztajn (1992) compared SLAC electron-scattering and BCDMS muon-scattering measurements of F_2 to QCD expectations. Deviations were attributed entirely to higher-twist effects and were fit to the form

$$F_2^{\text{measured}}/F_2^{\text{predicted}} = (1 + C_i/Q^2). \tag{38}$$

The constants C_i calculated for each x bin are shown in Fig. 9. This determination was done using a value of α_s smaller than the current world average, which may make these higher-twist corrections too large.

The Virchaux and Milsztajn (1992) corrections are applicable to a measurement of F_2 in neutrino scattering. However, xF_3 may not have the same higher-twist corrections as F_2. Figure 9 also shows the measured higher-twist contribution extracted from the CCFR xF_3 data based on a next-to-leading-order analysis following the prescription used for F_2 (Sidorov, 1996). In addition, Fig. 9 shows the calculation by Dasgupta and Webber (1996), which includes infrared renormalon contributions. The measured higher-twist contribution to the two structure functions are consistent; however, the coefficient for the $x = 0.65$ bin of xF_3 is almost a factor of 2 lower than that for F_2. A preliminary analysis of the recent CCFR F_2 and xF_3 results also indicates higher-twist corrections that are smaller than the Virchaux and Milsztajn (1992) or Dasgupta and Webber (1996) determinations. For these reasons, the new CCFR analysis uses one-half of the Dasgupta and Webber (1996) values, with a systematic error given by repeating the analysis with no correction and with the full correction.

b. Nuclear effects in neutrino scattering

Dependence on the mass number A of the nucleus could arise from several effects:

(i) Fluctuations of the intermediate virtual boson to mesons. This might suppress the bound nucleon (iron) structure function compared to that from a free (hydrogen) or nearly free (deuterium) nucleon (Bauer *et al.*, 1978). The vector-meson-dominance model ascribes the cause of shadowing to fluctuations of the boson into mesons, leading to strong interactions near the "surface" of the nucleus. This model was developed for charged-lepton scattering, where the photon can fluctuate only into vector mesons. However, for neutrinos the W has an axial as well as a vector component. Vector- and axial-vector-meson-dominance effects are expected to affect mainly the low-x region.

(ii) Gluon recombination, which can occur in a large nucleus between partons of neighboring nucleons (Nikolaev and Zakharov, 1975; Mueller and Qiu, 1986). This leads to an A-dependent depletion of low-x partons.

(iii) The EMC effect, which denotes a suppression of the structure functions from high-A targets compared to deuterium in the $0.2 < x < 0.7$ range. Many theoretical explanations have been developed to explain the EMC effect (Geesaman *et al.*, 1995), which has been most clearly observed in charged-lepton scattering experiments. These include multiquark clusters (Krzywicki, 1976; Pirner and Vary, 1981), dynamical rescaling (Nachtman and Pirner, 1984), and nuclear-binding effects (Akulinichev *et al.*, 1985; Dunne and Thomas, 1986). In each of these models, the effect is independent of the type of boson probe, and thus is expected to appear also in neutrino scattering using high-A targets.

(iv) Fermi motion of nucleons within the nucleus,

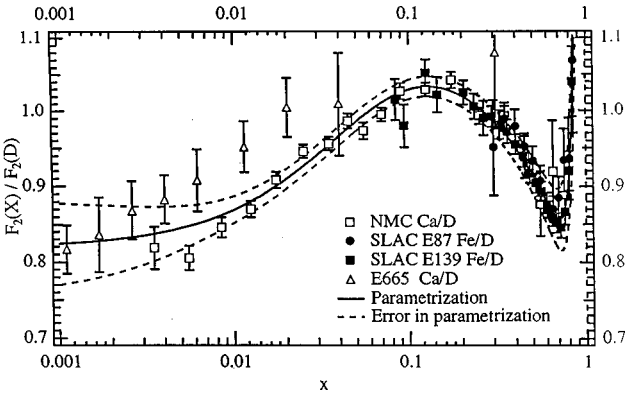

FIG. 10. Fit to the NMC (Amaudruz *et al.*, 1995), E665 (Adams *et al.*, 1995), SLAC E87 (Arnold *et al.*, 1984), and SLAC E139 (Gomez *et al.*, 1994) nuclear data. The resulting fit is used to correct the charged-lepton deuterium data for comparison with the CCFR result.

which is expected to affect nuclear targets at very high x (Bodek and Ritchie, 1981a, 1981b).

Figure 10 shows the A dependence of structure function data measured in deep inelastic charged-lepton scattering. If this A dependence is entirely attributed to effects within the nuclear target, as opposed to propagator effects, then this figure should also describe the expected nuclear dependence for neutrino scattering from a high-A target.

B. Experimental techniques for measuring xF_3 and F_2

Various experimental techniques are used to extract F_2 and xF_3 from the measured number of events. This section considers the methods used by CCFR, CDHSW, and CHARM as examples. In all cases, the assumptions concerning the longitudinal structure function R_L affect the final result and must be considered in any comparisons.

1. The CCFR measurement of F_2 and xF_3

The recent CCFR E744/E770 measurements of F_2 and xF_3 provide an example of a technique of extracting structure functions in neutrino experiments with very small systematic errors. The resulting measurements demonstrate the high precision that recent neutrino experiments have been able to achieve. As a result of this precision, neutrino experiments now quantitatively test QCD at next-to-leading order.

The structure functions F_2 and xF_3 are extracted from νN and $\overline{\nu} N$ differential cross sections, given the fluxes $(\Phi_\nu, \Phi_{\overline{\nu}})$ determined by the method described in Sec. II (Seligman *et al.*, 1997a, 1997b). The number of events in each x and Q^2 bin is related to the differential cross section by

$$N = \rho L N_A \int_{x\ \text{bin}} \int_{Q^2\ \text{bin}} \left[\int_{\text{all energies}} \frac{d^2\sigma}{dx\, dQ^2} \Phi(E) dE \right], \tag{39}$$

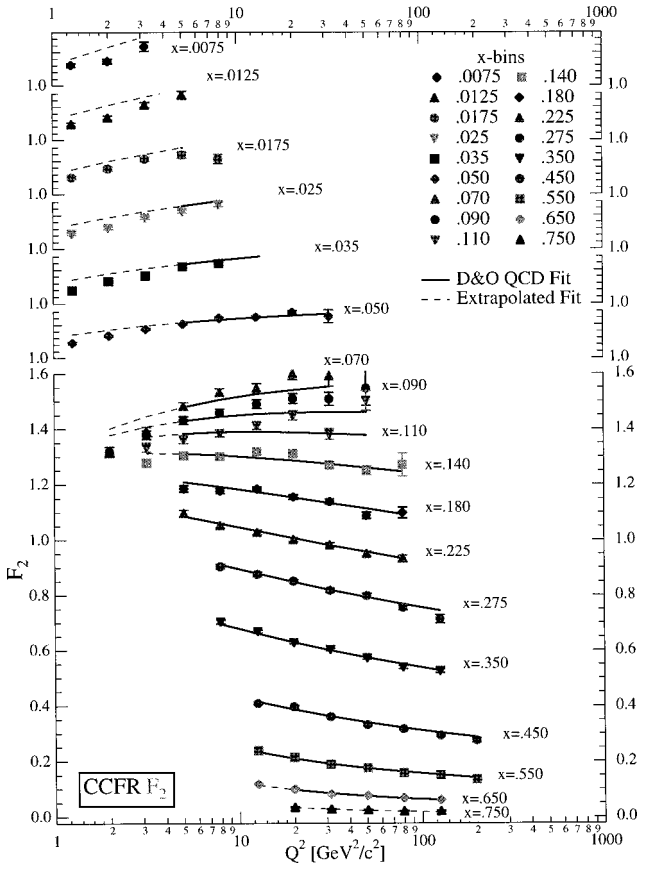

FIG. 11. CCFR F_2 measurement (Seligman *et al.*, 1997a, 1997b). Errors are statistical only. Lines indicate the CCFR QCD fit discussed in the text.

where ρ is the target density, L is the target length, and N_A is Avogadro's number. The structure functions are extracted by varying the Monte Carlo input to match the number of events in each acceptance-corrected bin.

The CCFR results presented here are from the final analysis of the E744/E770 data, which differ from the preliminary results of Quintas *et al.* (1993). Detailed information on the improvements to the analysis that led to the differences from the preliminary results can be found in Seligman *et al.* (1997a, 1997b) but a brief summary of the most important changes is given below. Improvements between the early and final analysis were made in energy calibration and modeling of energy loss by the scattered μ in the target. New techniques were developed for the handling of dimuon events, which arise from charm and π and K decays. Improvements were made to the flux extraction method, and more complete radiative corrections were applied. Finally, an updated R parametrization was used.

Figures 11 and 12 show the CCFR measurements of F_2 and xF_3 as a function of Q^2 in various bins of x. Only statistical errors are shown, and the systematic errors are approximately 2%. The solid and dashed curves on the plot indicate the QCD fits that are discussed in Sec. III.E. The precision of the data is such that subtle deviations from the QCD expectation can be probed.

2. F_2 and xF_3 extracted from the cross section

The structure functions can be extracted by forming the sums and differences of the differential cross section given in Eq. (12). This technique was used by the CDHSW and CHARM experiments. To make the measurement, the number of events in each x and Q^2 bin is related to the differential cross section by

$$\frac{1}{E_\nu}\frac{d^2\sigma}{dx\,dQ^2}=\frac{N(x,Q^2,E_\nu)}{N(E_\nu)}\frac{\sigma_{\rm tot}/E_\nu}{dx\,dQ^2}, \tag{40}$$

where $N(x,Q^2,E_\nu)$ is the number of events in each (x,Q^2,E_ν) bin and $N(E_\nu)$ is the number of events in each E_ν bin integrated over x and Q^2. The structure functions can then be expressed in terms of the sums and differences of neutrino and antineutrino cross sections as

$$\begin{aligned}(\pi/G^2M)&\left(\frac{1}{E_\nu}\frac{d^2\sigma^\nu}{dx\,dQ^2}+\frac{1}{E_\nu}\frac{d^2\sigma^{\bar\nu}}{dx\,dQ^2}\right)\\&=f(y,R_L)F_2+g(y)\Delta(xF_3),\\(\pi/G^2M)&\left(\frac{1}{E_\nu}\frac{d^2\sigma^\nu}{dx\,dQ^2}-\frac{1}{E_\nu}\frac{d^2\sigma^{\bar\nu}}{dx\,dQ^2}\right)=2g(y)xF_3,\end{aligned} \tag{41}$$

where

$$\begin{aligned}f(y,R_L)&=\left[1-y+\frac{y^2}{2(1+R_L)}\right]\frac{y}{Q^2},\\g(y)&=y\left(1-\frac{y}{2}\right)\frac{y}{Q^2},\end{aligned} \tag{42}$$

and F_2 and xF_3 can be extracted by solving the coupled equations.

The difference between xF_3 in neutrino and antineutrino scattering, $\Delta(xF_3)$, is related to the difference between the strange- and charm-sea distributions, $(s-c)$, as shown in Eq. (20) and discussed in Sec. IV.

3. Assumptions concerning R_L

The ratio of the longitudinal-to-transverse absorption cross section, R_L, can be measured from the y dependence of deep-inelastic scattering data. Fits to the function F,

$$\begin{aligned}F(x,Q^2,\epsilon)&=\frac{\pi(1-\epsilon)}{y^2G_F^2ME_\nu}\left(\frac{d^2\sigma^\nu}{dx\,dy}+\frac{d^2\sigma^{\bar\nu}}{dx\,dy}\right)\\&=2xF_1(x,Q^2)[1+\epsilon R_L(x,Q^2)],\end{aligned} \tag{43}$$

which follows from Eqs. (11) and (12) for $M_W^2\gg Q^2$ and $M\ll Q$, E_ν, can be used to determine R_L. In this equation, $\epsilon\simeq 2(1-y)/[1+(1-y)^2]$ is the polarization of the virtual W boson. This equation assumes $xF_3^\nu=xF_3^{\bar\nu}$, and therefore a correction for $\Delta(xF_3)$ must be applied. The values of $R_L=\sigma_L/\sigma_T$ are extracted from linear fits to F versus ϵ at fixed x and Q^2 bins.

There are very few measurements of R_L from deep-inelastic neutrino scattering. Two experiments with published results are CHARM (Bergsma *et al.*, 1984) and CDHSW (Abramowicz *et al.*, 1983). A comparison of the CDHSW measurements of R_L is made to the charged-lepton scattering results in Fig. 13. The best fit to the world's data on R_L is given by the parametrization "$R_{\rm world}$" (Whitlow *et al.*, 1992), which is also shown in the plot.

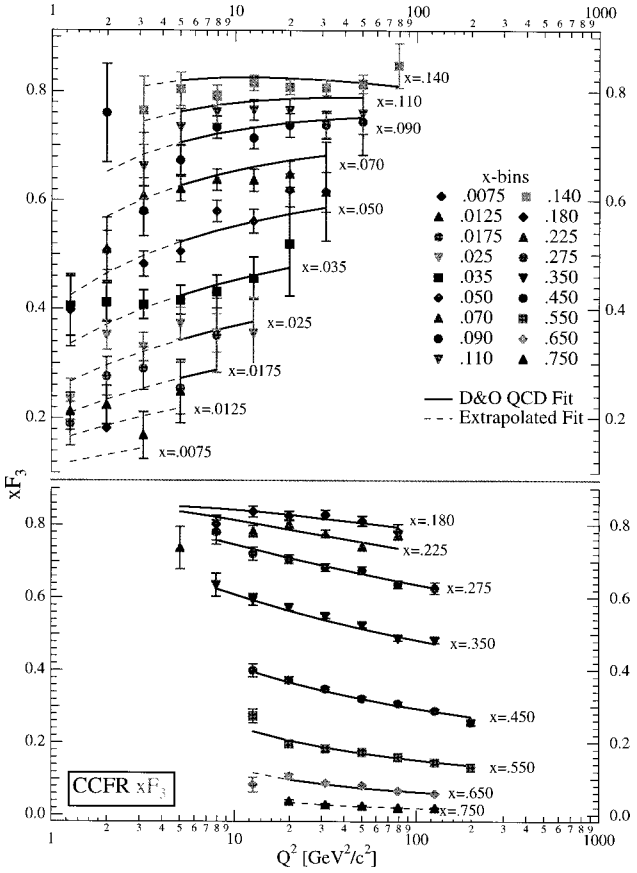

FIG. 12. CCFR xF_3 measurement (Seligman *et al.*, 1997a, 1997b). Errors are statistical only. Lines indicate the CCFR QCD fit discussed in text.

CCFR E744/E770 is in the process of measuring R_L as a function of x and Q^2. The wide range of CCFR beam energies produces an extended range of kinematically accessible y values in each Q^2 and x bin (Yang *et al.*, 1996). Therefore the lever arm for the fit in most kinematic bins is large.

For the F_2 and xF_3 results compared in the next section, various assumptions concerning R_L were made: BEBC and CHARM assumed $R_L=0$, CCFR E616/E701 used $R_{L,\rm QCD}$, CCFR E744/E770 implemented the $R_{\rm world}$ parametrization, and CDHSW used $R_L=0.1$.

C. Structure functions from neutrino experiments

This section compares results from precision neutrino structure-function measurements. Small differences in the technique and assumptions used for extracting the structure functions complicate this comparison. The assumptions concerning the structure function R_L were discussed in the previous section. CDHSW and CCFR assume nonzero values for the strange sea, while CHARM and BEBC assume the strange sea to be zero. All experiments apply radiative corrections, but the

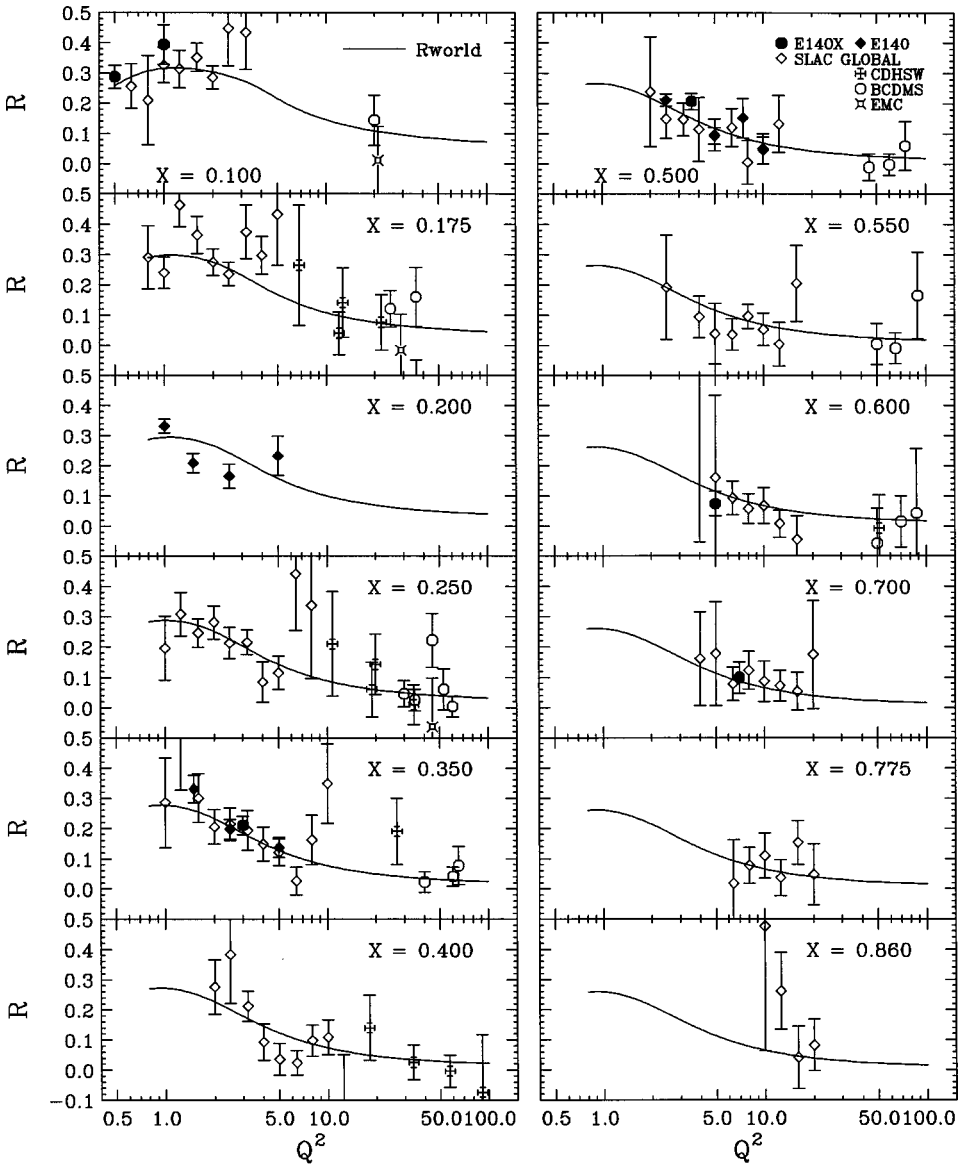

FIG. 13. Measurements of R_L by neutrino and charged-lepton experiments. Solid line indicates the "world" parametrization (Whitlow *et al.*, 1990) of R_L. The date are from SLAC E140(X) (Dasu *et al.*, 1988a, 1988b), EMC (Aubert *et al.*, 1987), BCDMS (Benvenuti *et al.*, 1990), and CDHSW (Berge *et al.*, 1991).

model and order of the calculation varies in each case (De Rujula *et al.*, 1979; Bardin and Dokuchaeva, 1986). Finally, CHARM and BEBC have applied corrections at high x for Fermi smearing, while CDHSW and CCFR have not. The discussion below is divided between measurements using high-A targets and those from deuterium. The recent data sets presented below are available in tabular format via the Internet.[3] Older experimental data are summarized in the tables of Diemoz *et al.* (1986); however, the structure functions for WHPFOR are in error, and the tables of reference Heagy *et al.* (1981) should be used.

1. Heavy-target experiments

The experiments with high-A targets have the advantage of high statistics. In the comparisons between experiments using high-A targets, various targets were used, and no nuclear corrections have been applied.

Figure 14 compares the structure function xF_3 from experiments with iron targets as a function of Q^2 for various x bins. These are from WHPFOR (Heagy *et al.*, 1981), CDHSW (Berge *et al.*, 1991), CCFR E616/E701 (Oltman *et al.*, 1992), CCFR E744/E770 (Seligman *et al.*,

[3]The CCFR Collaboration E744/770 structure functions are available in tabular form by contacting seligman@nevis1.columbia.edu. Data from BEBC, CCFR, CDHSW and many charged-lepton experiments are available in tables from the Durham Structure Function Archive, http://cpt1.dur.ac.uk/HEPDATA/structure1.html.

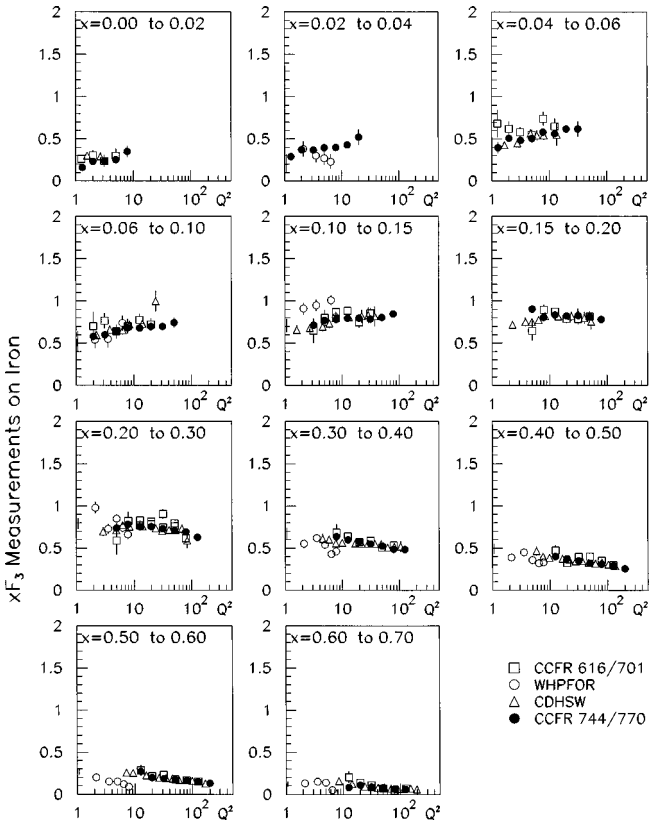

FIG. 14. Comparison of xF_3 data from experiments with iron targets.

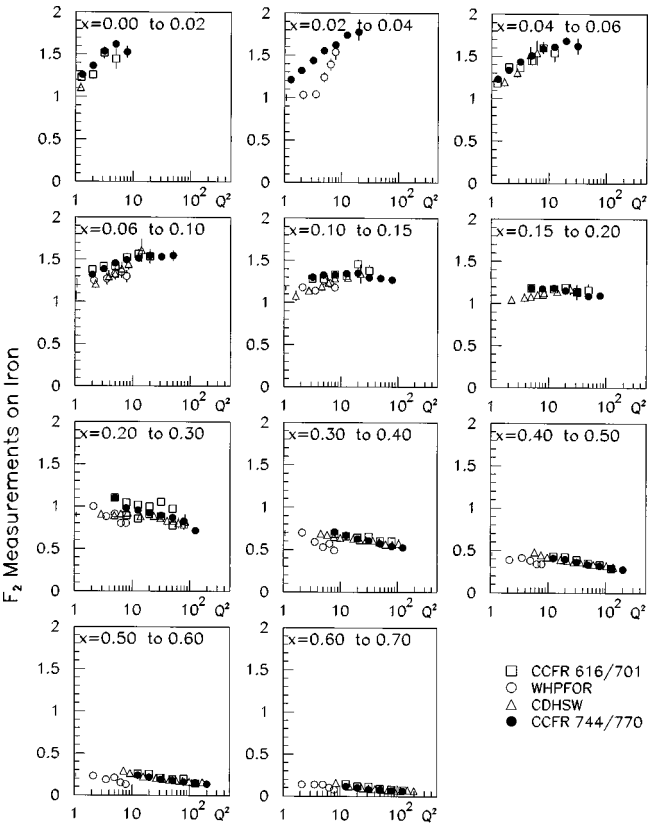

FIG. 15. Comparison of F_2 data from experiments with iron targets.

1997a, 1997b). Of these experiments, CCFR E744/E770 has the smallest statistical error. The xF_3 measurements are in good agreement.

The F_2 comparison as a function of Q^2 is shown in Fig. 15. At low x and Q^2, CDHSW and WHPFOR data lie below the results from the two CCFR experimental analyses. The WHPFOR experiment used the 1981 average neutrino-iron total cross section to normalize their data: $\sigma^{\nu}/E=(0.63\pm0.02)\times10^{-38}$ cm^2/GeV^2 and $\sigma^{\bar{\nu}}/E=(0.30\pm0.01)\times10^{-38}$ cm^2/GeV^2. These cross sections are lower than the current world average, discussed in Sec. II. Thus the WHPFOR data lie below the CCFR results. As will be shown in Sec. III.E, the shape of the Q^2 dependence as a function of x for the CDHSW data cannot be described by a QCD-based parametrization.

Figures 16 and 17 compare xF_3 and F_2 measured on various targets. The CCFR E744/E770 data are used to represent iron targets. The BEBC (Varvell *et al.*, 1987) data were taken on a neon target. Gargamelle (Morfin *et al.*, 1981), an earlier and less precise bubble-chamber experiment, used a C_3H_8-CF_3Br mixture. The CHARM data were taken on marble ($CaCO_2$). The statistical errors are sufficiently large that the data are consistent, despite the apparent wide spread between experiments.

The qualitative behavior of the structure functions averaged over Q^2 as a function of x, shown in Fig. 18, can be interpreted within QCD. Quantitative QCD studies, interpretations, and measurements will be discussed in Sec. III.E.

The structure function xF_3 is related to the sum of the valence quarks, and the measured distribution is peaked at moderate x, going to zero as x goes to zero or one. If the proton consisted of three noninteracting valence quarks, then this distribution would simply reflect the Fermi motion of the quarks inside the nucleon and would peak at $x=\frac{1}{3}$. However, because these quarks are interacting via gluons, which carry some of the fractional momentum of the proton, the distribution is smeared further and peaks at smaller x. The position of the peak will move toward smaller x with increasing Q^2 due to QCD evolution. Since each neutrino experiment covers a different range of Q^2, the data points on Fig. 18 are not expected to agree.

The F_2 structure function is related to the sum of the quark and antiquark distributions. The F_2 distribution goes to zero at high x, but is approximately constant in the low-x region. Gluon radiation and gluon splitting into quark-antiquark pairs results in a large number of low-momentum partons that dominate the low-x region. In fact, the charged-lepton scattering results on F_2 from HERA have shown that at very low x, outside of the kinematic range accessible to present neutrino experiments, F_2 rises dramatically (Aid *et al.*, 1996b; Derrick *et al.*, 1996a).

2. Deuterium and hydrogen targets

The BEBC experiment has used neutrino and antineutrino scattering from deuterium to obtain the best

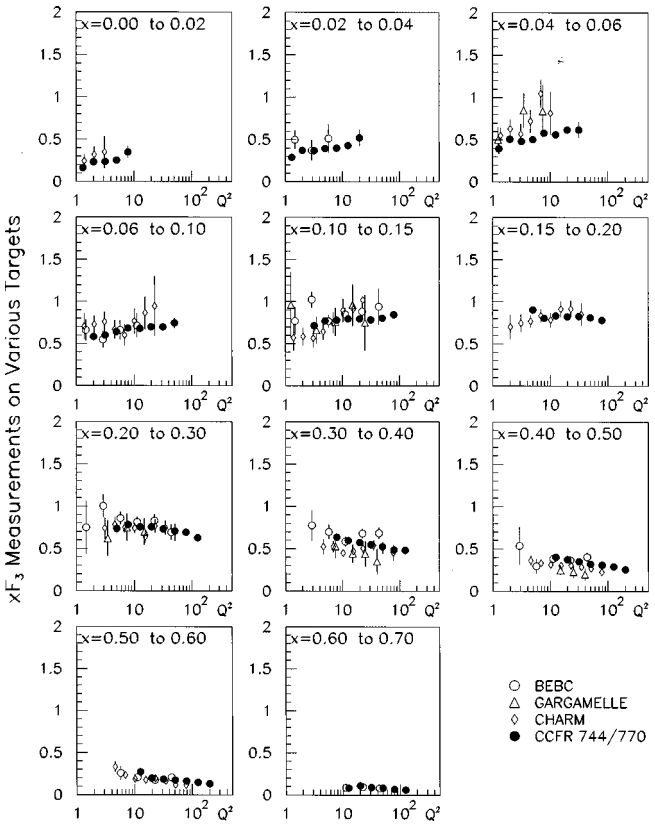

FIG. 16. Comparison of xF_3 data from experiments with various high-A targets.

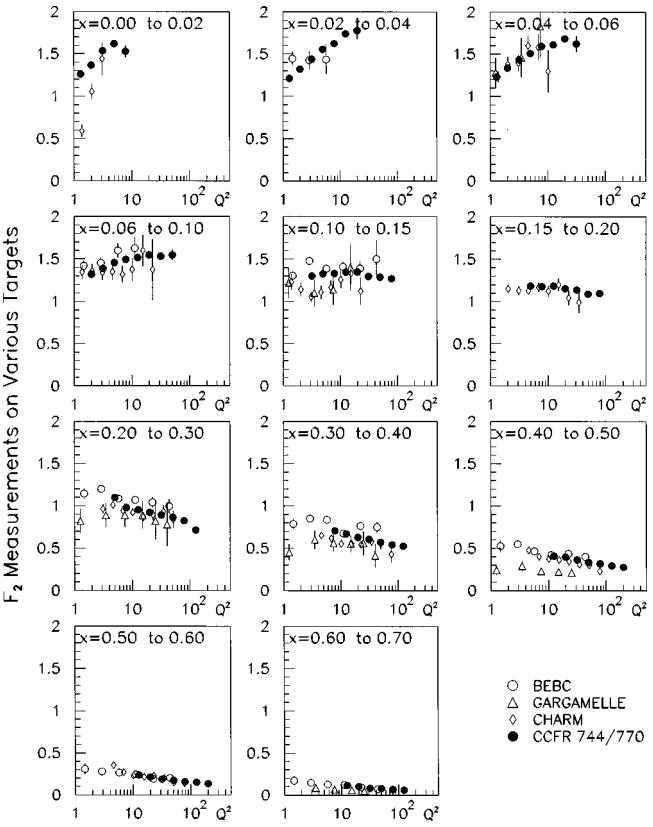

FIG. 17. Comparison of F_2 data from experiments with various high-A targets.

measurement of the structure functions on the proton and the neutron separately (Allasia *et al.*, 1985; Jones *et al.*, 1994). A neutrino or antineutrino interaction was identified as coming from a neutron if it had either an even number of prongs or an odd number of prongs with a proton with momentum less than 150 MeV (thus interpreted as a spectator). All remaining events, with an odd number of prongs and hence a net total charge, were classified as interactions with protons. Misidentifications were corrected on a statistical basis using a Monte Carlo simulation.

The resulting structure functions for neutrino scattering on protons and neutrons, $F_2^{\nu p}$ and $F_2^{\nu n}$, are shown in Fig. 19. The most evident feature is that $F_2^{\nu n} \approx 2F_2^{\nu p}$ over most of the kinematic region. This is because the W^+ emitted in a neutrino interaction must interact with a negatively charged quark, which at high x has the highest probability of being the valance d quark. Since the neutron has twice the number of valance d quarks as the proton, the neutron structure function is larger. These data clearly indicate the flavor sensitivity of neutrino scattering.

D. Comparisons of neutrino to charged-lepton Experiments

Neutrino deep-inelastic scattering experiments now have the statistical accuracy of charged-lepton scattering experiments. In this section, neutrino results are compared to charged-lepton results from SLAC (eN), NMC (μN), BCDMS (μN), and E665 (μN). The kinematic ranges covered by these experiments are shown in Fig. 20, with the CCFR region shown for comparison. The HERA ep data are mainly at high Q^2 and very low x, with only small kinematic overlap with the fixed-target neutrino data.

1. Comparison of F_2

The parity-conserving structure function F_2 is measured by both charged- and neutral-lepton scattering experiments. The definitions of F_2 in neutrino and charged-lepton scattering were discussed in Sec. I.C. As a result of the difference in the couplings, a conversion must be applied in order to compare muon and neutrino experiments. To lowest order with the charm sea set to zero, the correction is

$$F_2^{\mu N} = \frac{5}{18} F_2^{\nu N} \left[1 - \frac{3(s+\overline{s})}{5(q+\overline{q})} \right], \tag{44}$$

where $q+\overline{q}$ represents the sum over all quark flavors. This relation is true to all orders in the deep-inelastic scattering (DIS) scheme, which maintains Eq. (22) as the definition of F_2.

Assuming that the strange sea is small at high x, one expects $F_2^{\mu N}/F_2^{\nu N} \to \frac{5}{18} = 0.2778$ as $x \to 1$. Comparing the CCFR data and the CDHSW data (Mishra and Sciulli, 1989) to the results from BCDMS (Benvenuti *et al.*,

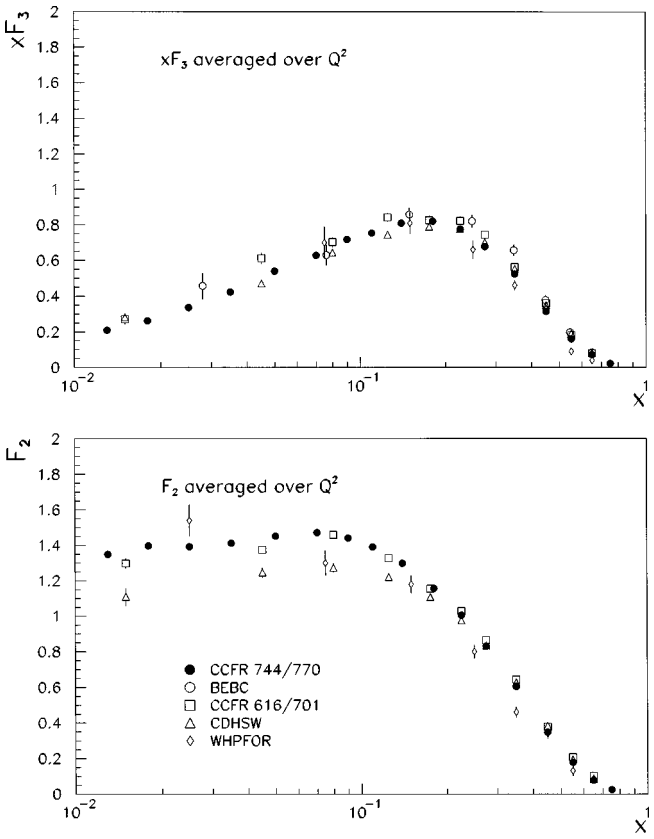

FIG. 18. Average xF_3 and F_2 as a function of x: ○, BEBC; □, CCFR E616/E701; ●, CCFR E744/E770; △, WHPFOR.

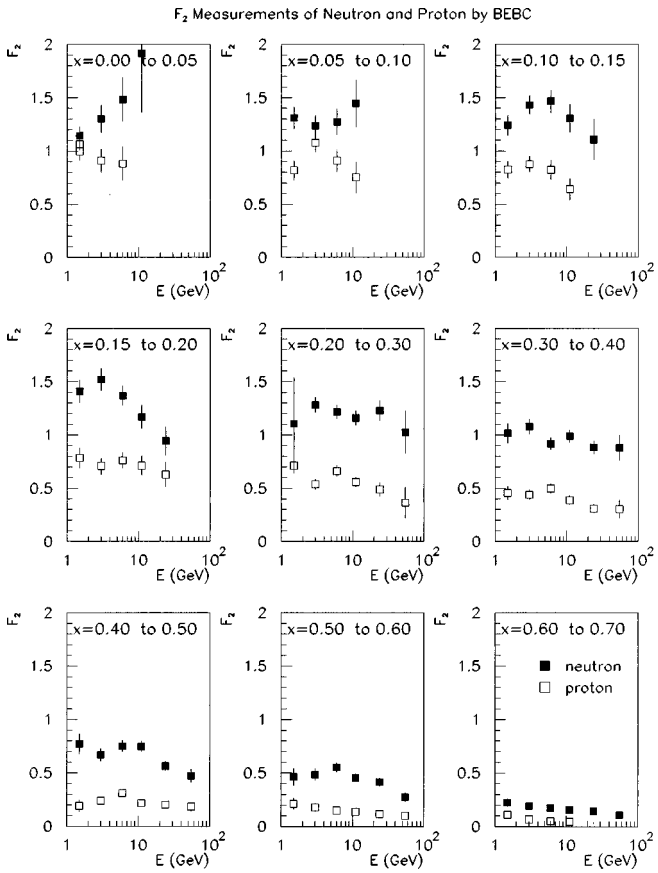

FIG. 19. Neutron and proton measurements by the Big European Bubble Chamber: □, $F_2^{\nu p}$; ■, $F_2^{\nu n}$. The data have been averaged over Q^2, and E refers to the incident-neutrino energy E_ν.

1987) at high x yields a ratio of 0.278 ± 0.010, which is in excellent agreement with the expected quark charges.

In the comparisons given below, all corrections for the differences between the charged-lepton and neutrino data have been applied to the charged-lepton data. The strange sea $(s,\overline{s})$ appears explicitly in Eq. (44), and therefore a measurement of this distribution is needed for the comparison. The strange sea can be measured from the neutrino charm production cross section, which is related to charged-current dimuon production (Bazarko *et al.*, 1995), described in detail in Sec. IV. Additional nuclear corrections must also be made to the charged-lepton measurements of F_2, as discussed in Sec. III.A.2.b.

Figures 21–26 compare the CCFR F_2 measurement to the measurements from NMC (Amaudruz *et al.*, 1992b) and E665 (Adams *et al.*, 1995) over a range of x values. The corrections for charge coupling, using the DIS scheme, and nuclear effects have been applied to the muon data. Also shown are several global parton distribution fits including CTEQ4M (Lai *et al.*, 1997; dashed curve), GRV 94 HO (Glück *et al.*, 1995; dotted curve), and MRS R2 (Martin *et al.*, 1996; solid curve).

At low x there appears to be a disagreement between the charged-lepton scattering data and the neutrino data. The charged-lepton F_2 values are lower than the neutrino F_2 results by 16% at $x=0.01$, 10% at $x=0.03$, and 6% at $x=0.05$. The discrepancy decreases with increasing x until $x \approx 0.070$, where the data are in good agreement to the highest x bins.

The high-statistics data in the region of the discrepancy come from CCFR and NMC. It is possible that one or both experiments have underestimated their systematic errors. The most important systematic error in the CCFR analysis is due to the calorimeter calibration. Ex-

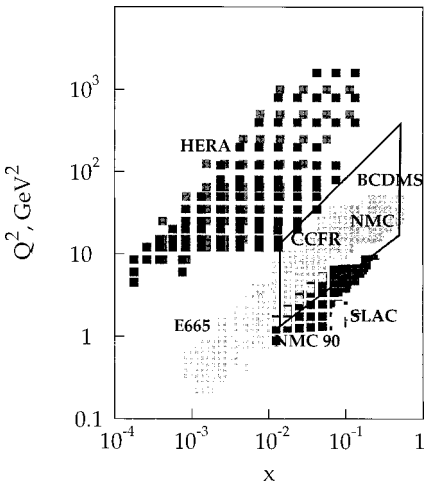

FIG. 20. The kinematic region accessible to various charged-lepton experiments compared to the CCFR experiment.

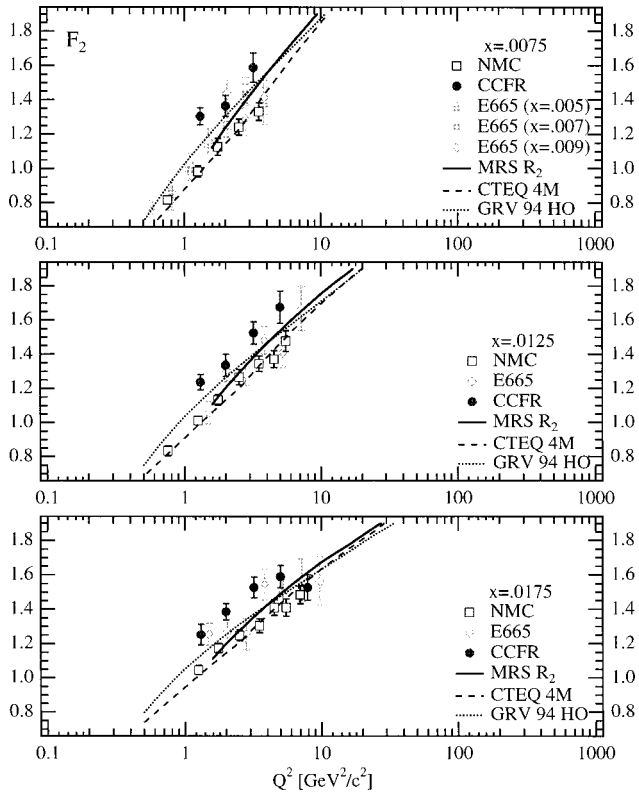

FIG. 21. Comparison of the CCFR (ν) measurement of F_2 (Seligman *et al.*, 1997a, 1997b) to the NMC and E665 (μ) results for $x=0.0075$, 0.0125, and 0.0175.

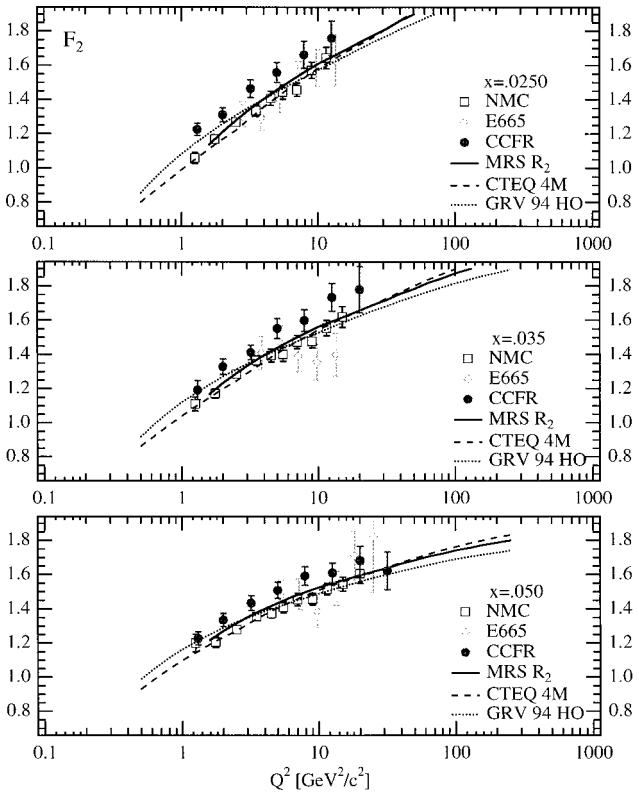

FIG. 22. Comparison of the CCFR (ν) measurement of F_2 (Seligman *et al.*, 1997a, 1997b) to the NMC and E665 (μ) results for $x=0.0250$, 0.035, and 0.050.

tensive studies of the test-beam data were undertaken in order to determine the muon and hadron energy calibration, and the systematic error assigned to this source was carefully estimated by the experiment.

Several publications have suggested that the discrepancy is due to an incorrect strange-sea correction (Botts *et al.*, 1993; Barone *et al.*, 1994; Brodsky and Ma, 1996). The strange-sea correction, $[1-3(s+\bar{s})/5(q+\bar{q})]$, for $Q^2=4$ GeV^2 is 11% at $x=0.01$, 9% at $x=0.03$, and 8% at $x=0.05$ and would need to be approximately doubled in this region to account for the discrepancy. For example, the required strange-sea distributions needed to eliminate the discrepancy, as calculated at next-to-leading order by the CTEQ collaboration (Botts *et al.*, 1993), are inconsistent by a factor of 2 at low x as compared to the direct CCFR strange-sea measurement from dimuon data (Bazarko *et al.*, 1995). The CCFR measurement of the strange sea, which is to next-to-leading order and includes corrections for the charm mass threshold, would have to be incorrect by 5σ to account for the discrepancy. The CCFR strange-sea measurement and its application to the correction presented here is described in detail in Sec. IV.

Another possible cause for the disagreement between the neutrino and charged-lepton measurements of F_2 may be the nuclear correction applied to the charged-lepton deuterium data in order to allow comparison with the neutrino results. As discussed in Sec. III.A.2.b, the corrected charged-lepton data will only agree with the neutrino result if the entire effect is ascribed to the target material. Propagator effects, such as fluctuation of the virtual boson to mesons, will not be the same for neutrino and charged-lepton scattering because of the additional axial component of the W. Such "nuclear shadowing" would be expected to affect the low-x (low-Q^2) region most strongly, thereby accounting for some of the disagreement. The data on these nuclear effects in neutrino and charged-lepton scattering are discussed in the next section.

2. Nuclear effects

Very few data on shadowing in neutrino scattering have been obtained. The best measurements come from the BEBC collaboration ratios of neon ($A=20$) to deuterium (Allport *et al.*, 1989). This can be compared to the muon-scattering results from carbon ($A=12$) as measured by the NMC experiment (Amaudruz *et al.*, 1995). Figure 27(a) shows Ne/D_2 directly compared to C/D_2, while Fig. 27(b) applies a correction factor for the theoretically expected $A^{-(2/3)}$ dependence of the nuclear cross section to the carbon ratio (Geesaman *et al.*, 1995), although it should be noted that some experimental results indicate less A dependence (Adams *et al.*, 1995). Data are shown for $Q^2>1$ GeV^2, except for the three lowest-x BEBC data points, which are from $Q^2<0.2$ GeV^2, $(0.2<Q^2<0.5)$ GeV^2, and $(0.5<Q^2<1.0)$ GeV^2, respectively. Within the combined statistical and systematic errors, the results from charged-

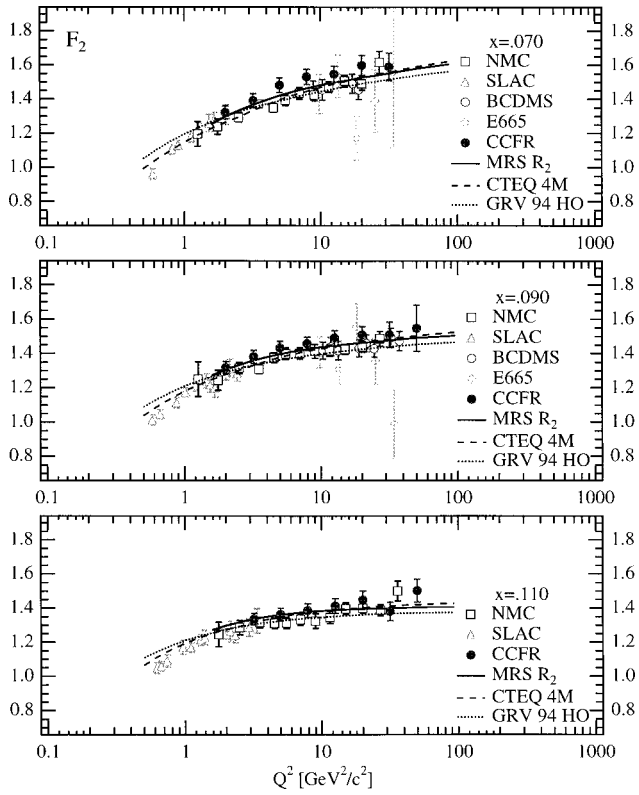

FIG. 23. Comparison of the CCFR (ν) measurement of F_2 (Seligman *et al.*, 1997a, 1997b) to the NMC and E665 (μ) results and SLAC (e) results for $x=0.070$, 0.090, and 0.110.

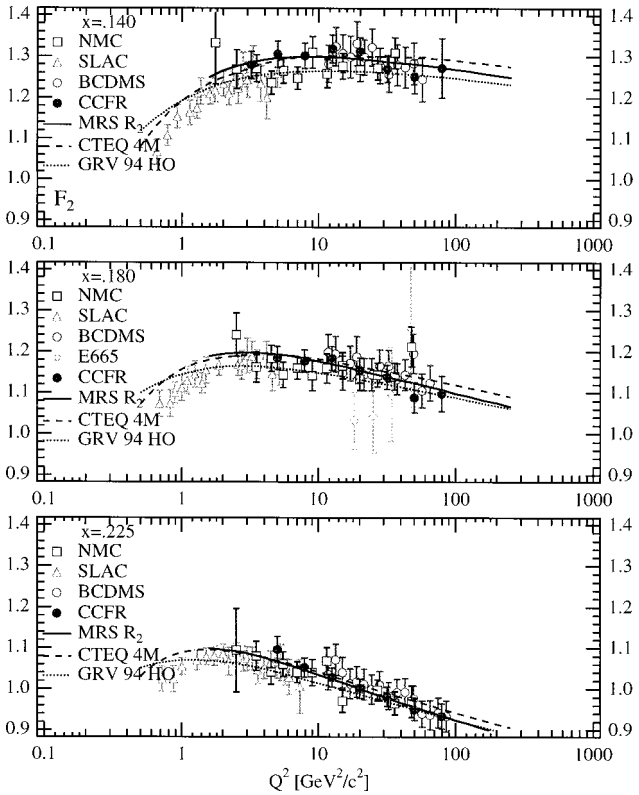

FIG. 24. Comparison of the CCFR (ν) measurement of F_2 (Seligman *et al.*, 1997a, 1997b) to the NMC and E665 (μ) results for $x=0.140$, 0.180, and 0.225.

lepton and neutrino scattering appear to agree. These results are also in agreement with an earlier, lower-statistics BEBC measurement of this ratio, which used a 3-m^3 track-sensitive target filled with deuterium surrounded by neon (Cooper *et al.*, 1984). CDHSW has measured the ratio of structure functions in iron to hydrogen (Abramowicz *et al.*, 1984) using a 35-m^3 hydrogen tank located in front of the CDHSW detector. This experiment obtained 4457 νp events and 4178 $\overline{\nu p}$ events, which were compared to 50 000 neutrino and 150 000 antineutrino events in iron. Although the combined systematic and statistical errors are too large to establish A dependence, the behavior of the data is consistent with the behavior observed in charged-lepton scattering.

Although the NMC and E665 shadowing data that were used to obtain the nuclear correction are in statistical agreement, there appears to be a systematic shift between the two data sets, as can be seen in Fig. 10. The nuclear correction is dominated by the NMC result, which has much smaller errors than the E665 data. However, if only the E665 data are used in a fit that is then applied to the charged-lepton deuterium results, then the CCFR/NMC discrepancy is reduced by approximately a factor of 2 for $x<0.03$. However, it seems unlikely that the entire νN versus μN low-x discrepancy can be due to nuclear effects alone.

E. QCD Analyses of the structure-function results

An analysis of the structure-function data within the QCD framework allows precise tests of the predicted QCD evolution and the Gross-Llewellyn Smith and Adler sum rules. From these studies, measurements of α_s and the parton distributions can be extracted.

1. The strong coupling measured from QCD evolution

Perturbative QCD can predict the Q^2 evolution of the structure functions given a starting set of x-dependent parton distribution functions at a reference scale Q_0^2 (Gribov and Lipatov, 1972; Altarelli and Parisi, 1977; Dokshitser, *et al.*, 1978, 1980), as described in Sec. III.A.1. Therefore an analysis of scaling violations in structure-function data permits a determination of the parton distributions and the QCD parameter Λ. The CCFR E744/E770 analysis, which is the most precise to date, provides an example of the extraction of these distributions and the QCD parameter at next-to-leading order for four flavors in the $\overline{\text{MS}}$ renormalization scheme ($\Lambda_{\overline{\text{MS}}}^{\text{NLO}-4f}$).

Two independent QCD evolution analyses were performed by CCFR. The first used only the parity-violating structure function xF_3. The advantage of this analysis is that the evolution of xF_3 is independent of the gluon distribution, reducing the number of free parameters. The second analysis used both xF_3 and F_2 data in the QCD fit. This increases the statistical power of the fit but introduces extra parameters to describe the gluon distribution. On the other hand, the combined F_2/xF_3 data can constrain the gluon distribution $G(x,Q^2)$ at moderate values of x. Note that charged-

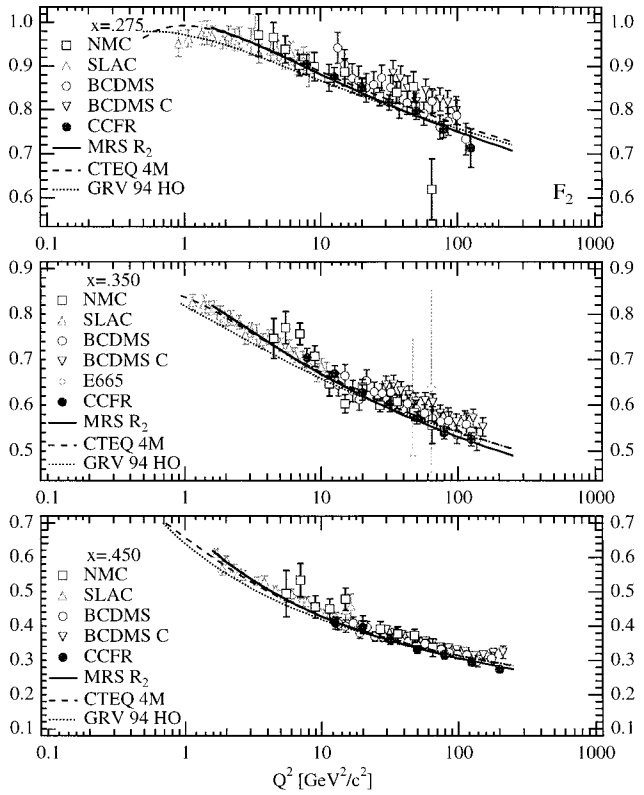

FIG. 25. Comparison of the CCFR (ν) measurement of F_2 (Seligman *et al.*, 1997a, 1997b) to the NMC and E665 (μ) results for $x=0.275$, 0.350, and 0.450.

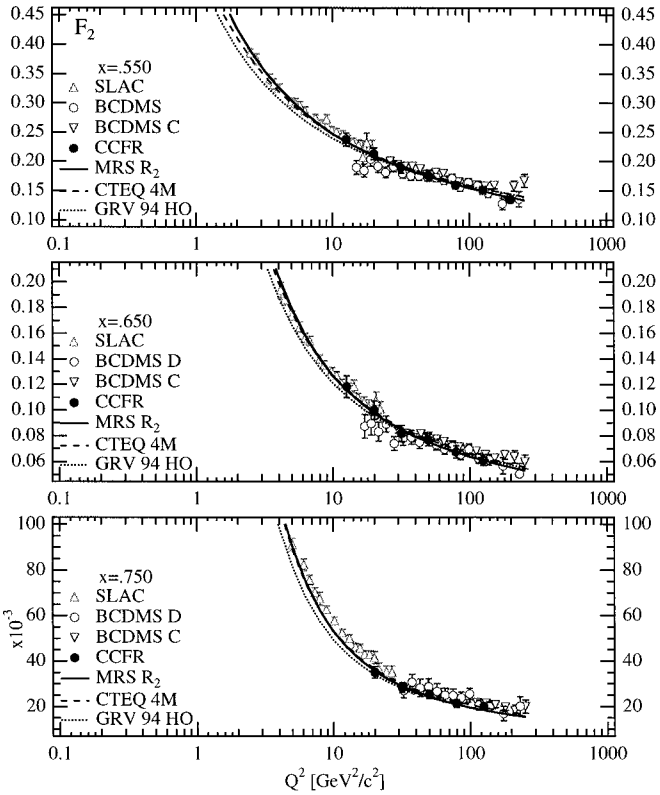

FIG. 26. Comparison of the CCFR (ν) measurement of F_2 (Seligman *et al.*, 1997a, 1997b) to the NMC and E665 (μ) results for $x=0.550$, 0.650, and 0.750.

lepton scattering experiments cannot separate gluon distribution effects from the running of α_S as cleanly because they do not have access to the parity-violating structure function, xF_3.

The QCD fits require initial parametrizations of the parton distributions at some Q_0^2. CCFR E744/E770 used

$$xq^{NS}(x,Q_0^2)=A_{NS}x^{\eta_1}(1-x)^{\eta_2},$$
$$xq^{S}(x,Q_0^2)=xq^{NS}(x,Q_0^2)+A_S(1-x)^{\eta_S},$$
$$xG(x,Q_0^2)=A_G(1-x)^{\eta_G}, \tag{45}$$

where NS, S, and G refer to nonsinglet, singlet, and gluon distributions, respectively, and $A_{\rm NS}$, A_S, A_G, η_1, η_2, and η_G are free parameters in the fit. More complicated parametrizations of the parton distributions were found to yield fit results consistent with the above parametrizations (Seligman *et al.*, 1997a, 1997b). The resulting parton distributions are compared to other measurements in Sec. III.E.2.

The CCFR analysis compared data to a theoretical prediction based on a next-to-leading-order QCD evolution program (Duke and Owens, 1984) using a χ^2 technique that included the effects of target mass, higher twist, and $R_{L,\rm QCD}$. Only data satisfying $Q^2>5$ GeV^2, $W^2>10$ GeV^2, and $x<0.7$ were included, and (x,Q^2) bins with statistical error greater than 50% were eliminated. The effects of systematic errors were studied by implementing positive and negative shifts of F_2 and xF_3 caused by each systematic error and reextracting Λ as well as the other fit parameters. The results of next-to-leading-order QCD fits in the $\overline{\rm MS}$ scheme to the CCFR structure-function data are shown by the solid line in Figs. 11 and 12. The dashed lines in these figures represent an extrapolation of the parametrization from the fit to lower Q^2 values.

An alternative and more powerful way to incorporate systematic uncertainties is to include their effects directly in the QCD fit. For this type of analysis, a χ^2 fit to the theoretical prediction for the structure functions is compared to the data in each x and Q^2 bin. The predic-

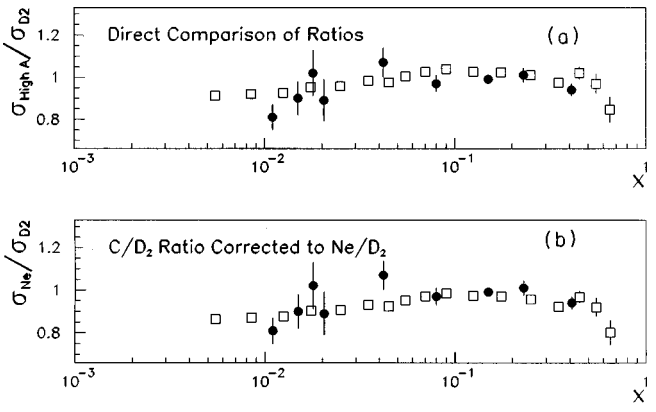

FIG. 27. Comparison of the ratio of cross sections for high-A targets to deuterium: ●, BEBC data from neutrino-neon scattering; □, NMC data from muon-carbon scattering.

TABLE III. Values of $\Lambda_{\overline{\rm MS}}^{\rm NLO-4f}$ determined from fits to the CCFR data. The systematic error includes the experimental, physics model, and higher-twist uncertainties.

	From xF_3 only		From xF_3 and F_2	
Fit type:	$\Lambda \pm \text{stat} \pm \text{sys}$	χ^2/DOF	$\Lambda \pm \text{stat} \pm \text{sys}$	χ^2/DOF
Basic	$387 \pm 42 \pm 94$	81/82	$381 \pm 23 \pm 58$	191/164
Global	$381 \pm 41 \pm 37$	69/82	$337 \pm 21 \pm 23$	171/164

tion should be compared to the data using a χ^2 that includes both statistical and systematic uncertainties with correlations. The systematic uncertainties can be handled by introducing a parameter δ_k for each uncertainty k into the χ^2. Defining the structure-function vector $\mathbf{F}=(F_2, xF_3)$ and the structure-function error matrix $\mathbf{V}=(\sigma_{ij})$, for $i,j=F_2, xF_3$, then the differences between the theoretical prediction and data and the χ^2 are

$$\mathbf{F}^{diff}=\mathbf{F}^{\rm data}-\mathbf{F}^{\rm theory}+\sum_k \delta_k(\mathbf{F}^k-\mathbf{F}^{\rm data}), \tag{46}$$

$$\chi^2=(\mathbf{F}^{\rm diff})\mathbf{V}^{-1}(\mathbf{F}^{\rm diff})^T+\sum_k \delta_k^2, \tag{47}$$

where $\mathbf{F}^k$ is the value of the extracted structure functions when the kth systematic parameter is shifted by 1σ. For the CCFR data, the results of this fitting method are compared in Table III to the "basic" method described above. The "global fit" gives a more precise measure of Λ because of the constraint of QCD. The good χ^2 per degree of freedom indicates consistency of the data with QCD.

Table IV compares the CCFR E744/E770 results to those from other neutrino experiments. The CCFR E616/E701 experiment used an earlier version of the next-to-leading-order fitting employed by CCFR E744/E770. Methods for fitting vary between experiments. The CDHSW used similar algorithms and parton distribution parametrizations to those used by CCFR. The CHARM experiment fit the parton distributions to Laguerre polynomials in $\ln(1/x)$ (Bergsma *et al.*, 1983). In this method, developed by Furmanski and Petronzio (1982), the form of the initial parton distributions at some Q_0 is not required as input.

The CDHSW data are not in agreement with the other neutrino measurements (see Sec. III.C.1) or with the expected QCD behavior. Another way to see this is to consider the logarithmic derivative of the structure functions with respect to Q^2 as a function of x. Quantum chromodynamics predicts the form of this distribution up to one free parameter, Λ, given the parton distributions as inputs. Figure 28 shows the CCFR logarithmic slopes and the corresponding QCD fit to the data along with the CDHSW data for comparison.

TABLE IV. Values of $\Lambda_{\overline{\rm MS}}^{\rm NLO-4f}$ determined from fits to structure functions measured in various neutrino experiments.

Experiment	Structure Function(s) fit	$\Lambda_{\overline{\rm MS}}^{\rm NLO-4f}$
CDHSW	xF_3	200^{+200}_{-100}
	F_2	300 ± 80
CHARM	xF_3	310 ± 150
CCFR 616/701	F_2	340 ± 110
CCFR 744/770	xF_3	381 ± 55
	F_2, xF_3	337 ± 31

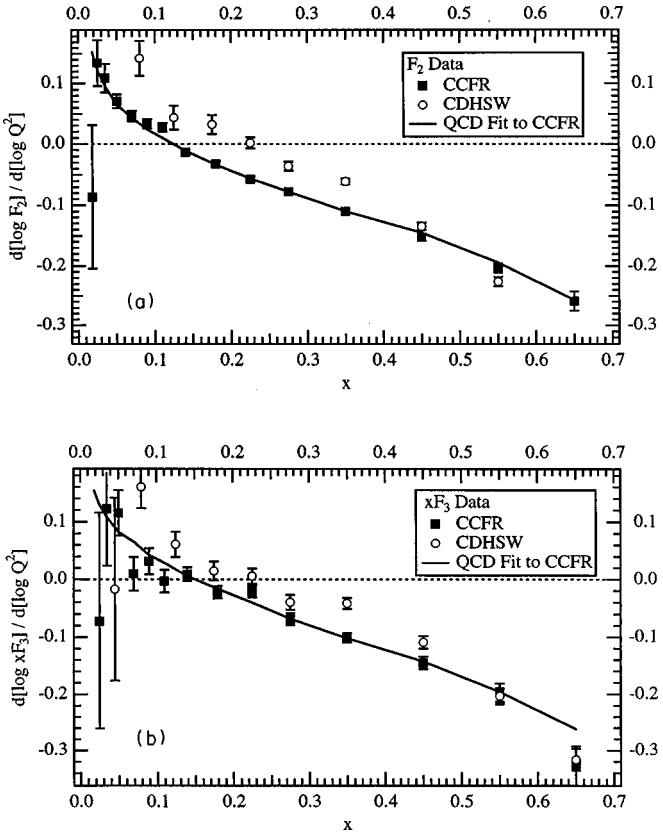

FIG. 28. CCFR and CDHSW logarithmic slopes of the structure functions, (a) F_2 and (b) xF_3. The line indicates the CCFR QCD fit result.

The value of $\Lambda=337\pm31$ MeV from the CCFR global fit using F_2 and xF_3 is one of the most accurate experimental determinations of this parameter and is equivalent to

$$\alpha_s(M_Z^2)=0.119\pm0.002(\text{exp})\pm0.004(\text{scale}) \quad \text{(CCFR)}.$$

The scale error is due to the renormalization and factorization scale uncertainties (Virchaux and Milsztajn, 1992). This result can be compared to other measurements as reported in Barnett *et al.* (1996). The CCFR result is higher than the previous measurement of CCFR, $\alpha_s(M_Z^2)=0.111\pm0.005$ (Quintas *et al.*, 1993) and is also higher than the previous deep-inelastic scattering average, $\alpha_s(M_Z^2)=0.112\pm0.005$. Including the new CCFR measurement, the average for deep-inelastic scattering experiments is

$$\alpha_s(M_Z^2)=0.117\pm0.004 \quad \text{(DIS Average)},$$

which is lower than the LEP measurement from event shapes of 0.122 ± 0.007. However, all of the above results

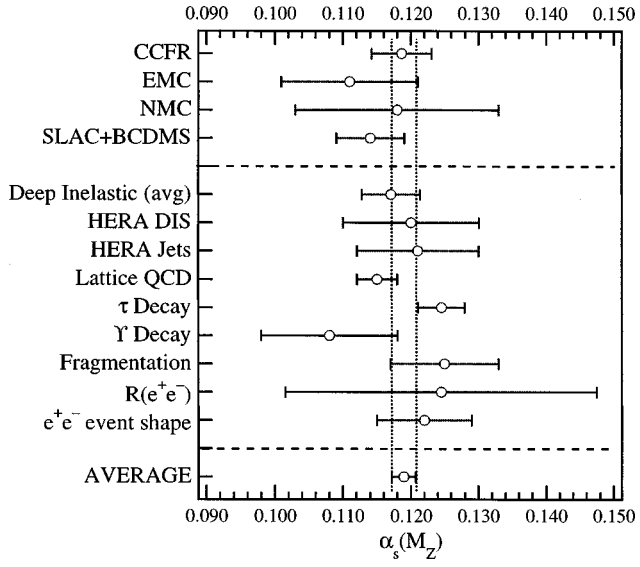

FIG. 29. Measurement of α_S from various experiments. CCFR result from Seligman *et al.* (1997a, 1997b) and other results from Barnett *et al.* (1996).

are consistent within the errors. Figure 29 compares the CCFR result to results from other non-neutrino experiments (Barnett *et al.*, 1996).

2. Parton distributions measured from QCD evolution

This section considers measurements of the parton distributions from the QCD evolution fits. The parton distributions are extracted simultaneously with the fit for Λ. This method can accurately determine the distributions for light quarks and gluons. The best method for determining the strange and charm distributions is through charged- and neutral-current charm production, respectively, as discussed in Sec. IV.

The parametrizations of the parton distributions found to fit best the CCFR E744/E770 data are compared with several popular PDF sets available from PDFLIB (Plothow-Besch *et al.*, 1993) in Fig. 30. These PDFs are obtained through global fits of the world's data, including charged- and neutral-lepton scattering, Drell-Yan production, and direct photon production. All three parton distribution functions [GRV 94 (Glück *et al.*, 1995), MRS R2 (Martin *et al.*, 1996), and CTEQ4M (Lai *et al.*, 1997)] have used preliminary CCFR E744/E770 structure-function data in the global fits, so the comparison contains some correlation. The data from other neutrino experiments have not been included in most global fits because of poor precision or disagreement with QCD.

The gluon distribution is the most poorly constrained of the parton distribution measurements. This is because in most processes where precision measurements can be used to extract PDFs, the gluons enter only indirectly through the QCD predictions for the Q^2 evolution. Fits to xF_3 and F_2, described previously, allow one to extract the form of the gluon distribution. The global fit to the CCFR E744/E770 data yields the distribution

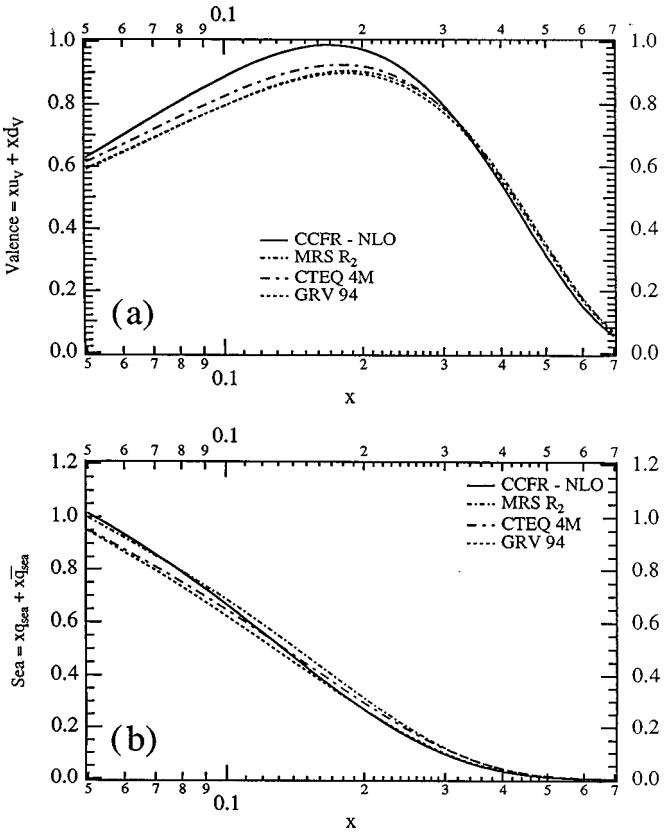

FIG. 30. The CCFR parton distributions compared to CTEQ 4M, MRS R_2, and GRV 94 at $Q^2=5\ \mathrm{GeV}^2$: (a) $xq_{\mathrm{valance}}=xu_V+xd_V$; (b) total sea$=\Sigma_{i=u,d,s}(xq_{i,\mathrm{sea}}+x\overline{q}_{i,\mathrm{sea}})$.

$$xG(x,Q_0^2=5\ \mathrm{GeV}^2)$$
$$=(2.22\pm0.25)(1-x)^{4.65\pm0.68}\quad(\mathrm{CCFR}).$$

Figure 31 shows this distribution as a function of x, evolved to $Q^2=32\ \mathrm{GeV}^2$. The shaded region indicates the CCFR $\pm1\sigma$ errors. For comparison, the crosses

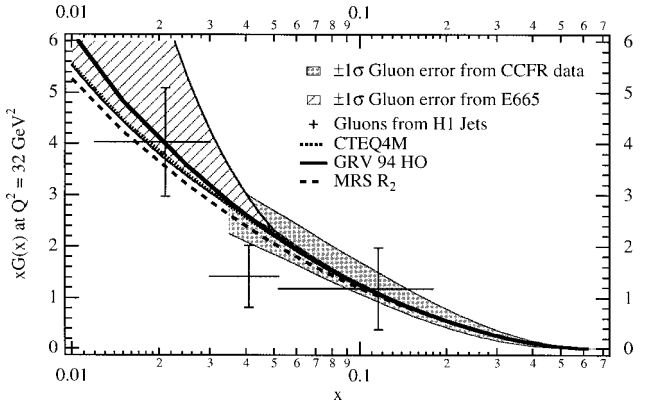

FIG. 31. The CCFR gluon distribution evolved to $Q^2=32\ \mathrm{GeV}^2$ and compared to gluon distributions measured in other processes. Shaded region shows $\pm1\sigma$ errors. Crosses show results from HERA jet measurements. Dotted line, CTEQ4M; solid line, GRV94 HO; dashed line, MRS R2. Hatched region is gluon distribution from E665 hadronic energy distributions.

show the gluon distribution as measured from jet production at the H1 experiment (Aid *et al.*, 1995). The hatched region indicates the E665 gluon distribution measured from the energy distribution of hadrons produced in deep-inelastic muon scattering (Adams *et al.*, 1996). Also shown are the gluon distributions from fits to data from a wide range of high-energy experiments that are available as parton distribution functions: GRV 94 HO (Glück *et al.*, 1995; solid curve), MRS R2 (Martin *et al.*, 1996; dashed curve), and CTEQ4M (Lai *et al.*, 1997; dotted curve). The gluon distributions from the various experiments agree in the region of the CCFR data with $x>0.04$. The gluon distribution also has been extracted by previous neutrino experiments, including CDHSW (Abramowicz *et al.*, 1983) and CHARM (Bergsma *et al.*, 1983). The CHARM gluon distribution was significantly softer than, and in disagreement with, those of the other neutrino experiments and non-neutrino measurements presented in Fig. 31. Unlike the other experiments, which define an initial x dependence for the gluon distribution, the CHARM analysis required only that the shape be representable by a Laguerre polynomial expansion in $1/x$.

3. The QCD sum rules

Quantum chromodynamic predictions exist for a wide variety of "sum rules," which are integrals over quark densities. Two QCD sum rules can only be measured in neutrino scattering: the Gross-Llewellyn Smith (GLS) sum rule and the Adler sum rule. The values for these sum rules are fundamental predictions of QCD.

a. The Gross-Llewellyn Smith sum rule

The GLS sum rule gives the QCD expectation for the integral of the valance quark densities. To leading order in perturbative QCD, the integral $\int(dx/x)(xF_3)$ is the number of valence quarks in the proton and should equal 3 (Gross and Llewellyn Smith, 1969). QCD corrections to this integral result in a dependence on α_s (Larin and Vermarseren, 1991):

$$\int_0^1 xF_3(x,Q^2)\,\frac{dx}{x} = 3\left[1-\frac{\alpha_s}{\pi}-a(n_f)\left(\frac{\alpha_s}{\pi}\right)^2-b(n_f)\left(\frac{\alpha_s}{\pi}\right)^3\right]. \tag{48}$$

In this equation, a and b are known functions of the number of quark flavors n_f that contribute to scattering at a given x and Q^2. This is one of the few QCD predictions that is available to order α_s^3.

One can determine $\alpha_s(Q^2)$ from $\int F_3 dx$ by inverting the Gross-Llewellyn Smith equation. However, for a given Q^2 value, there is a limited region in x that is accessible by the data from any one experiment. Two analysis methods address this problem.

The first method extrapolates all xF_3 data to a single Q^2 value, resulting in data over a sufficiently wide range of x to evaluate accurately the integral in Eq. (48). However, this introduces systematic errors involved in the assumptions for the extrapolation. To evaluate this error, three extrapolation methods can be considered: QCD evolution, $1/Q^2$, and a simple power law. The results of this analysis for several neutrino experiments are shown in Fig. 32. The world average is

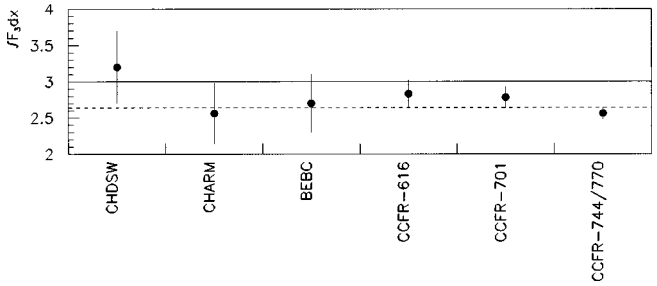

FIG. 32. Summary of measurements of the Gross-Llewellyn–Smith sum rule.

$$\int F_3 dx = 2.64 \pm 0.06, \tag{49}$$

which is consistent with the next-to-next-to-leading-order evaluation of Eq. (48) with $\Lambda = 250 \pm 50$ MeV.

The second method evaluates the integral by combining the xF_3 measurements of experiments covering different kinematic regions (Harris *et al.*, 1995). At high x, F_2 is nearly equal to xF_3. Therefore, to improve further the kinematic range at high x, one can use F_2 data from charged-lepton scattering for $x>0.5$.

An issue which can be best addressed using the second analysis technique is that of higher-twist contributions to the GLS integral. Because CCFR evaluates this integral in the low-Q^2 region where higher-twist contributions can contribute, an additional term ΔHT must be included in Eq. (48) (Larin and Vermarseren, 1991). This higher-twist contribution has been computed to be approximately $0.27/Q^2$ based on three independent calculations of the dynamical power corrections (Braun and Kolesnichenko, 1987). The three calculations are consistent with each other to $\sim 50\%$, so an error of $\pm 0.14/Q^2$ should be assumed for this result. A more recent result (Ross and Roberts, 1994) improved on the technique of Braun and Kolesnichenko (1987) by explicitly retaining extra terms dropped in the earlier analysis. As a result, the extracted value is more reliable, leading to a smaller theoretical error $[(0.16\pm 0.01)/Q^2$; Ross *et al.*, 1994].

b. The Adler sum rule

The Adler sum rule predicts the difference between the quark densities of the neutron and the proton, integrated over x. To leading order,

$$\int_0^1 [F_2^{\nu n}(x,Q^2)-F_2^{\nu p}(x,Q^2)]\frac{dx}{x} = \int_0^1 2[u_V(x)-d_V(x)]dx = 2. \tag{50}$$

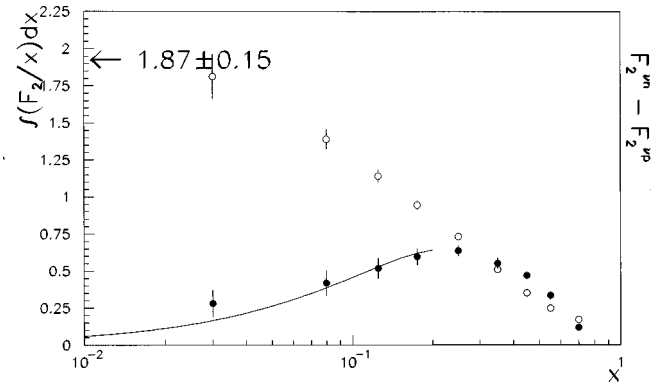

FIG. 33. Evaluation of the Adler sum rule using the data from BEBC: ●, $F_2^{\nu n}-F_2^{\nu p}$ evolved to $Q^2=5$ GeV^2; solid line, the fit to the low-x data; ○, the integral, $\int[F_2^{\nu n}(x)-F_2^{\nu p}(x)]/x\,dx$, from each bin to $x=1$ referred to as $\int(F_2/x)dx$ on the left-hand axis. Using the fit to evaluate the integral for $x<0.01$, the sum rule is found to be 1.87 ± 15.

The only assumption introduced in this calculation is that the quark and antiquark seas are equal; there is no assumption concerning the equality of, for example, the $\overline{u}$ and $\overline{d}$ seas.

Using the $F_2^{\nu p}$ and $F_2^{\nu n}$ data shown in Fig. 19, BEBC has demonstrated that the Adler sum rule is consistent with 2.0 (Allasia *et al.*, 1985). For this review, we have evolved the $F_2^{\nu n}-F_2^{\nu p}$ measurements to $Q^2=5$ GeV^2, as shown in Fig. 33 (closed points). We then evaluate the Adler sum rule under two assumptions for the low-x behavior. For the first method, we assume that the lowest bin is a constant equal to the value of the lowest-x data point. In this case, the integral is 2.05 ± 0.15 at $Q^2=5$. Alternatively, for the second method, we fit for the low-x behavior using the polynomial shown by the solid line. Using this polynomial to evaluate the integral for $0<x<0.01$, we obtain 1.87 ± 0.15, which is also within 1σ of the expectation.

The comparable sum rule for charged-lepton scattering is the Gottfried Sum Rule (Gottfried, 1967):

$$\int_0^1 [F_2^{\mu n}(x,Q^2)-F_2^{\mu p}(x,Q^2)]\frac{dx}{x} = \int_0^1 [u(x)-d(x)](e_u^2-e_d^2)dx=\frac{1}{3}, \tag{51}$$

where e_u^2 and e_d^2 are the charges of the u and d quarks. Inherent in this form of the Gottfried sum rule is the assumption that the $\overline{u}$ distribution is equal to the $\overline{d}$ distribution. There is no *a priori* reason to expect a difference in these distributions, and there was therefore some surprise when the NMC experiment measured the Gottfried sum to be 0.240 ± 0.016 (Allasia *et al.*, 1990). This result could be explained if $\overline{u}\neq\overline{d}$. Note that this assumption $\overline{u}=\overline{d}$ was not required in the Adler sum rule.

IV. NEUTRINO CHARM PRODUCTION: MEASUREMENTS OF THE STRANGE SEA, CHARM SEA, AND $|V_{CD}|$

A. Introduction

As shown in the previous sections, neutrino deep-inelastic scattering is particularly well suited for measuring the parton densities due to the neutrino's ability to resolve the flavor of the nucleon constituents. In addition, neutrino scattering is an effective way to study the dynamics of heavy-quark production, due to the light-to-heavy-quark transition at the charged-current vertex. In particular, neutrino charm production can be used to isolate the nucleon strange-quark distributions, $xs(x)$ and $x\overline{s}(x)$, and study the transition to the heavy charm quark. The strange-quark distribution function is of particular theoretical interest, since it may contribute to the low-Q^2 properties of the nucleon in the nonperturbative regime. Charm production is also an important testing ground for next-to-leading-order perturbative QCD due to the large contribution from gluon-initiated diagrams. In addition, understanding the threshold behavior associated with the heavy charm mass is critical to the extraction of the weak mixing angle, $\sin^2\theta_W$, from neutrino neutral-current data, as described in the next section.

One distinctive signature for the production of charmed quarks in neutrino- and antineutrino-nucleon scattering is the presence of two oppositely charged muons. [Studies of same-sign dimuon production have shown that the observed signal is completely dominated by nonprompt background sources, which preclude any quantitative physics measurements (Sandler *et al.*, 1993).] In the case of neutrino scattering, the underlying process is a neutrino interacting with an s or d quark, producing a charm quark that fragments into a charmed hadron. The charmed hadron's semileptonic decay ($BR=\approx10\%$) produces a second muon of opposite sign from the first:

$$\nu_\mu+\mathrm{N}\rightarrow\mu^-+c+\mathrm{X} \hookrightarrow s+\mu^++\nu_\mu. \tag{52}$$

The analogous process with an incident antineutrino proceeds through an interaction with an $\overline{s}$ or $\overline{d}$ antiquark, again leading to oppositely signed muons in the final state:

$$\overline{\nu}_\mu+\mathrm{N}\rightarrow\mu^++\overline{c}+\mathrm{X} \hookrightarrow \overline{s}+\mu^-+\overline{\nu}_\mu. \tag{53}$$

The heavy charm quark is expected to introduce an energy threshold in the dimuon production rate. This effect has been described in the past through the "slow rescaling" model (Barnett, 1976; Georgi and Politzer, 1976), in which ξ^0, the momentum fraction carried by the struck quark, is related to the kinematic variable $x=Q^2/2M\nu$ by the expression $\xi^0=x(1+m_c^2/Q^2)$, where m_c is the mass of the charm quark. (A more complete treatment of the kinematics associated with heavy-quark production modifies this model slightly, as discussed be-

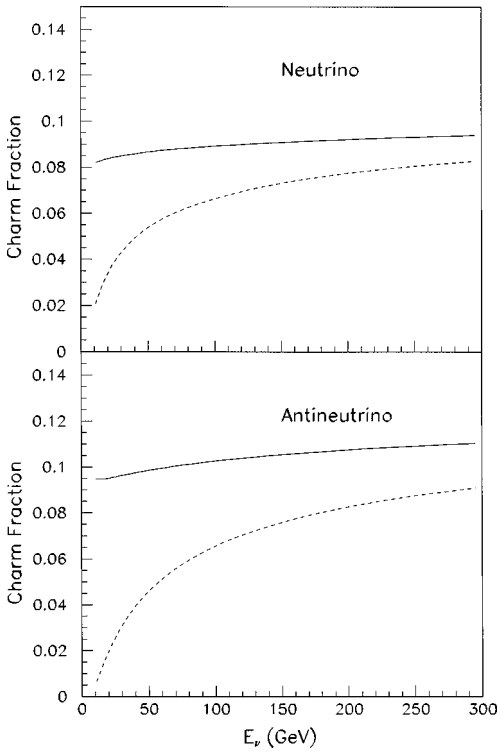

FIG. 34. Fraction of the neutrino (antineutrino) total cross section that is associated with charm production: dashed curves, leading-order calculation with $m_c=1.31$ GeV; solid curves, the same calculation with $m_c=0$.

low.) Charm production by neutrinos (or antineutrinos) is a substantial fraction of the total cross section and grows from threshold to about 10% at high energy, as shown in Fig. 34.

Neutral-current scattering off the charm sea can be isolated and studied by looking for the production of wrong-sign single muons in the interaction of a relatively pure ν_μ beam. This is one of the only techniques for probing the charm content in the nucleon, which is assumed in the standard calculation to evolve from zero at a threshold $Q^2\approx 4\ \mathrm{GeV}^2$. The process for study is neutrino neutral-current scattering off a charm quark followed by the semileptonic decay of the charm quark into a wrong-sign muon. The size of this process is therefore dependent on the number and distribution of charm quarks in the nucleon. The main backgrounds come from the $\bar{\nu}_\mu$ contamination in the beam and decays of secondary pions or kaons in the hadronic shower. The signal is smaller than the background, and at present only upper limits on the size of the charm sea are available.

B. Differential cross section for dimuon production and heavy-quark effects

The differential cross section for dimuon production is expressed generally as

$$\frac{d^3\sigma(\nu_\mu N\to\mu^-\mu^+X)}{d\xi dy\,dz} = \frac{d^2\sigma(\nu_\mu N\to cX)}{d\xi\,dy}D(z)B_c(c\to\mu^+X), \tag{54}$$

where the function $D(z)$ describes the hadronization of charmed quarks into D mesons with $z=p_D/p_D^{\max}$, and B_c is the weighted average of the semileptonic branching ratios of the charmed hadrons produced in neutrino interactions.

The heavy charm quark introduces an energy dependence in the charm production rate and also affects the measured angular (or y) distribution compared to that expected for a massless quark. (Additional thresholds related to the masses of final-state charmed mesons and baryons are present, but only become important near production threshold.) These are kinematic effects for which ξ, the momentum fraction of the struck quark, is related to the Bjorken scaling variable x through the expression (Aivazis, Collins *et al.*, 1994; Aivazis, Olness, and Tung, 1994)

$$\xi=\left(\frac{1}{2x}+\sqrt{\frac{1}{4x^2}+\frac{M^2}{Q^2}}\right)^{-1} \times\frac{Q^2-m_s^2+m_c^2+\Delta(-Q^2,m_s^2,m_c^2)}{2Q^2}, \tag{55}$$

where m_c is the charm quark mass and m_s refers to the initial-state quark mass, either the strange quark or the down quark, and $\Delta(-Q^2,m_s^2,m_c^2)$ is the triangle function, defined by

$$\Delta(a,b,c)\equiv\sqrt{a^2+b^2+c^2-2(ab+bc+ca)}.$$

The full expression for ξ can be simplified by neglecting the small effect of the initial-state quark mass to yield

$$\xi^0=x\left(1+\frac{m_c^2}{Q^2}\right)\left(1-\frac{x^2M^2}{Q^2}\right). \tag{56}$$

Relating ξ and x through the charm quark mass is referred to as "slow rescaling" (Barnett, 1976; Georgi and Politzer, 1976). A comparison of the full ξ calculation to the simple ξ^0 expression given above yields a difference of 10% (2%) for $x=0.2$ and $Q^2=1.0(5.0)$ GeV^2; this difference is much smaller at lower x and higher Q^2.

At leading order charm is produced by scattering directly off of strange and down quarks in the nucleon. The leading-order differential cross section for an isoscalar target, neglecting target-mass effects, is given by

$$\left[\frac{d^2\sigma(\nu_\mu N\to cX)}{d\xi\,dy}\right]_{LO} =\frac{G_F^2ME_\nu}{\pi(1+Q^2/M_W^2)^2}\{[\xi u(\xi,\mu^2)+\xi d(\xi,\mu^2)]|V_{cd}|^2 +2\xi s(\xi,\mu^2)|V_{cs}|^2\}\left(1-\frac{m_c^2}{2ME_\nu\xi}\right), \tag{57}$$

where $\xi u(\xi,\mu^2)$, $\xi d(\xi,\mu^2)$, and $\xi s(\xi,\mu^2)$ represent the momentum distributions of the u, d, and s quarks

within the proton at the scale μ^2 (the corresponding $\overline{\nu}_\mu$ process has the quarks replaced by their antiquark partners). $|V_{cd}|$ and $|V_{cs}|$ are the CKM matrix elements. The dependence of the parton distributions on the scale μ^2 is specified by QCD (Gribov and Lipatov, 1972; Altarelli and Parisi, 1977; Dokshitser *et al.*, 1978; Dokshitser *et al.*, 1980), but the precise dependence of μ^2 on Q^2 and x is somewhat arbitrary in finite-order perturbation theory. The finite charm mass included in the $(1-m_c^2/2ME_\nu\xi)$ expression induces an effective Callan-Gross violation such that $R_L^{\text{LO charm}}(\xi,Q^2)\simeq 1+m_c^2/Q^2$. In the modified leading-order analysis of Rabinowitz *et al.* (1993), Callan-Gross violation is included by replacing the term $[1-m_c^2/(2ME_\nu\xi)]$ in Eq. (57) with

$$1-m_c^2/(2ME_\nu\xi)\rightarrow \frac{1+R_L(\xi,Q^2)}{1+(2M\xi/Q)^2} \times[1-y-Mxy/(2E_\nu)+xy/\xi], \tag{58}$$

using external measurements of the structure function $R_L(\xi,Q^2)$ (Dasu *et al.*, 1988a, 1988b). In the next-to-leading-order formalism, violation of the Callan-Gross relation emerges as a consequence of the more complete QCD calculation.

The leading-order expression illustrates the sensitivity of the process to the strange-quark sea. Charm or anticharm production from scattering off d or $\overline{d}$ quarks is Cabibbo suppressed. In the case of charm produced by neutrinos, approximately 50% is due to scattering from s quarks, even though the d-quark content of the proton is approximately ten times larger. In the case of antineutrino scattering, where $\overline{d}$ quarks from the sea contribute, roughly 90% is due to scattering off $\overline{s}$ quarks.

C. Next-to-leading-order corrections

Because neutrino charm production has a large sea-quark component at leading order, the next-to-leading-order gluon-initiated contributions are significant (Aivazis *et al.*, 1990). Gluon-initiated production of charm proceeds through both the t and u channels as shown in Fig. 35(a). The size of the gluon distribution, which is an order of magnitude larger than the sea-quark distribution, compensates for the extra power of α_S involved in the gluon-initiated diagram. The next-to-leading-order quark-initiated diagrams, shown in Fig. 35(b), in which a gluon is radiated, also enter the perturbative expansion at $\mathcal{O}(\alpha_S)$, but the corrections from these diagrams to the cross section are small. Several calculations including the next-to-leading-order formalism have been done (Van der Bij and van Oldenborgh, 1991; Kramer and Lampe, 1992; Aivazis, Collins, *et al.*, 1994; Aivazis, Olness, and Tung, 1994). The treatment of the gluon-initiated diagrams in these has been cross-checked and found to be consistent.

As with all applications of perturbative QCD, a theoretical uncertainty is associated with the choice of factorization and renormalization scales. Some scale dependence is unavoidable for any calculation done to finite order in α_S. Most analyses assume that the factorization and renormalization scales are both equal to a single parameter, μ. The μ scale is interpreted as setting the boundary between the collinear and noncollinear regions of the $p_\perp$ integration over the final states, where $p_\perp$ is the transverse momentum of the initial-state quark coming from the gluon splitting. Therefore a scale proportional to $p_\perp^{\max}=\Delta(W^2,m_c^2,M^2)/\sqrt{4W^2}$ is suggested by Aivazis *et al.* (Aivazis, Collins, *et al.*, 1994; Aivazis, Olness, and Tung, 1994). Figure 36 shows the scale dependence of the differential cross section for charm production, where the abscissa is in units of $p_\perp^{\max}$. The scale dependence is weak for values above one unit of $p_\perp^{\max}$, but there is a strong dependence when μ is below this value.

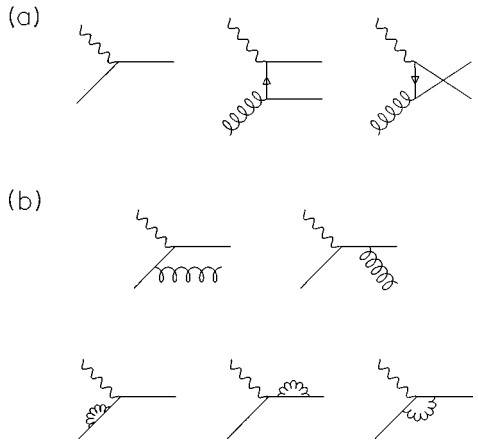

FIG. 35. Mechanisms that contribute to neutrino production of charm up to $\mathcal{O}(\alpha_S)$: (a) the dominant diagrams—the leading-order quark-initiated diagram and the t channel and u channel gluon-initiated diagrams, respectively; (b) the radiative gluon and self-energy diagrams.

D. Experimental issues for dimuon measurements

1. Data samples and event selection

Many experiments have investigated neutrino and antineutrino production of charm since it was first observed in 1974 (Benvenuti *et al.*, 1975). The experiments considered here include the highest-statistics experiments using each of the main experimental techniques. Most of the experiments have been described in Sec. I.D, and only details relevant to charm measurements will be given here. The largest data samples are available from the CCFR (Bazarko *et al.*, 1995) and CDHS (Abramowicz *et al.*, 1982) experiments. The CCFR collaboration used a high-energy, quadrupole-triplet neutrino beam and a massive, high-density steel detector at the Fermilab Tevatron. The CDHS collaboration at CERN used a magnetized steel target calorimeter illuminated by a horn-focused neutrino beam with a somewhat lower-energy spectrum. Results are also available from the Fermilab 15-ft bubble-chamber experiment for $\mu^- e^+$ events (Baker *et al.*, 1991). In this experiment, the

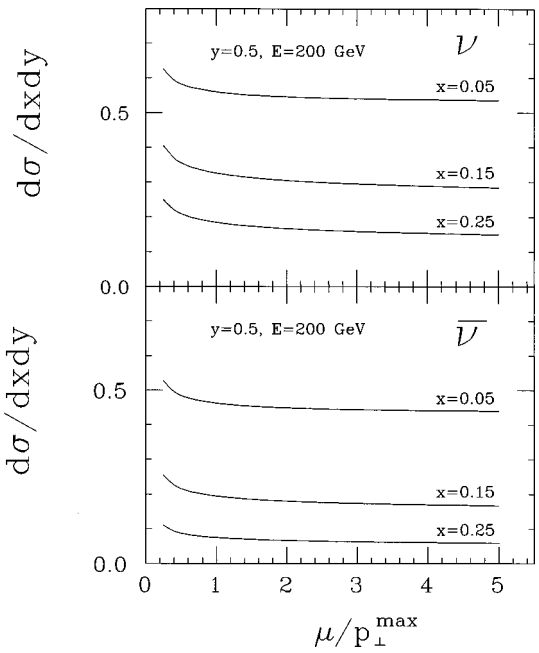

FIG. 36. The μ^2 scale dependence of the differential cross section for neutrino and antineutrino production of charm, where μ^2 identifies the factorization and renormalization scales. The scale on the abscissa is in units of $p_\perp^{\max}$. For $E=200$ GeV and $y=0.5$, the $x=0.05$, 0.15, 0.25 lines correspond to $p_\perp^{\max}=6.6$, 6.2, 5.8 GeV/c, respectively.

low threshold, $p_{e^+}>0.3$ GeV, combined with good statistics for $E_\nu<30$ GeV, gives good sensitivity to the slow-rescaling threshold behavior. The final data set considered is the E531 neutrino emulsion experiment (Ushida *et al.*, 1988a, 1988b) at Fermilab, which measures inclusive charm particle production directly by identifying the charm decay in the emulsion. Thus this experiment can provide information on the charm species produced by neutrinos and the kinematics of the production. Table V summarizes the neutrino charm production data samples from these experiments.

2. Nonprompt and other background sources of dimuons

For the CCFR and CDHS experiments, nonprompt pion and kaon decays constitute the main background to the charm-initiated signal. The high density of their target calorimeters minimizes this contamination due to the short interaction length of the detector. The background is estimated from Monte Carlo calculations and test-beam measurements of muon production in hadron showers. The systematic uncertainty in this background has been estimated (Sandler *et al.*, 1993) by the CCFR collaboration to be 15%(20%) for $\nu(\overline{\nu})$-induced showers and comes mainly from uncertainties in the secondary particle production spectrum including heavy nuclear target effects. For the 15-ft bubble-chamber experiment, the background is from Dalitz decays of π^0 mesons and other γ conversions. Finally, the E531 emulsion experiment has a small background from noncharm events that pass their charm identification cuts. The background level for each experiment is listed in Table V.

3. Charm quark production, fragmentation, and experimental acceptance

The production and fragmentation of the charm quark into charmed hadrons must be modeled in order to extract information from the observed dilepton events. For the leading-order formalism, the kinematic suppression due to the mass of the charm quark, m_c, is included in Eq. (57) and the charm quark direction is defined by the $W^+q\to c$ kinematics.

The gluon-initiated diagrams in the next-to-leading-order calculation proceed by $W^+g\to c\overline{s}$ as shown in Fig. 35(a). This next-to-leading-order production proceeds through both the t and the u channels, which dominate different regions of phase space. In the t channel, the gluon splits into an $s\overline{s}$ pair and the c quark emerges from the W-boson vertex. In the u channel, the legs of the c and $\overline{s}$ quarks are crossed—the gluon splits into a $c\overline{c}$ pair and the $\overline{s}$ quark emerges from the W-boson vertex. In the W-boson–gluon center-of-mass frame, the c quark is produced at an angle θ_c^* relative to the W-boson direction. The production angle is related to the momentum of the c quark in the laboratory. When θ_c^* is small—t channel dominance—the c quark carries most of the W-boson momentum. As θ_c^* approaches π—u channel dominance—the c quark emerges with little momentum in the laboratory. Acceptance correc-

TABLE V. Summary of data samples from some neutrino charm production experiments. The CDHS and CCFR experiments detect dimuon events, the 15-ft Bubble Chamber measures μ-e events, and the E531 experiment detects the inclusive decays of charmed particles in an emulsion target.

Experiment	E_ν (GeV)	μ^-l^+ events	μ^+l^- events	Background (%)
CCFR (Bazarko *et al.*, 1995)	30–600	5030	1060	15
$p_{\mu_2}>5$ GeV	(>100)	(3721)	(493)	
CDHS (Abramowicz *et al.*, 1982)	30–250	11041	3684	13
$p_{\mu_2}>5$ GeV	(>100)	(3589)	(452)	
15-ft BC (Baker *et al.*, 1991)	1–200	461	-	18
$p_{e^+}>0.3$ GeV				
E531 (Ushida *et al.*, 1988)	1–250	122	-	3
ν-Emulsion		(Charm Events)		

tions that are dependent on θ_c^* need to be included in the analysis of any experimental measurement; these corrections are largest at high θ_c^* where the decay products of the outgoing c quark are hard to detect.

The charm quark fragmentation uncertainties are a second important source of systematic error for the dilepton physics measurements. The fragmentation of the charm quark into D mesons is typically parametrized using the Collins and Spiller function (Collins and Spiller, 1985),

$$D(z)=N[(1-z)/z+\epsilon_C(2-z)/(1-z)](1+z)^2 \times[1-(1/z)-\epsilon_C/(1-z)]^{-2}; \quad (59)$$

older measurements also employed the Peterson function (Peterson *et al.*, 1983),

$$D(z)=\frac{N}{z[1-(1/z)-\epsilon_P/(1-z)]^2}, \quad (60)$$

where $z=p_D/p_D^{\max}$ is the fraction of its maximum possible momentum that the D meson carries and the ϵ parameters determine the shape of the distribution. In principle, e^+e^- collider data could provide precise data on the ϵ parameters. However, because of uncertainties due to the different quark environment in e^+e^- relative to neutrino scattering, the ϵ parameters in the fragmentation models are best determined from fits to neutrino charm production data. Fits to the charm particle spectrum in the E531 data (Ushida *et al.*, 1988) give $\epsilon_P=0.18\pm0.06$, and fits to the CCFR $z_{\rm vis}=E_{\mu_2}/(E_{\mu_2}+E_{\rm had})$ distribution, where E_{μ_2} is the energy of the second muon, yield $\epsilon_C=0.81\pm0.14$ (Bazarko *et al.*, 1995) [or $\epsilon_P=0.22\pm0.05$ (Rabinowitz *et al.*, 1993)]. These can be compared to the CLEO measurements (Bortoletto *et al.*, 1988): The Collins and Spiller function fits the CLEO data well, with $\epsilon_C=0.64\pm0.14$, but the Peterson function does not reproduce the data for any value of ϵ_P. The CDHS collaboration in their dimuon analysis (Abramowicz *et al.*, 1982) parametrized the charm fragmentation phenomenologically by functions ranging from a delta function at $z=0.68$ to a flat distribution.

The semileptonic decay of the charmed particles also needs to be modeled, and the effect of missing energy from the outgoing neutrino needs to be included. For this modeling, the three-body decay kinematics is taken from e^+e^- collider studies including the differences for the various charmed-particle species. The composition of charmed particles produced in neutrino interactions has been measured by the E531 ν-emulsion experiment (Ushida *et al.*, 1988). With an $E_\nu>30$ GeV cut, the production is dominated by neutral and charged D mesons.

E. Dimuon measurements and results

1. Charm production rate

The energy dependence of the neutrino charm production rates provides a direct test of the modeling of the heavy charm quark production and the thresholds appropriate for the charm particles in the final states. At low energy, $E_\nu<20$ GeV, quasielastic scattering, such as $\nu_\mu n\to\mu^-\Lambda_c^+$, is a large fraction of the charm production and accounts for more than 25% of the charm cross section. Above 50 GeV, the exclusive final-state effects become small (below 5%) and the simple parton model approach in which the production and hadronization factorizes becomes valid. Comparing the predicted energy dependence expected from the slow-rescaling model with measured rates corrected for acceptance, smearing, and other kinematic cuts shows good agreement between the data and model for the CCFR, 15-ft Bubble Chamber and E531 experiments, as shown in Fig. 37. The CDHS data, however, are somewhat below the prediction and the other data, especially at low energy.

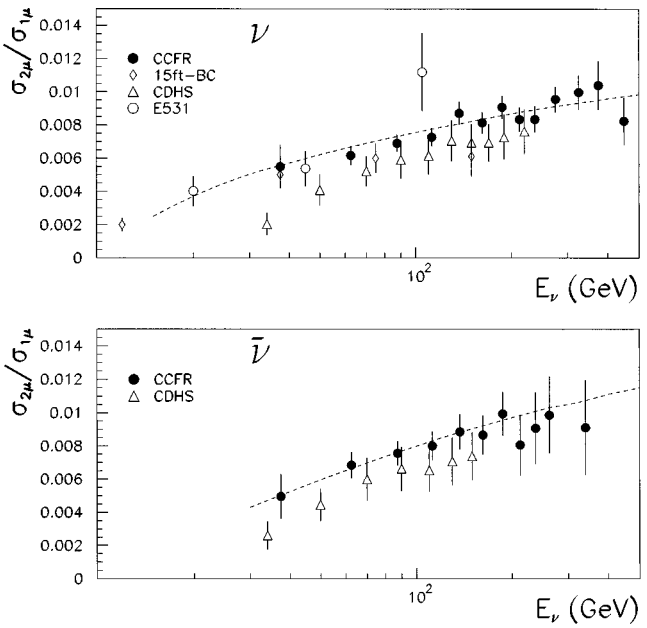

FIG. 37. The dimuon-to-single-muon rate, corrected for acceptance, smearing, and minimum second muon energy cut vs neutrino energy for the CCFR and CDHS experiments. Also shown is the 15-ft Bubble Chamber rate ratio for μe to single-muon events and the E531 emulsion experiment where the charm rate has been multiplied by a semileptonic branching ratio of 0.11. The dashed curve is a leading-order slow-rescaling model prediction with $m_c=1.31$ GeV. (The errors on the CDHS points include uncertainties in fragmentation and normalization; the other points do not.)

After correcting for the slow-rescaling threshold corresponding to an appropriate m_c, the rates become less dependent on E_ν, exhibiting only the sharp, low-energy threshold behavior associated with the production of heavy charmed mesons [$W^2>(M_D+M)^2$]. The CCFR data shown in Fig. 38 are in good agreement with this model for a charm quark mass of $m_c=1.31$ GeV/c^2. In the next section, the energy dependence of charm production will be used to determine m_c.

2. Extraction of the strange sea $xs(x,\mu^2)$ and charm mass m_c

The CCFR collaboration has done both a leading-order (Rabinowitz *et al.*, 1993) and next-to-leading-

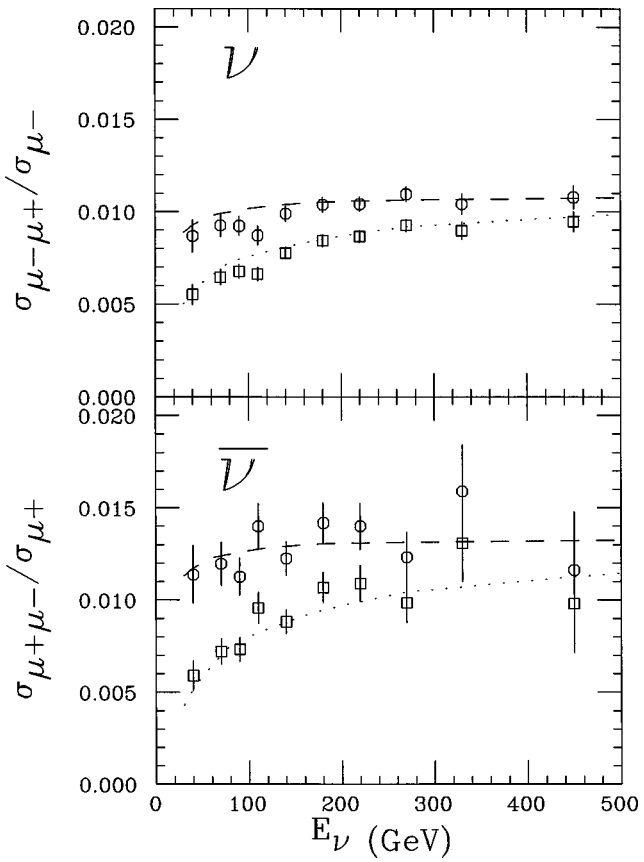

FIG. 38. Opposite-sign dimuon rates vs E_ν for the CCFR ν_μ (top) and $\overline{\nu}_\mu$ (bottom) data: □, rates corrected for acceptance, smearing, and kinematic cuts; ○, rates corrected for slow rescaling with $m_c=1.31$ GeV; dotted curve, the leading-order model prediction with $m_c=1.31$ GeV before correcting for the finite charm mass but including charm particle mass effects; dashed curve, same $m_c=1.31$ GeV prediction after correcting for the finite charm mass.

order (Bazarko *et al.*, 1995) analysis of their dimuon data samples. For these analyses, the single-muon and dimuon events were simulated using Monte Carlo techniques and compared to the observed dimuon distribution to extract the various physics parameters. Quark and antiquark momentum densities were obtained from the measured CCFR structure functions (Leung *et al.*, 1993; Quintas *et al.*, 1993) using the following procedure.

The F_2 and xF_3 structure functions are used to determine the singlet, $xq^S(x,\mu^2)=xq(x,\mu^2)+x\overline{q}(x,\mu^2)$, nonsinglet, $xq^{\rm NS}(x,\mu^2)=xq(x,\mu^2)-x\overline{q}(x,\mu^2)$, and gluon, $xG(x,\mu^2)$, distributions. These distributions are obtained from leading-order or next-to-leading-order QCD fits to the structure-function data, described in Seligman *et al.* (1997a, 1997b), using the QCD evolution programs of Buras and Gaemers (1978) or Duke and Owens (1984), respectively.

To resolve the strange component of the quark sea, the singlet and nonsinglet quark distributions are separated by flavor. Insofar as isospin is a good symmetry, the experiment is insensitive to the exact form of the up and down valence- and sea-quark distributions, because the neutrino target is composed of iron, which is nearly isoscalar. An isoscalar correction accounts for the 5.67% neutron excess in the iron target. The proton valence-quark content, $xq_V(x,\mu^2)=xq^{NS}(x,\mu^2)$, is parametrized by

$$xq_V(x,\mu^2)=xu_V(x,\mu^2)+xd_V(x,\mu^2),$$
$$xd_V(x,\mu^2)=A_d(1-x)xu_V(x,\mu^2), \tag{61}$$

where the shape difference for $xd_V(x)$ better fits charged-lepton scattering measurements of $F_2^{e(\mu)n}/F_2^{e(\mu)p}$ (Amaudruz *et al.*, 1992a). A_d is fixed by requiring that the ratio of the number of d to u valence quarks in the proton be 1/2. The nonstrange quark and antiquark components of the sea are assumed to be symmetric, so that $x\overline{u}(x,\mu^2)=xu_S(x,\mu^2)$, $x\overline{d}(x,\mu^2)=xd_S(x,\mu^2)$. The isoscalar correction is applied assuming $x\overline{u}(x,\mu^2)=x\overline{d}(x,\mu^2)$.

The strange component of the quark sea is allowed to have a different magnitude and shape from the nonstrange component. The strange-quark content is set by the parameter

$$\kappa=\frac{\int_0^1[xs(x,\mu^2)+x\overline{s}(x,\mu^2)]dx}{\int_0^1[x\overline{u}(x,\mu^2)+x\overline{d}(x,\mu^2)]dx}, \tag{62}$$

where $\kappa=1$ would indicate a flavor SU(3) symmetric sea. The shape of the strange-quark distribution is related to that of the nonstrange sea by a shape parameter α, where $\alpha=0$ would indicate that the strange sea had the same x dependence as the nonstrange component of the quark sea. Assuming that $xs(x,\mu^2)$ and $x\overline{s}(x,\mu^2)$ are the same, the sea-quark distributions are then parametrized by

$$x\overline{q}(x,\mu^2)=2\left[\frac{x\overline{u}(x,\mu^2)+x\overline{d}(x,\mu^2)}{2}\right]+xs(x,\mu^2),$$
$$xs(x,\mu^2)=A_s(1-x)^\alpha\left[\frac{x\overline{u}(x,\mu^2)+x\overline{d}(x,\mu^2)}{2}\right], \tag{63}$$

where A_s is determined from Eq. (62) given for a given value of κ and α.

A χ^2 minimization is performed to find the strange-sea parameters κ and α, the values of B_c and m_c that appear in Eqs. (54) and (57), and the fragmentation parameter ϵ, by comparing the data and Monte Carlo $x_{\rm vis}$, $E_{\rm vis}$, and $z_{\rm vis}$ event distributions. [We use the subscript vis to denote values of the kinematic variables listed in Eq. (3), where $E_{\rm had}$ is set equal to the value with the missing decay neutrino energy subtracted, $E_{\rm had}^{\rm vis}=E_{\rm had}-E_{{\rm decay}\ \nu}=E_{\rm had}^{\rm meas}+E_{\mu 2}$.] Projections of data for each of these variables are compared with the next-to-leading-order fits (Bazarko *et al.*, 1995) in Figs. 39, 40, and 41. Taking $|V_{cd}|=0.221\pm0.003$ and $|V_{cs}|=0.9743\pm0.0008$ (Barnett *et al.*, 1996) as input values, the extracted CCFR leading-order and next-to-leading-order parameters with their statistical and systematic errors are presented in Table VI.

The CDHS collaboration (Abramowicz *et al.*, 1982) extracts the combination $|V_{cd}|^2B_c$ from the slow-

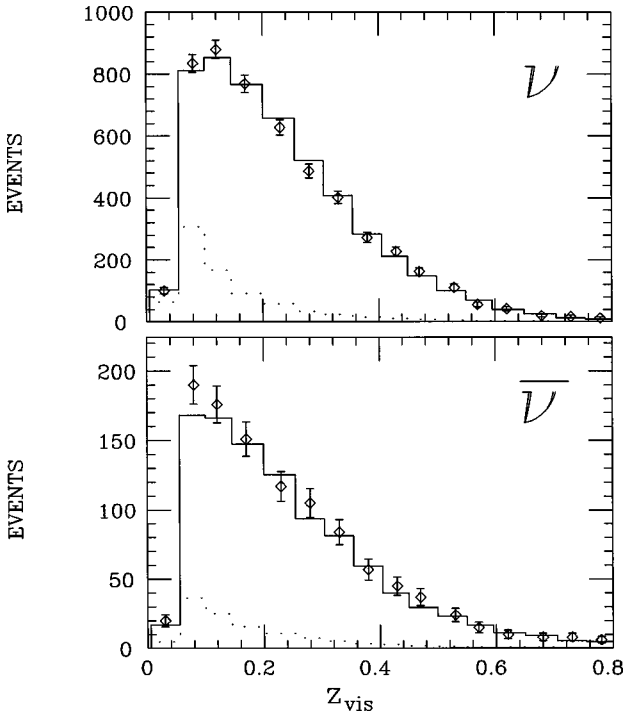

FIG. 39. The $z_{\rm vis}$ distribution for the CCFR ν- and $\overline{\nu}$-induced dimuon events. Data are given by the points, and the solid histogram is the result of fitting the dimuon event simulation. The dotted histogram is the background contribution to the former from pion and kaon decay.

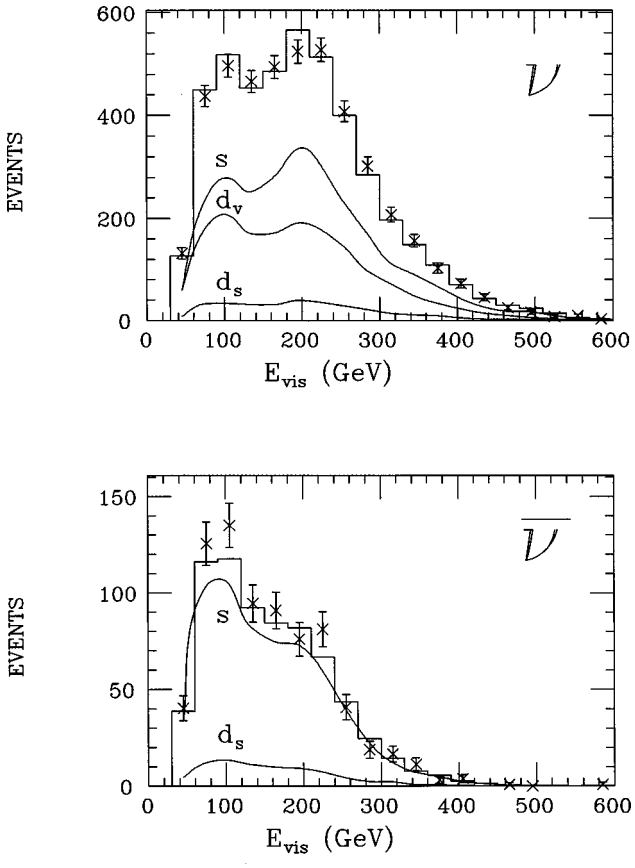

FIG. 40. The $E_{\rm vis}$ distribution for the CCFR ν- and $\overline{\nu}$-induced dimuon events after correction for π/K decay backgrounds and $\nu-\overline{\nu}$ misidentification. Data are given by the points, and the solid histogram is the result of fitting the dimuon event simulation. The quarks contributing to the histogram are indicated by the curves: s, the strange-sea component; d_V, the d valence component; d_S, the d sea component.

rescaling and acceptance-corrected dimuon rates at high energy, $E_\nu > 80$ GeV. The $\overline{\nu}_\mu$ rate is used to remove the strange-quark contribution to the ν_μ rate, leaving the down quark to charm quark contribution as follows:

$$|V_{cd}|^2 B_c = \frac{2}{3}\frac{R_\nu - r R_{\overline{\nu}}}{(1-r)} \tag{64}$$

where $R_{\nu(\overline{\nu})} = \sigma_{2\mu}^{\nu,\overline{\nu}}/\sigma_{1\mu}^{\nu,\overline{\nu}}$ and $r = \sigma_{1\mu}^{\overline{\nu}}/\sigma_{1\mu}^{\nu} = 0.48 \pm 0.02$.

In the CDHS analysis, the combination $\kappa|V_{cs}|^2/|V_{cd}|^2$ is found by a shape analysis of the observed $x_{\rm vis}$ distribution for neutrino-induced dimuons, where the distribution is separated into scattering off d or s quarks. The antineutrino dimuon data give the strange-quark distribution, and their measured charged-current structure functions give the distribution for down quarks. After including the fragmentation uncertainties, a 10% scale error, and variations in the charm mass between 1.2 and 1.8 GeV/c^2, the results are

$$|V_{cd}|^2 B_c = (4.10 \pm 0.70 \pm 0.16) \times 10^{-3} \quad \text{(CDHS)},$$

$$\kappa \frac{|V_{cs}|^2}{|V_{cd}|^2} = 9.3 \pm 1.6 \pm 0.9 \quad \text{(CDHS)},$$

where the first error is the total error except the m_c variation, which is given as the second error. Using the same CKM matrix elements as above, $|V_{cd}| = 0.221 \pm 0.003$ and $|V_{cs}| = 0.9743 \pm 0.0008$ (Barnett *et al.*, 1996), one can convert these values to the measurements of B_c and κ shown in Table VI.

3. Discussion of results

Parton distributions are defined to a given order and scheme in QCD. Therefore the magnitude of a given parton distribution differs between leading order and next-to-leading-order. The parameters α and m_c show shifts between leading order and next-to-leading order, but κ and B_c are similar. For the CCFR next-to-leading-order analysis, the nucleon strange-quark content is found to be $\kappa = 0.477 \pm 0.051$, indicating that the sea is not SU(3) symmetric. This is qualitatively the same result as from the leading-order analysis of CCFR and CDHS.

Since a nonzero value of α would indicate a shape difference between $x\overline{q}(x)$ and $xs(x)$, the CCFR next-to-leading-order value $\alpha = -0.02^{+0.66}_{-0.60}$ indicates no shape difference at next-to-leading order. At leading order, CCFR finds the strange quarks softer than the overall quark sea. This comes about in part because the CCFR leading-order analysis includes a longitudinal component, $R_L(\xi, Q^2)$, in both the inclusive charged-current and charm production differential cross section, as shown in Eq. (58). This procedure is an approximation and does not correctly treat the differences in the longi-

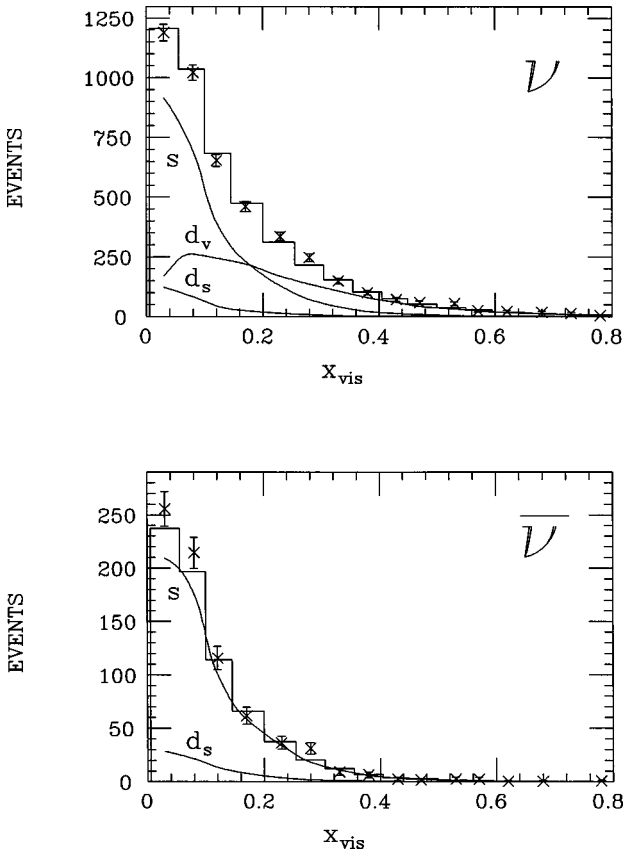

FIG. 41. The $x_{\rm vis}$ distribution for the CCFR ν- and $\overline{\nu}$-induced dimuon events after correction for π/K decay backgrounds and ν-$\overline{\nu}$ misidentification. Data are given by the points, and the solid histogram is the result of fitting the dimuon event simulation. The quarks contributing to the histogram are indicated by the curves: s, the strange-sea component; d_V, the d valence component; d_s, the d sea component.

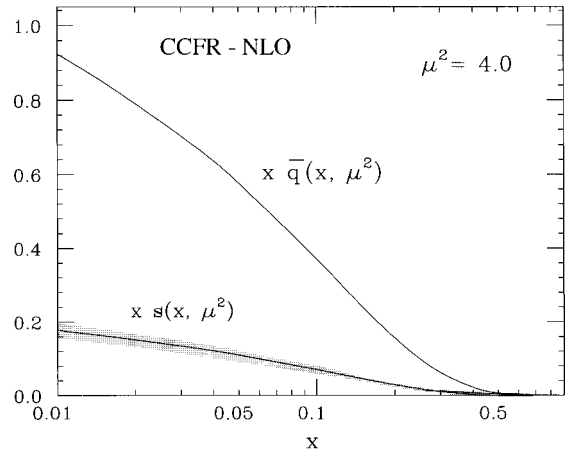

FIG. 42. The quark and strange-sea distributions, $x\overline{q}(x,\mu^2)$ and $xs(x,\mu^2)$, at $\mu^2=4\,\mathrm{GeV}^2$ determined from the CCFR next-to-leading-order analysis. The band around the next-to-leading-order strange-sea distribution indicates the $\pm1\sigma$ uncertainty in the distribution.

tudinal component for heavy- and light-quark production. On the other hand, the next-to-leading-order formalism does include these mass effects correctly and should give reliable measurements of the $x\overline{q}(x)$ and $xs(x)$ seas. Figure 42 compares the results for the quark and strange seas determined by the next-to-leading-order CCFR analysis, which shows that the magnitude is different but the shape is the same.

The charm quark mass parameter from the CCFR next-to-leading-order fit is 1.70 ± 0.19 GeV, which differs from the leading-order result. As shown in Sec. IV.E.1, the leading-order analysis with the slow-rescaling correction for the heavy charm quark is able to parametrize the threshold behavior of the measured process. On the other hand, the next-to-leading-order value of m_c, while also describing the threshold behavior well, correctly includes the kinematic effects associated with heavy-quark production and provides a better comparison with measurements derived from other processes involving similar higher-order perturbative QCD calculations. For example, the photon-gluon-fusion analysis of photoproduction data of Anjos *et al.* (1990) finds $m_c=1.74^{+0.13}_{-0.18}$ GeV, which is in agreement with the next-to-leading-order neutrino value.

Glück, Kretzer, and Reya (Glück *et al.*, 1996) have erroneously claimed that the acceptance correction was applied incorrectly in the CCFR next-to-leading-order

TABLE VI. Next-to-leading-order and leading-order fit results, assuming $xs(x)=x\overline{s}(x)$. Errors are statistical and systematic, except that the errors on the fragmentation parameters are statistical only.

	Fragmentation	χ^2/DOF	κ	α	B_c	m_c (GeV)
CCFR (Bazarko *et al.*, 1995)	Collins-Spiller	52.2/	0.477	-0.02	0.1091	1.70
NLO fit	$\epsilon_C=0.81\pm0.14$	65	$\pm0.045\pm0.024$	$\pm0.57\pm0.27$	$\pm0.0078\pm0.0057$	$\pm0.17\pm0.09$
CCFR (Bazarko *et al.*, 1995)	Peterson	41.2/	0.468	-0.05	0.1047	1.69
NLO fit	$\epsilon_P=0.20\pm0.04$	46	$\pm0.053\pm0.025$	$\pm0.47\pm0.27$	$\pm0.0076\pm0.0057$	$\pm0.16\pm0.11$
CCFR (Rabinowitz *et al.*, 1993)	Peterson	42.5/	0.373	2.50	0.1050	1.31
LO fit	$\epsilon_P=0.20\pm0.04$	46	$\pm0.045\pm0.018$	$\pm0.58\pm0.31$	$\pm0.007\pm0.005$	$\pm0.21\pm0.12$
CDHS (Abramowicz *et al.*, 1982)	δ-function		0.478	Not fit	0.0839	Not fit
LO fit	$(z=0.68)$		±0.094	Assumed 0.0	±0.0147	Varied 1.2–1.8

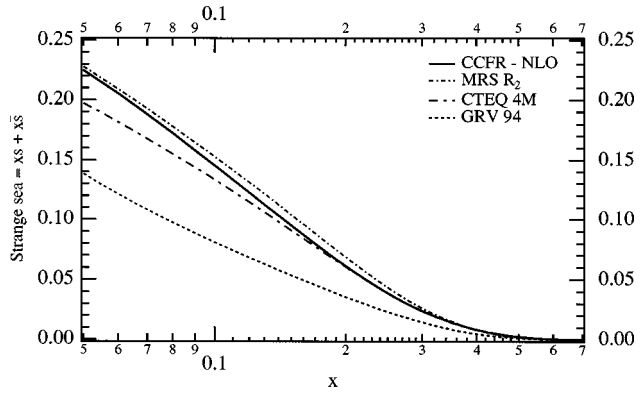

FIG. 43. The CCFR next-to-leading-order strange-sea distributions compared to CTEQ 4M, MRS R_2, and GRV 94 at $\mu^2=5$ GeV^2.

analysis (Bazarko *et al.*, 1995). In the analysis procedure of Aivazis *et al.* (Aivazis, Collins, *et al.*, 1994; Aivazis, Olness, and Tung, 1994), the cross section is divided into three terms: leading order, next-to-leading order, and subtraction. The CCFR analysis consistently corrects for all experimental acceptance effects using the proper kinematics for each term. For the leading-order and subtraction term, the underlying distribution corresponds to the appropriate $W^+s\rightarrow c$ kinematics. The acceptance for the next-to-leading-order term uses the $W^+g\rightarrow c\bar{s}$ kinematics with the calculated matrix element from Aivazis *et al.* (Aivazis, Collins, *et al.*, 1994; Aivazis, Olness, and Tung, 1994). Glück, Kretzer, and Reya also claim that the next-to-leading-order to leading-order difference is not supported by the currently available parton distribution functions (Glück *et al.*, 1995; Martin *et al.*, 1996; Lai *et al.*, 1997). As stated above, the CCFR leading-order analysis includes higher-order longitudinal cross-section components that make their parton distributions different from strict leading-order analyses. The most recent and complete CCFR next-to-leading order analysis (Seligman *et al.*, 1997a, 1997b) gives parton distributions that are consistent with those from the various global fits, as shown in Fig. 30. It is interesting to note that the most recent GRV 94 (Glück *et al.*, 1995) strange-sea distributions are much smaller than the CCFR next-to-leading-order measurements and the other global fit results, as shown in Fig. 43. Publication in the future of acceptance and smearing-corrected neutrino charm production cross sections or structure functions by the CCFR group will allow independent analyses and global fits using the different next-to-leading-order calculations.

The CCFR collaboration has also investigated the dependence of their next-to-leading-order results on factorization and renormalization scale uncertainties. Their standard results quoted in Table VI use $\mu=2p_\perp^{\max}$ for both scales and find the scale uncertainty by varying μ between $p_\perp^{\max}$ and $3p_\perp^{\max}$. Fit results with various choices of the common factorization and renormalization scale are presented in Table VII. These results indicate that the data favor μ^2 scales with smaller magnitudes but that the values of the fit parameters are fairly insensitive to the choice of scale.

4. Comparisons to other strange-sea measurements

The comparison of neutrino and charged-lepton measurements of the F_2 structure function (see Sec. III.D) can also be used to study the magnitude of the strange sea. In the deep-inelastic scattering renormalization scheme with $\mu^2=Q^2$, the strange sea is related to the two F_2 measurements by

$$\frac{1}{2}[xs(x,Q^2)+x\bar{s}(x,Q^2)]\simeq\frac{5}{6}F_2^{\nu N}(x,Q^2)-3F_2^{\mu N}(x,Q^2). \tag{65}$$

The CTEQ collaboration in their CTEQ 1MS parton distributions (Botts *et al.*, 1993) tried increasing the strange sea at low x to be consistent with Eq. (65). The strange sea from this procedure is much larger than the direct CCFR next-to-leading-order measurements (Bazarko *et al.*, 1995) and other parton distributions, CTEQ 2MS (Botts *et al.*, 1993), MRS H (Martin *et al.*, 1993), and GRV HO (Glück *et al.*, 1992), as shown in Fig. 44. It therefore seems unlikely that a larger strange sea is the explanation for the neutrino/charged-lepton difference

TABLE VII. Central values of the CCFR fit parameters for various choices of the QCD scale μ^2. Each fit contains 65 degrees of freedom.

Choice of scale, μ^2	χ^2	κ	α	B_c	m_c (GeV)
$(p_\perp^{\max})^2$	50.4	0.513	0.18	0.0987	1.71
$(2p_\perp^{\max})^2$	52.2	0.477	−0.02	0.1091	1.70
$(3p_\perp^{\max})^2$	54.4	0.460	−0.10	0.1142	1.68
Q^2	51.7	0.423	−0.37	0.1074	1.80
$(2Q)^2$	56.1	0.410	−0.46	0.1159	1.71
$(3Q)^2$	59.4	0.408	−0.54	0.1206	1.73
$Q^2+m_c^2$	52.5	0.421	−0.03	0.1066	1.65
$4(Q^2+m_c^2)$	57.1	0.409	−0.16	0.1154	1.64
$Q^2+(2m_c)^2$	52.8	0.428	0.00	0.1068	1.62
$4[Q^2+(2m_c)^2]$	57.3	0.415	−0.15	0.1161	1.63

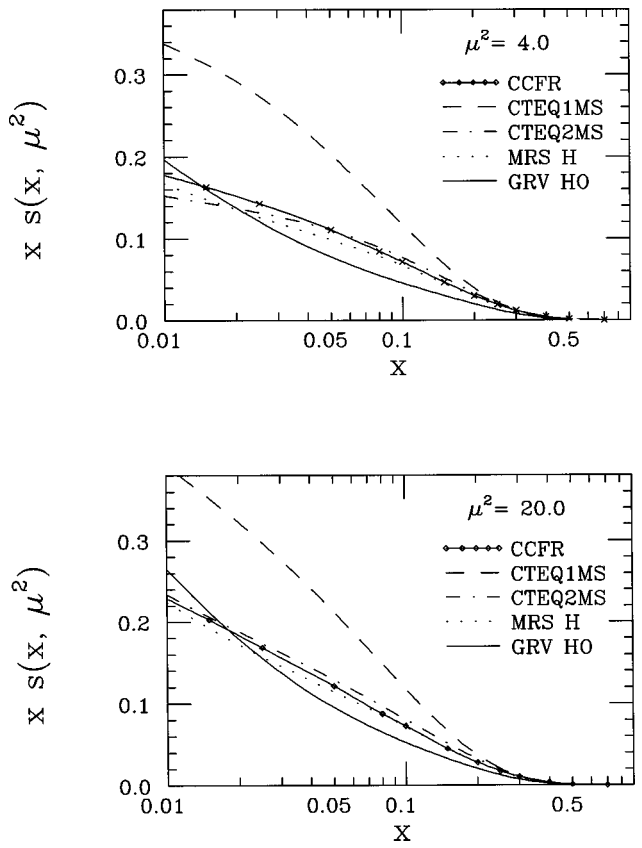

FIG. 44. Strange-quark distributions $x\,s(x,\mu^2)$ from the CCFR experiment and previous global fits by CTEQ, MRS, and GRV for $\mu^2=4$ and 20 GeV^2.

at low x. The same conclusion has been put forward by Glück *et al.* (1996), who state that if the CCFR (Seligman *et al.*, 1997a, 1997b) and NMC (Amaudruz *et al.*, 1992b) data are correct, this discrepancy "will constitute a major problem which cannot be solved within our present understanding of the so far successful perturbative QCD."

5. Tests of $xs(x)\neq x\bar{s}(x)$

In principle, the momentum distributions of s and $\bar{s}$ quarks need not be the same as long as the strangeness content of the nucleon is constrained to have equal numbers of s and $\bar{s}$ quarks. Theoretical work has explored the possibility that the nucleon contains a sizable heavy-quark component at moderate x—the possibility of so-called "intrinsic heavy-quark states" within the nucleon (Brodsky *et al.*, 1981; Brodsky and Ma, 1996). Postulating intrinsic strange particle states, such as a $K^+\Lambda$ component of the proton wave function, leads to the prediction that the s-quark momentum distribution will be harder than the $\bar{s}$-quark distribution (Burkardt and Warr, 1992).

The CCFR collaboration has explored this possibility by performing an analysis (Bazarko *et al.*, 1995) in which the momentum distributions of the s and $\bar{s}$ quarks are allowed to be different. For this study the sea-quark distributions are parametrized by

$$x\bar{q}(x,\mu^2)=2\left[\frac{x\bar{u}(x,\mu^2)+x\bar{d}(x,\mu^2)}{2}\right]+\frac{xs(x,\mu^2)+x\bar{s}(x,\mu^2)}{2},$$

$$xs(x,\mu^2)=A_s(1-x)^{\alpha}\left[\frac{x\bar{u}(x,\mu^2)+x\bar{d}(x,\mu^2)}{2}\right],$$

$$x\bar{s}(x,\mu^2)=A_s'(1-x)^{\alpha'}\left[\frac{x\bar{u}(x,\mu^2)+x\bar{d}(x,\mu^2)}{2}\right]. \quad (66)$$

With the s and $\bar{s}$ distributions constrained to have the same number, $\int_0^1 s(x,\mu^2)dx=\int_0^1\bar{s}(x,\mu^2)dx$, A_s and A_s' are defined in terms of κ, α, and α'. In the CCFR analysis, four parameters, κ, α, $\Delta\alpha=\alpha-\alpha'$, and the charm quark mass m_c, are determined from the data with the charm hadron branching ratio fixed to the value obtained from other measurements, $B_c^{\mathrm{I}}=0.093\pm0.009$ (see Sec. IV.E.6). The results are

$$\kappa=0.536\pm0.030\pm0.037^{-0.064}_{+0.098},$$

$$\alpha=-0.78\pm0.40\pm0.75\pm0.98,$$

$$\Delta\alpha=-0.46\pm0.42\pm0.40\pm0.65,$$

$$m_c=1.66\pm0.16\pm0.07^{+0.04}_{-0.01}\ \mathrm{GeV/c^2}, \quad (67)$$

where the first error is statistical, the second is systematic, and the third is due to the uncertainty in B_c^{I}. The value of $\Delta\alpha=-0.46\pm0.87$ indicates that the momentum distributions of s and $\bar{s}$ are consistent, and the difference in the two distributions is limited to $-1.9<\Delta\alpha<1.0$ at the 90% confidence level. Brodsky and Ma (1996) have compared their intrinsic strangeness model to these CCFR fits. The simple application of the model in their paper uses a scaling of the d valence-quark distributions to do the QCD evolution of the intrinsic strange-quark sea. The results of the calculation, including a 30% extrinsic strange-quark component, are inconsistent with the CCFR analysis, as shown in Fig. 4 of the Brodsky and Ma (1996) paper. From the figure, the predicted ratio is $x\bar{s}(x)/xs(x)=1.7$ at $x=0.07$ and falls to 1 at $x=0.22$. This difference corresponds to a $\Delta\alpha\approx-3$, which is inconsistent with the CCFR limit.

The CCFR fits assume a simple power-law relation of the strange to nonstrange sea and may not have sufficient flexibility to encompass an intrinsic strange-quark contribution at high x. An additional high-x component would show up in the CCFR analysis as a modification of B_c (and $|V_{cd}|^2$) for the neutrino charm production and as an unexplained excess at high x for the antineutrino production. The agreement of the antineutrino data (Fig. 41) and the agreement of the fit $B_c=0.1091\pm0.0097$ with $B_c^{\mathrm{I}}=0.093\pm0.009$ (see Sec. IV.E.6) extracted from other measurements limits the size of any intrinsic contribution to below 20%. Further analyses will be needed to test the intrinsic strangeness models directly and precisely. Since the intrinsic component mainly contributes at large x, it is unlikely that an

$s/\bar{s}$ asymmetry could explain the discrepancy between the charged-lepton and neutrino measurements of F_2 in the small-x region.

6. Measurements of $|V_{cd}|$

If the CKM matrix elements are not assumed, then the CCFR next-to-leading-order results (Bazarko *et al.*, 1995) can be interpreted in terms of α, m_c, and the following products:

$$|V_{cd}|^2 B_c = (5.34 \pm 0.39 \pm 0.24^{+0.25}_{-0.51}) \times 10^{-3} \quad \text{(CCFR-NLO)},$$

$$\frac{\kappa}{\kappa+2}|V_{cs}|^2 B_c = (2.00 \pm 0.10 \pm 0.06^{+0.06}_{-0.14}) \times 10^{-2}, \tag{68}$$

where the first error is statistical, the second systematic, and third from the QCD scale uncertainty.

As shown in Table VI, there is little difference in the parameters if the analysis is performed to leading order or next-to-leading order. Accordingly, we may combine the CCFR result with the leading-order result from the CDHS collaboration (Abramowicz *et al.*, 1982),

$$|V_{cd}|^2 B_c = (4.1 \pm 0.7^{+0.19}_{-0.39}) \times 10^{-3} \quad \text{(CDHS-LO)},$$

where the first error is the total experimental error and the second is the QCD scale error, which is not given by the original analysis but assumed to be the same as in the CCFR measurement. Combining the two results, assuming that all of the experimental errors are uncorrelated, yields

$$|V_{cd}|^2 B_c = (5.02^{+0.50}_{-0.69}) \times 10^{-3} \quad \text{(CCFR/CDHS)}. \tag{69}$$

These combinations can be used to extract $|V_{cd}|^2$ and $\kappa|V_{cs}|^2$ when B_c is determined from other data. B_c is determined by combining the charmed-particle semileptonic branching ratios measured at e^+e^- colliders (Barnett *et al.*, 1996) with the neutrino production fractions measured by the Fermilab E531 neutrino-emulsion experiment (Ushida *et al.*, 1988). Using an $E_{\rm vis} > 30$ GeV cut, E531 determined the following production fractions: $52 \pm 6\%$ D^0, $42 \pm 6\%$ D^+, $1 \pm 2\%$ D_s^+, and $5 \pm 3\%$ Λ_c^+. In the E531 analysis, events that could not be unambiguously identified as D^+ or D_s^+ were all categorized as D^+ events. To remove this small bias, a reanalysis was performed that included updated values of the charmed-hadron lifetimes (Bolton, 1994; 1997). This reanalysis finds the following production fractions with an $E_{\rm vis} > 30$ GeV cut: $58 \pm 6\%$ D^0, $26 \pm 6\%$ D^+, $7 \pm 5\%$ D_s^+, and $7 \pm 4\%$ Λ_c^+. These production fractions are consistent with those measured by e^+e^- experiments (Bortoletto *et al.*, 1988). With these particle fractions, $B_c^{\rm I} = 0.093 \pm 0.009$ (Bolton, 1994, 1997) and when incorporated with the combined measurement of Eq. (69) gives the value of the CKM matrix element,

$$|V_{cd}| = 0.232^{+0.017}_{-0.019} \quad \text{(CCFR/CDHS)},$$

where the error indicates all sources of uncertainty including the μ^2 scale uncertainty. This value compares well with the Particle Data Group value, $|V_{cd}| = 0.221 \pm 0.003$, which is determined from measurements of the other matrix elements and the unitarity constraint on the CKM matrix assuming three generations. The errors on the direct $|V_{cd}|$ measurement from ν charm production are currently at the $\pm 9\%$ level, which precludes a precise test of the CKM unitarity.

The CKM parameter $|V_{cs}|$ requires an independent determination of the strange-sea fraction κ, which is currently unavailable. Using the value of $B_c^{\rm I}$ given above with the result of Eq. (68) and making the conservative assumption that $\kappa \leqslant 1$ implies that

$$|V_{cs}| > 0.74 \text{ at } 90\% \text{ C.L.} \quad \text{(CCFR)}.$$

In the future, κ could be determined from a measurement of the xF_3 difference between neutrinos and antineutrinos, $xF_3^{\nu}(x,Q^2) - xF_3^{\bar{\nu}}(x,Q^2) = 4x[s(x,Q^2) - c(x,Q^2)]$. It should be possible with this technique to measure κ to 20%, which would allow the quantity $|V_{cd}|/|V_{cs}|$ to be determined to 10% from the dimuon measurements.

F. Charm-sea measurements from wrong-sign single-muon production

Wrong-sign single-muon production can be used to probe the charm content in the nucleon through the neutral-current scattering of a ν_μ off a charm quark, which subsequently decays into a μ^+. A charm component is expected in QCD through gluon splitting into $c\bar{c}$ pairs. In a typical QCD calculation, the charm sea is set to zero for $Q^2 < Q_0^2 \approx 4\ \text{GeV}^2$ and is then allowed to evolve via the DGLAP equations. In the ν_μ interaction, neutral-current scattering off a charm quark is suppressed due to the kinematic effects related to producing two heavy-charm quarks ($c\bar{c}$) in the final state:

$$\nu_\mu + c(+\bar{c}) \rightarrow \nu_\mu + c(+\bar{c}) \hookrightarrow s + \mu^+ + \nu_\mu. \tag{70}$$

For a mean energy of 100 GeV, this suppression introduces a factor of ~ 0.3 relative to massless quark production. In addition, to go from the charm production rate to the wrong-sign single-muon rate, one must incorporate the semileptonic branching ratio for the final-state charmed particle ($\sim 10\%$) and the acceptance for the muon to be measured in the detector (typically $\sim 20\%$). The size of the cross section for neutral-current scattering off charm quarks in the nucleon can be estimated using the charm-sea calculations. Using the next-to-leading-order parton distributions of the CTEQ collaboration (Botts *et al.*, 1993), one finds that the cross section for neutral-current charm scattering is a factor of 0.005 lower than the total neutrino charged-current scattering cross section. Combining all these factors, one would expect a wrong-sign single-muon rate (that was approximately 3×10^{-5} of the normal charged-current rate.

The CCFR collaboration has made a study (Mishra *et al.*, 1989) of wrong-sign single-muon production using the data from their narrow-band E616/E701 experiment.

The dominant background comes from the $\bar{\nu}_\mu$ contamination in the beam. CCFR minimizes this background by requiring that the observed energy in the wrong-sign single-muon events have $E_{vis}>100$ GeV, which reduces the background rate to 2.3×10^{-4}. Other background sources (ν_e induced dilepton production, misidentified dimuon events, and neutral-current interactions with a π/K decay in the hadron shower) contribute an additional background at the 1.5×10^{-4} level. For $E_{\rm vis}>100$ GeV, the CCFR experiment observes 43.0 ± 6.6 wrong-sign single-muon events with a calculated background of 26.9 ± 5.1 events, leading to a 2σ excess of 16.1 ± 8.3 events or a rate of $(2.3\pm1.2)\times10^{-4}$. The CCFR collaboration presents the excess as a 90% confidence level upper limit on the wrong-sign single-muon rate of 4.3×10^{-4}, which is much larger than the estimate of 1.4×10^{-5} for neutral-current charm scattering with $E_{\rm vis}>100$ GeV.

V. ELECTROWEAK PHYSICS WITH NEUTRINO BEAMS

Lepton-scattering experiments permit the study of electroweak interactions at spacelike momentum transfers of $10^{-2}\leqslant Q^2\leqslant10^{+2}$ GeV^2 in a fixed-target environment, with $Q^2\rightarrow10^4$ GeV^2 possible in the future at the HERA ep collider. As such they complement the large $\sqrt{s}$ timelike measurements now performed with extraordinary precision at LEP, SLD, and the Tevatron. It is sometimes not appreciated that electroweak measurements performed in fixed-target lepton-scattering experiments can also still compete with the collider results in probing the standard model.

Neutrino scattering, in particular, has contributed to our understanding of electroweak physics over roughly four historical phases since the early 1970s: (I) confirmation of the existence of neutral currents through first observation of $\nu_\mu e^-\rightarrow\nu_\mu e^-$ at CERN (Hasert *et al.*, 1973); (II) early measurements of $\sin^2\theta_W$ that provided a critical ingredient to the successful prediction of the masses of the W and Z bosons (Arnison *et al.*, 1983); (III) second-generation weak-mixing angle determinations that probed one-loop corrections to the standard model and provided some of the first useful upper and lower limits on the top mass; and, finally, (IV) third-generation experiments that seek to test the internal consistency of electroweak theory through precise coupling-constant extrapolations that can be compared to other precision electroweak measurements at colliders. In this review we shall summarize the current experimental state of electroweak measurements with neutrino probes (period III), and give short- and intermediate-term prospects for current and future experiments (period IV). Detailed discussions of results obtained prior to direct observation of the W and Z may be obtained elsewhere (Kim *et al.*, 1981; Fogli, 1986). The remainder of this section is divided into three parts: theoretical motivation, experimental neutrino-electron scattering, and experimental neutrino-nucleon scattering.

A. Theoretical motivation

Neutrino-nucleon and neutrino-electron scattering depends on the left- and right-handed $\nu-Z^0$ and Z^0 target fermion couplings. Because all of the parameters of the standard model except the Higgs mass are now well known, the couplings measured in neutrino scattering are predicted to high accuracy. Any significant deviation between measurement and prediction would thus indicate new physics. Other experimental programs (LEP/SLD, LEP II, CDF/D0) also probe for new physics through precision electroweak tests, and neutrino experiments complement these high-energy efforts in several ways:

(i) By measuring different combinations of couplings than collider experiments, in particular, couplings to light quarks.
(ii) By measuring cross sections at moderate spacelike momentum transfer, as opposed to the large timelike scattering explored at colliders.
(iii) By extracting cross sections with ''orthogonal'' analysis tools: for example, different radiative correction packages and very limited quark-gluon fragmentation model dependence.

Electroweak measurements are frequently summarized by quoting a value of the weak mixing angle $\sin^2\theta_W$; however, this parameter can be defined in many different ways, e.g.,

$$1-M_W^2/M_Z^2\equiv\sin^2\theta_W(\text{on shell}) \tag{71}$$

and

$$A_{LR}(Z^0)\equiv\frac{[\frac{1}{2}-\sin^2\theta_W(\text{eff})]^2-\sin^4\theta_W(\text{eff})}{[\frac{1}{2}-\sin^2\theta_W(\text{eff})^2]+\sin^4\theta_W(\text{eff})}. \tag{72}$$

The ''on-shell'' mixing angle $\sin^2\theta_W$(on-shell) naturally emerges in describing direct W mass measurements and turns out to be very close to the mixing angle inferred from measurements of νN scattering. The parameter $\sin^2\theta_W$(eff) is an equally useful choice for parametrizing the left-right cross-section asymmetry for the e^+e^- annihilation at the Z^0 resonance. Many other choices are possible. A way to reduce confusion in comparing the sensitivity of different experiments to electroweak physics is to translate all measurements to an equivalent determination of a common physical parameter, for which a convenient choice is the W boson mass.[4] It follows simply that a ±0.002 on-shell mixing angle measurement in neutrino scattering (see Sec. V.A.4.a) is equivalent to a ±100-MeV W mass measurement, which compares well with expected results from LEP II and CDF/D0.

[4]These translations use standard model electroweak theory with the fine-structure constant α, the Fermi constant G_F, the Z^0 mass M_Z, and the top-quark mass M_{top}, as input. Low-energy electroweak observables can be calculated to sufficient accuracy without knowing the Higgs boson mass M_H.

TABLE VIII. Neutral-current standard model couplings for electron and quark targets.

f	ℓ_f	r_f
e^-	$-\frac{1}{2}+\sin^2\theta_W$	$\sin^2\theta_W$
u,c	$\frac{1}{2}-\frac{2}{3}\sin^2\theta_W$	$-\frac{2}{3}\sin^2\theta_W$
d,s	$-\frac{1}{2}+\frac{1}{3}\sin^2\theta_W$	$\frac{1}{3}\sin^2\theta_W$

1. Basic cross sections

Muon-neutrino scattering cross sections off light-fermion targets can be expressed in tree level as

$$\frac{d\sigma(\nu_\mu f\to\nu_\mu f)}{dy}=\frac{G_F^2 s}{\pi}[\ell_f^2+r_f^2(1-y)^2]\left(1+\frac{sy}{M_Z^2}\right)^{-2}, \tag{73}$$

$$\frac{d\sigma(\bar{\nu}_\mu f\to\bar{\nu}_\mu f)}{dy}=\frac{G_F^2 s}{\pi}[\ell_f^2(1-y)^2+r_f^2]\left(1+\frac{sy}{M_Z^2}\right)^{-2}, \tag{74}$$

where $f=e^-,u,d,s,c$; $G_F=(1.16639\pm0.00002)\times10^{-5}$ GeV^{-2} is the Fermi constant, $M_Z=91.187\pm0.007$ GeV is the Z^0 mass; s is the effective center-of-mass energy, which depends on f; y is the inelasticity; and ℓ_f,r_f are left- and right-handed coupling constants summarized in Table VIII. At fixed-target energies, the propagator term $(1+sy/M_Z^2)^{-2}$ seldom differs from unity by more than one percent for quark targets and is entirely negligible for electron targets. Although all experiments apply propagator corrections, this factor will be omitted for brevity in subsequent formulas.

Electron-neutrino-electron ($\nu_e e^-$ and $\bar{\nu}_e e^-$) scattering cross sections contain additional charged-current and interference terms. These processes have been observed (Reines *et al.*, 1976; Allen *et al.*, 1990, 1991, 1993; Krakauer *et al.*, 1990, 1992a, 1992b), and experimental results have provided important qualitative confirmation of the standard model, for example, the elimination of the fourfold sign ambiguity in axial and vector coupling constants of the electron. However, limited statistics preclude precision electroweak tests. Similar comments currently apply to very high Q^2 neutral-current scattering measurements at HERA (Derrick *et al.*, 1995, 1996b; Aid *et al.*, 1996a), although there is considerable hope in this case for future improvement (see, for example, Cashmore, Elsen, Kniehl, and Spiesberger, 1996). Accordingly, we shall restrict our discussion to scattering experiments that use ν_μ and $\bar{\nu}_\mu$ beams.

2. Neutrino-electron scattering

For electrons, $s_e=2m_eE_\nu$, with m_e the electron mass and E_ν the neutrino energy. The total neutral-current scattering cross sections then follow as

$$\frac{d\sigma(\nu_\mu e^-\to\nu_\mu e^-)}{dy}=\sigma_0^{\nu e}E_\nu[\ell_e^2+r_e^2(1-y)^2], \tag{75}$$

$$\frac{d\sigma(\bar{\nu}_\mu e^-\to\bar{\nu}_\mu e^-)}{dy}=\sigma_0^{\nu e}E_\nu[\ell_e^2(1-y)^2+r_e^2], \tag{76}$$

with $\sigma_0^{\nu e}=2G_F^2m_e/\pi=17.2\times10^{-42}$ cm^2/GeV. The electron mass sets the scale for the very small cross section and also drives the kinematics. With a maximum momentum transfer $Q^2_{\max}=2m_eE_\nu\simeq0.001E_\nu$ GeV^2, with E_ν in GeV, the electron always scatters nearly parallel to the neutrino beam.

The charged-current process $\nu_\mu e^-\to\nu_e\mu^-$, sometimes called inverse muon decay, represents an electroweak test in its own right. The tree-level cross section is

$$\frac{d\sigma(\nu_\mu e^-\to\nu_e\mu^-)}{dy}=\sigma_0^{\nu e}E_\nu\left(1-\frac{m_\mu^2}{2m_eE_\nu}\right)^2, \tag{77}$$

with the kinematic threshold occurring at $E_\nu\cong11$ GeV. The small center-of-mass energy forces the muon to be emitted in the forward direction.

Muon-decay measurements do not measure final-state neutrino helicities and thus cannot distinguish between vector left-handed couplings g^V_{LL} and scalar couplings g^S_{LL}; the inverse muon-decay cross section is proportional to $|g^V_{LL}|^2$ and thus resolves this ambiguity. Muon decay *and* inverse muon decay are required to establish rigorously the $V-A$ character of the charged current.

Electroweak radiative corrections to $\nu_\mu e^-$ and $\bar{\nu}_\mu e^-$ neutral-current (Novikov, Okun, and Vysotsky, 1993) and charged-current (Bardin and Dokuchaeva, 1987) scattering have been calculated. An apparently coincidental cancellation between the two dominant radiative corrections in neutral-current scattering causes the effective weak mixing angle $\sin^2\theta_W^{\nu e}$ to be very close to $\sin^2\theta_W$(eff) extracted from asymmetry measurements at LEP/SLD.

3. Neutrino-nucleon scattering

For quarks, the effective center-of-mass energy is $s_q=2ME_\nu\xi$, with M the nucleon mass and ξ interpretable as the fraction of the nucleon's four-momentum carried by the struck quark. An experiment can only measure, in practice, the average over ξ of the sum over all quark targets inside the nucleon (and, in fact, these distributions are further averaged over the incident-neutrino energy distribution):

$$\frac{d\sigma(\nu_\mu p\to\nu_\mu X)}{dy}=\frac{2G_F^2ME_\nu}{\pi}\times\int_0^1 d\xi\sum_{q=u,d,s,c}\{[\ell_f^2+r_f^2(1-y)^2]\times\xi q(\xi)+[\ell_f^2(1-y)^2+r_f^2]\xi\bar{q}(\xi)\}, \tag{78}$$

$$\frac{d\sigma(\bar{\nu}_\mu p\to\bar{\nu}_\mu X)}{dy}=\frac{2G_F^2ME_\nu}{\pi}\times\int_0^1 d\xi\sum_{q=u,d,s,c}\{[\ell_f^2(1-y)^2+r_f^2]\times\xi q(\xi)+[\ell_f^2+r_f^2(1-y)^2]\xi\bar{q}(\xi)\}. \tag{79}$$

Neutron cross sections follow from isospin arguments with the substitutions $u(\bar{u})\to d(\bar{d})$, $d(\bar{d})\to u(\bar{u})$, $s(\bar{s})\to s(\bar{s})$, and $c(\bar{c})\to c(\bar{c})$ (but see Sec. V.A.4.d). Contributions from b and t quarks are assumed to be negligible.

For isoscalar targets, omitting second-generation quark contributions for the moment,

$$\frac{d\sigma(\nu_\mu N\to\nu_\mu X)}{dy}=\frac{G_F^2 ME_\nu}{\pi}\times\int_0^1 d\xi\{[\ell_u^2+\ell_d^2+(r_u^2+r_d^2)(1-y)^2]\times[\xi u(\xi)+\xi d(\xi)]+[(\ell_u^2+\ell_d^2)(1-y)^2+r_u^2+r_d^2]\times[\xi\bar{u}(\xi)+\xi\bar{d}(\xi)]\}, \tag{80}$$

$$\frac{d\sigma(\bar{\nu}_\mu N\to\bar{\nu}_\mu X)}{dy}=\frac{G_F^2 ME_\nu}{\pi}\times\int_0^1 d\xi\{[(\ell_u^2+\ell_d^2)(1-y)^2+r_u^2+r_d^2]\times[\xi u(\xi)+\xi d(\xi)]+[\ell_u^2+\ell_d^2+(r_u^2+r_d^2)(1-y)^2][\xi\bar{u}(\xi)+\xi\bar{d}(\xi)]\}. \tag{81}$$

At this level, one notes that neutral-current cross sections can be reexpressed as

$$\frac{d\sigma(\nu_\mu N\to\nu_\mu X)}{dy}=(\ell_u^2+\ell_d^2)\frac{d\sigma(\nu_\mu N\to\mu^- X)}{dy}+(r_u^2+r_d^2)\frac{d\sigma(\bar{\nu}_\mu N\to\mu^+ X)}{dy}, \tag{82}$$

$$\frac{d\sigma(\bar{\nu}_\mu N\to\nu_\mu X)}{dy}=(r_u^2+r_d^2)\frac{d\sigma(\nu_\mu N\to\mu^- X)}{dy}+(\ell_u^2+\ell_d^2)\frac{d\sigma(\bar{\nu}_\mu N\to\mu^+ X)}{dy}, \tag{83}$$

a result that follows more generally from isospin conservation (Llewellyn Smith, 1983). When integrated over y, the above imply the Llewellyn-Smith relations,

$$R^\nu\equiv\frac{\int dy[d\sigma(\nu_\mu N\to\nu_\mu X)/dy]}{\int dy[d\sigma(\nu_\mu N\to\mu^- X)/dy]} \tag{84}$$

$$=(\ell_u^2+\ell_d^2)+r(r_u^2+r_d^2), \tag{85}$$

$$=\frac{1}{2}-\sin^2\theta_W+\frac{5}{9}(1+r)\sin^4\theta_W; \tag{86}$$

$$R^{\bar{\nu}}\equiv\frac{\int dy[d\sigma(\bar{\nu}_\mu N\to\bar{\nu}_\mu X)/dy]}{\int dy[d\sigma(\bar{\nu}_\mu N\to\mu^+ X)/dy]} \tag{87}$$

$$=(\ell_u^2+\ell_d^2)+r^{-1}(r_u^2+r_d^2), \tag{88}$$

$$=\frac{1}{2}-\sin^2\theta_W+\frac{5}{9}(1+r^{-1})\sin^4\theta_W; \tag{89}$$

with

$$r\equiv\frac{\int dy[d\sigma(\bar{\nu}_\mu N\to\mu^+ X)/dy]}{\int dy[d\sigma(\nu_\mu N\to\mu^- X)/dy]}, \tag{90}$$

the ν_μ to $\bar{\nu}_\mu$ charged-current ratio. Because the Llewellyn-Smith relationships also hold at the differential cross-section level, r can be defined to incorporate experimental hadron energy acceptance. For an ideal full acceptance experiment, $r\simeq 0.5$, whereas typical experimental cuts reduce this value to $r\simeq 0.35-0.45$. The Llewellyn-Smith formula is valid for an idealized isospin zero target composed only of first-generation quarks. Corrections must be applied in real experiments to take into account the effects of nonisoscalar targets and, especially, heavy quarks involved in the scattering.

A different combination of couplings can be isolated through a linear combination of R^ν and $R^{\bar{\nu}}$:

$$R^-=\frac{R^\nu-rR^{\bar{\nu}}}{1-r}, \tag{91}$$

$$=\frac{[d\sigma(\nu_\mu N\to\nu_\mu X)/dy]-[d\sigma(\bar{\nu}_\mu N\to\bar{\nu}_\mu X)/dy]}{[d\sigma(\nu_\mu N\to\mu^- X)/dy]-[d\sigma(\bar{\nu}_\mu N\to\mu^+ X)/dy]} \tag{92}$$

$$=\ell_u^2+\ell_d^2-r_u^2-r_d^2 \tag{93}$$

$$=\frac{1}{2}-\sin^2\theta_W. \tag{94}$$

This final line expresses the Paschos-Wolfenstein relationship (Paschos and Wolfenstein, 1973). It retains its accuracy even if heavy-quark contributions to the neutral-current and charged-current cross section are included, provided that these contributions are the same for ν_μ and $\bar{\nu}_\mu$. This latter feature makes this quantity superior to all other electroweak observables in the neutrino sector.[5]

4. Standard model corrections to $\nu_\mu(\bar{\nu}_\mu)N$ cross sections

Several corrections must be applied before standard model couplings can be extracted from the Llewellyn-Smith or Paschos-Wolfenstein relations or their variants.

[5]Direct implementation of the Paschos-Wolfenstein method requires knowledge of the relative $\bar{\nu}:\nu$ flux ratio to an accuracy that would be difficult to obtain in practice. This difficulty can be surmounted by analyzing the data in the form suggested by the first line of Eq. (91), in which all cross sections appear only in ratios. The relative flux error is then converted to an uncertainty in r, which is known to about 2%, a level that does not result in unacceptable systematic error. For more details, see Bolton (1995).

a. Standard model electroweak radiative corrections

Radiative corrections approximately factor into two parts: QED final-state radiation (De Rujula *et al.*, 1979), for which final-state muon bremsstrahlung diagrams are most important, and purely weak corrections, which effectively shift coupling constants (Marciano and Sirlin, 1980). A complete treatment that combines the two effects exists (Bardin and Fedorenko, 1979).

The effect of weak corrections can be represented schematically by the following:

$$\not{\ell}_f \rightarrow (1+\Delta\rho)\not{\ell}_f, \tag{95}$$

$$r_f \rightarrow (1+\Delta\rho) r_f, \tag{96}$$

$$\sin^2\theta_W \rightarrow (1+\Delta\kappa)\sin^2\theta_W . \tag{97}$$

Calculation of $\Delta\rho$ and $\Delta\kappa$ requires a precise definition of $\sin^2\theta_W$. While any definition is possible, it has become conventional to use the on-shell or Sirlin definition [Eq. (71)] to describe νN scattering. With this convention, the leading contributions to $\Delta\rho$ and $\Delta\kappa$ that arise from the large top mass,

$$\Delta\kappa = \frac{3G_F}{8\sqrt{2}\pi^2}\cot^2\theta_W M_{top}^2 + \mathcal{O}\ln\left(\frac{M_H^2}{M_W^2}\right) + \cdots, \tag{98}$$

$$\Delta\rho = \frac{3G_F}{8\sqrt{2}\pi^2} M_{top}^2 + \mathcal{O}\ln\left(\frac{M_H^2}{M_W^2}\right) \ldots, \tag{99}$$

largely cancel (Marciano and Sirlin, 1980; Stuart, 1987), and a $\sin^2\theta_W$ measurement from νN scattering can be thought of as an effective W-mass measurement,[6]

$$\sin^2\theta_W(\nu N) \simeq \sin^2\theta_W(\text{on-shell}). \tag{100}$$

Since the direct measurement of the top mass (Abachi *et al.*, 1995; Abe *et al.*, 1995b), the on-shell definition is less motivated, although it remains convenient so that the precision of neutrino measurements can be compared to that of colliders.

QED radiative corrections are numerically large and must be handled with care. Their dominant effect is to harden the observed y distributions for $\nu_\mu N$ and $\overline{\nu}_\mu N$ charged-current cross sections relative to their expected theoretical forms; good control of acceptance corrections minimizes their effect.

b. Structure functions and higher-order QCD corrections

The use of neutral-current to charged-current cross-section ratios coupled with the approximate validity of the Llewellyn-Smith and Paschos-Wolfenstein relations obviates the need to correct for light-quark structure-function effects. Similarly, uncertainties in $\alpha_S(Q^2)$ contribute negligible error in the extraction of electroweak parameters.

c. Heavy-quark production

The most uncertain parts of νN charged-current and neutral-current cross sections are due to scattering from and production of heavy flavor,

$$\nu_\mu s \rightarrow \nu_\mu s, \tag{101}$$

$$\nu_\mu c \rightarrow \nu_\mu c, \tag{102}$$

$$\nu_\mu d \rightarrow \mu^- c, \tag{103}$$

$$\nu_\mu s \rightarrow \mu^- c, \tag{104}$$

$$\nu_\mu s \rightarrow \mu^- u; \tag{105}$$

here s is counted as "heavy." The phenomenology and experimental status of neutrino-induced heavy-quark production is described in Sec. IV. For the purpose of neutral-current analyses, heavy-flavor production introduces uncertainties in electroweak analyses through two main effects:

(i) The neutral-current processes are not simply related to analogous charged-current cross sections through a Llewellyn-Smith–type formula, due to the role of the charm mass, CKM matrix elements, and large flavor asymmetry $[s(\xi) \neq c(\xi)]$.

(ii) The threshold behavior of charm production is not known well enough, independent of the model used to describe it. In the naive leading-order slow rescaling model, where the threshold dependence in charged-current charm production is described by a single effective charm mass m_c^{eff}, one only knows $m_c^{\text{eff}} = 1.31 \pm 0.24$ GeV (Rabinowitz *et al.*, 1993), an 18% error. Better models of charm production exist, but these do not improve the experimental uncertainty. Threshold effects in charm production persist to very high neutrino energies because of the important role of sea-quark mechanisms, which predominate at low ξ, where the effective center-of-mass-energy $2ME_\nu\xi$ is not necessarily large compared to $(m_c^{\text{eff}})^2$.

d. Isovector effects

Two kinds of isospin-violating effects are present; these can be thought of as nuclear and nucleon isospin-violating effects.

Heavy targets, such as iron, used in high-statistics scattering experiments have a small ($\sim 6\%$) neutron excess. This excess creates cross-section terms proportional to $u - \overline{u} - d + \overline{d} \equiv u_V - d_V$ and $\overline{u} - \overline{d}$, referred to as valence and sea contributions, respectively. The valence contribution has only directly been measured in relatively low-statistics νp and νD bubble-chamber experiments (Jones *et al.*, 1994); however, global fits (see, for

[6]Strictly speaking, this is true only if $\sin^2\theta_W$ is extracted using the Llewellyn-Smith formalism, and even then, only if experimental acceptance effects do not move the effective value of r too far from $r \simeq 0.4-0.5$. These restrictions have no consequence now that M_{top} corrections can be made.

example, Martin *et al.*, 1996; Lai *et al.*, 1997) to parton distributions that compare high-statistics νN charged-current scattering to ep, μp, eD, and μD electroproduction provide tight indirect constraints. The sea-quark contribution, now known not to vanish (Amaudruz *et al.*, 1992a), is not well constrained, but is numerically small.

Isospin violation exists even in an isoscalar target, because electromagnetic and quark mass effects break the equality between u(proton) and d(neutron) quark distributions. These effects produce corrections to $\sin^2\theta_W$ of ~ 0.002 (Sather, 1992).

e. Longitudinal cross section

The simple decomposition of νN cross sections into terms proportional to 1 and $(1-y)^2$ is broken by the existence of a nonzero longitudinal structure function $R_L(\xi,Q^2)$. As in the case of other higher-order QCD effects, the longitudinal structure function modifies the y distribution but not the Llewellyn Smith or Paschos-Wolfenstein relations. Influence on neutrino experiments arises only because the y distribution slightly affects charged-current/neutral-current separation experimentally. With sufficient care, acceptance corrections for $R_L(\xi,Q^2)$ can be applied with negligible uncertainty added to coupling extractions.

f. Higher-twist effects

Higher-twist contributions to neutrino cross sections fall as $1/Q^{2n}$, with $n \geqslant 1$. This kinematic dependence alone severely suppresses their effects on neutral-current analyses at high energies. Further suppression arises from the similarity of neutral-current to charged-current cross-section ratios from deep-inelastic and higher-twist sources, provided scattering occurs from an isoscalar target (a consequence of the Llewellyn Smith relation). For example, purely elastic scattering, the "highest twist" of all, has a neutral-current to charged-current cross-section ratio of ~ 0.35, as compared to the deep-inelastic scattering total of ~ 0.31.

In fact, higher-twist effects are arguably absent in any experiment that is in a regime where logarithmic QCD evolution of structure functions dominates ($Q^2 > 1-10$ GeV^2, depending on ξ). In order to exhibit this approximate scaling behavior, the cross section must consist of a very large number of high-twist terms; but, by duality arguments, many high-twist terms added together are equivalent to the simpler quark scattering picture.

Pumplin (1990) has argued to the contrary, based on an application of vector/axial-vector dominance. In his model, the $a_1-\rho$ mass difference generates substantial and uncertain violations of the Llewellyn Smith relationship (but not the Paschos-Wolfenstein relationship, since vector dominance produces equal ν_μ and $\overline{\nu}_\mu$ cross sections). However, his model fails to describe charged-current differential cross sections unless its parameters are constrained to the level where effects on the neutral-current to charged-current cross-section ratios are small.[7] Furthermore, from the arguments above, it may simply be incorrect to decompose an inclusive cross section displaying approximate scaling into a deep-inelastic scattering contribution and a single higher-twist term. More theoretical study of this issue would be useful.

5. New physics effects in $\nu_\mu(\overline{\nu}_\mu)e^-$ and $\nu_\mu(\overline{\nu}_\mu)N$ cross sections

Direct effects of physics beyond the standard model can appear in $\nu_\mu(\overline{\nu}_\mu)N$ scattering through higher-order loop corrections (standard model and non-standard model Higgs, fourth-generation quarks), new propagator effects (heavy Z^0, leptoquarks, compositeness), and lepton mixing (mirror fermions, Langacker, Luo, and Mann, 1992). Somewhat surprisingly, the advantage enjoyed by neutrino measurements in probing certain classes of new physics derives often from the low energy scale of the process. For example, an unmixed new Z' would produce linear shifts in couplings in $\nu_\mu N$ neutral-current scattering, since both the Z^0 and Z' are far off-shell. In contrast, the effect of a heavy, unmixed Z' in e^+e^- scattering on the Z^0 pole would be to produce quadratic shifts in observed coupling, since the Z' would not interfere directly with the Z^0 at the pole. An advantage is also enjoyed over direct searches at the Tevatron, which have excellent sensitivity to constructive interference between Z^0 and Z', which increases lepton pair cross sections over expectations, but relatively poor sensitivity to destructive interference, which has the opposite effect.

Other new physics not directly related to neutral-current processes can manifest itself through shifts in the apparent values of $R^\nu, R^{\overline{\nu}}$ measured by experiment. For example, $\nu_\mu \rightarrow \nu_e, \nu_\tau$ oscillations would increase the value of $R^\nu, R^{\overline{\nu}}$ relative to standard model expectations because both ν_e and ν_τ charged-current interactions produce an experimental ν_μ neutral-current signature (McFarland *et al.*, 1995).

B. $\nu_\mu e^-$ and $\bar{\nu}_\mu e^-$ scattering: experiment

The experimental challenge in measuring neutral-current processes is to separate genuine scattering from electrons from much-larger-cross-section elastic and quasielastic $\nu_e N$ and $\overline{\nu}_e N$ reactions,

$$\nu_e N \rightarrow e^-(n\pi^0)X, \tag{106}$$

where X consists of hadrons with energy too low to be measured; furthermore, from the rare, but kinematically similar, coherent pion production reactions:

$$\nu_\mu N \rightarrow \nu_\mu \pi^0 N. \tag{107}$$

[7]Specifically, we have compared Pumplin's model to high-precision charged-lepton scattering and have concluded, conservatively, that his parameter S_0 is constrained to $S_0 < 2$ GeV^2 at 90% confidence level. Pumplin's original analysis allowed $S_0 \rightarrow \infty$.

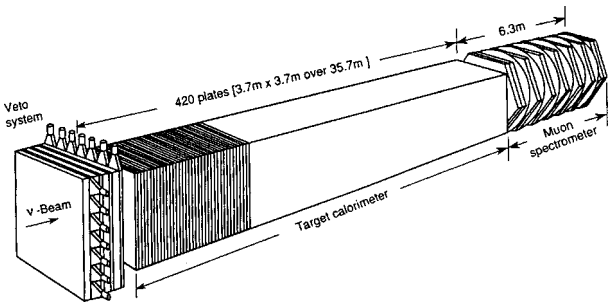

FIG. 45. The CHARM II detector.

Background rejection arises primarily from application of cuts that exploit the small momentum transfer inherent in scattering from electron targets. This demands good electron energy and angle measurement, which in turn mandates fine-grained low-Z detectors. Since measurement of electron charge is not possible in a practical device, separate, high-purity, sign-selected beams are required. Corrections must be applied for the wrong-sign neutrino content and for the few percent component of ν_e or $\overline{\nu}_e$ in the beam.

Charged-current scattering is also optimally performed in a low-Z, fine-grained detector. This allows superior rejection of the primary background, $y \to 0$ inclusive $\nu_\mu N$ scattering. At high energies, inverse muon decay can also be observed in dense detectors as the quasielastic processes become proportionally less important and the final-state muon is easily observed. The low y $\nu_\mu N$ background processes can be measured from inclusive $\overline{\nu}_\mu N$ scattering under the assumption that $d\sigma(\nu_\mu N \to \mu^- X)/dy = d\sigma(\overline{\nu}_\mu N \to \mu^+ X)/dy$ as $y \to 0$.

1. Neutral-current scattering

CHARM II (Vilain *et al.*, 1994a) recorded 2677 ± 82 $\nu_\mu e^-$ and 2752 ± 88 $\overline{\nu}_\mu e^-$ events, after corrections, using a 690-ton instrumented glass detector (Geiregat *et al.*, 1993; Fig. 45) in a 2.1×10^{19} proton-on-target exposure to the 450-GeV CERN horn beam. The detector has excellent electron identification and measurement capabilities (Fig. 46). Average energies for ν_μ and $\overline{\nu}_\mu$ were 23.7 and 19.2 GeV, respectively. Backgrounds, mainly from coherent π^0 production in elastic nuclear and nucleon scattering and quasielastic $\nu_e N$ scattering, were at the 50% level. The CHARM II statistics ensure that this experiment dominates previous efforts at Brookhaven (Ahrens *et al.*, 1983; Ahrens *et al.*, 1985; Abe *et al.*, 1986); hence this section is essentially a resumé of their results.

CHARM II published their final results in terms of vector and axial-vector couplings, $g_V^{\nu e}$ and $g_A^{\nu e}$, which are simply related to left- and right-handed electron couplings, assuming the neutrino is purely left-handed, by $\ell_e = \frac{1}{2}(g_V^{\nu e} + g_A^{\nu e})$, $r_e = \frac{1}{2}(g_V^{\nu e} - g_A^{\nu e})$. The results are

$$g_V^{\nu e} = -0.035 \pm 0.012 \pm 0.012 \quad \text{(CHARM II)},$$

$$g_A^{\nu e} = -0.503 \pm 0.006 \pm 0.016 \quad \text{(CHARM II)},$$

where the first uncertainty listed is the statistical error and the second is the systematic error. These measurements were then combined to yield an effective weak mixing angle for νe scattering, $\sin^2\theta_W^{\nu e}$, which, as noted earlier, is fortuitously close, theoretically, to the effective mixing angle measured at LEP and SLD:

$$\sin^2\theta_W^{\nu e} = 0.2324 \pm 0.0058 \pm 0.0059 \quad \text{(CHARM II)},$$

with the first error statistical and the second systematic. These results, based on an analysis of the absolute differential cross sections, were confirmed with an earlier study based only on the shape of the y distributions (Vilain *et al.*, 1993; Fig. 47). Excellent agreement with LEP/SLD results exists.

The CHARM II data also provided, after combination with LEP data and lower-energy $\nu_e e^-$ scattering, an elegant demonstration of the flavor independence of the Z^0 coupling to neutrinos (Vilain *et al.*, 1994b).

Finally, the comparison of CHARM II coupling measurements to standard model electroweak theory allowed limits to be set on masses of new heavy Z' bosons. For the optimal case of no mixing with the ordinary Z^0 boson, the following limits hold (Vilain *et al.*, 1994c):

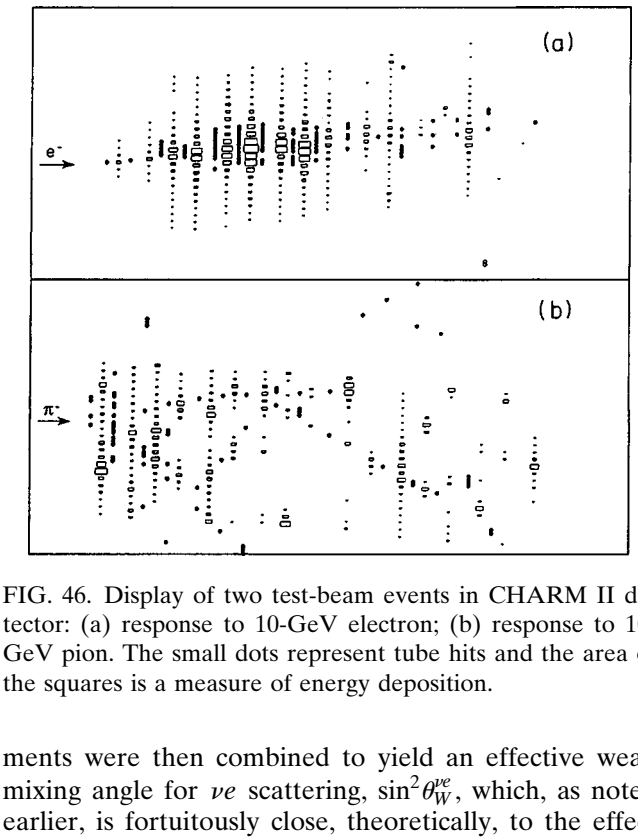

FIG. 46. Display of two test-beam events in CHARM II detector: (a) response to 10-GeV electron; (b) response to 10-GeV pion. The small dots represent tube hits and the area of the squares is a measure of energy deposition.

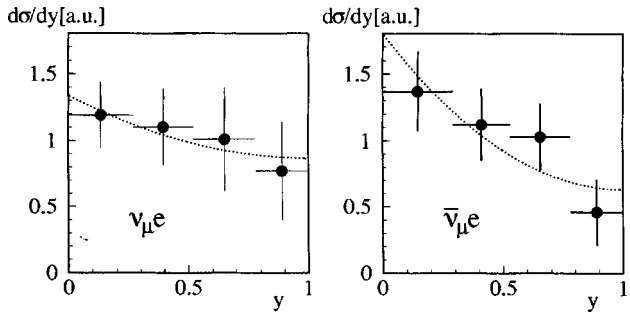

FIG. 47. Neutral-current ν_μ and $\overline{\nu}_\mu$ differential cross-section shapes measured by CHARM II. Arbitrary units.

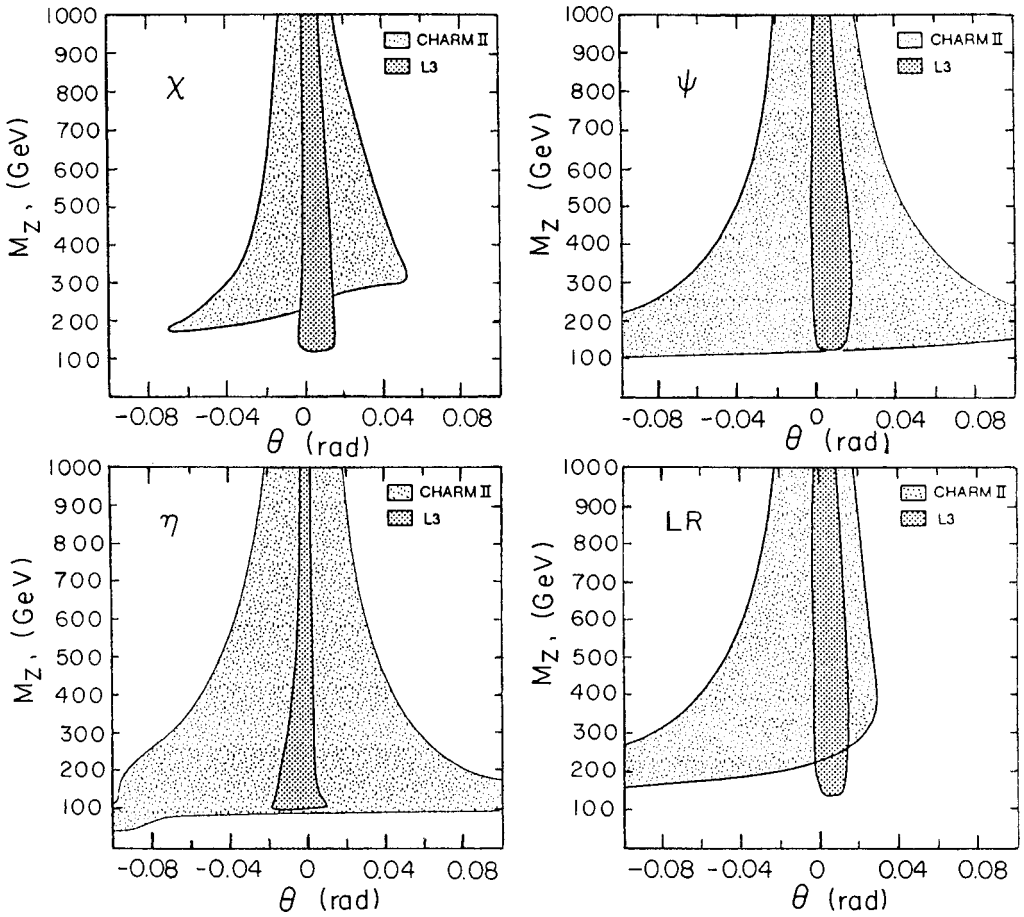

FIG. 48. Limits of Z' set by CHARM II from a comparison of electron couplings with the standard model predictions.

$M_{Z(\chi)}>262$ GeV at 95% C.L. (CHARM II),

$M_{Z(\psi)}>135$ GeV at 95% C.L. (CHARM II),

$M_{Z(\eta)}>100$ GeV at 95% C.L. (CHARM II),

$M_{Z(LR)}>253$ GeV at 95% C.L. (CHARM II).

More general limits are summarized in Fig. 48. While these results have largely been superseded by direct searches and other precision measurements, it is nonetheless remarkable that such constraints follow from the modest statistics and low energy scale of CHARM II.

2. Inverse muon decay

CCFR (FNAL E744/770; Mishra *et al.*, 1990) has a sample of 3248 ± 148 corrected events from an exposure corresponding to 3×10^6 ordinary charged-current events at an average energy $E_\nu=160$ GeV. CHARM II (Geiregat *et al.*, 1990; Vilain *et al.*, 1996) recorded a signal of $15\,758\pm324$ events from a much larger exposure (13.3×10^6 charged-current events) at an average energy $E_\nu=23$ GeV. Signal-to-background for this reaction was approximately 1:2.5 for both experiments. Figure 49 shows the background-subtracted transverse-momentum spectrum from CHARM II.

The $E_\nu\to\infty$ asymptotic cross-section slopes [Eq. (77)] $\sigma_0^{\nu e}$ measured by the two experiments agree, and the total measurement errors are comparable. CCFR's error is dominated by statistics, whereas CHARM II, with their lower energy beam, is more affected by model uncertainties in making the background subtraction. The quoted cross section results,

$$\sigma_0^{\nu e}=(16.93\pm0.85\pm0.52)\times10^{-42}\ \text{cm}^2 \quad \text{(CCFR)},$$

$$\sigma_0^{\nu e}=(16.01\pm0.33\pm0.83)\times10^{-42}\ \text{cm}^2 \quad \text{(CHARM II)},$$

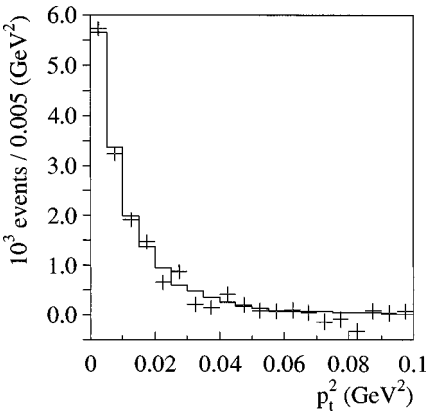

FIG. 49. Distribution of inverse muon-decay events as a function of p_t^2 from CHARM II. The solid line represents the expected distribution as simulated by a Monte Carlo calculation.

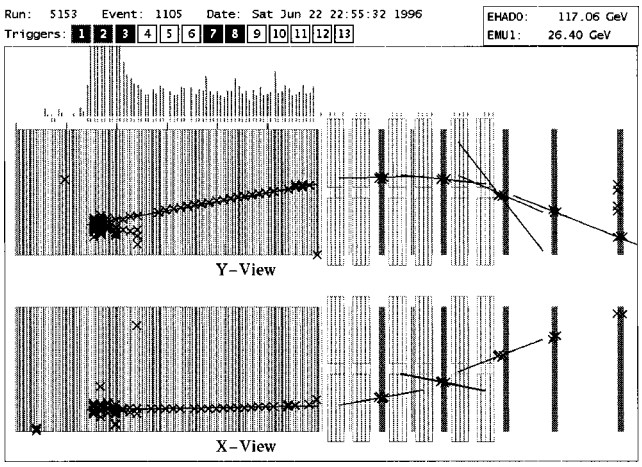

FIG. 50. A charged-current event candidate in the CCFR detector.

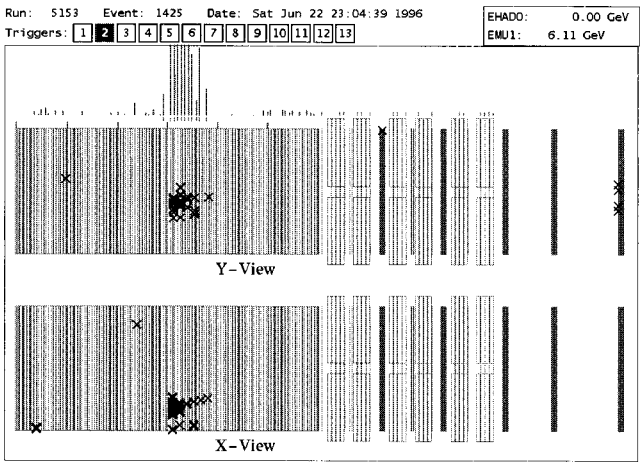

FIG. 51. A neutral-current event candidate in the CCFR detector.

also agree with the standard model prediction $\sigma_0^{\nu e} = 17.2 \times 10^{-42}$ cm^2.

Consistency with the standard model allows the two groups to set limits in the scalar coupling of

$$|g_{LL}^S|^2 < 0.30 \text{ at } 90\% \text{ C.L.} \quad \text{(CCFR)},$$

$$|g_{LL}^S|^2 < 0.475 \text{ at } 90\% \text{ C.L.} \quad \text{(CHARM II)};$$

and CHARM II also quotes

$$|g_{LL}^V|^2 > 0.881 \text{ at } 90\% \text{ C.L.} \quad \text{(CHARM II)}.$$

These results confirm the $V-A$ character of the charged-current interaction.

It should be noted that CHARM II applied standard model radiative corrections before setting their limits, whereas CCFR apparently did not. The effect of the radiative correction was to increase $\sigma_0^{\nu e}$ by $\sim 3\%$. Because the radiative corrections would (fortuitously) move the CCFR measurement closer to the standard model, actual limits on scalar couplings are probably tighter.

C. $\nu_\mu N$ and $\bar{\nu}_\mu N$ scattering: experiment

1. Method

The critical issue in neutrino-nucleon neutral-current to charged-current ratio measurements is the experimental separation between neutral-current and charged-current events. This separation essentially depends on the presence or absence of a muon in a particular event, as can be seen in Figs. 50 and 51, which show charged-current and neutral-current candidate events in the CCFR detector.

Two approaches have been successfully employed in high-statistics measurements: event-by-event charged-current identification through muon track finding [CHARM (Allaby *et al.*, 1986; Allaby *et al.*, 1987)] and statistical separation based on the distribution of longitudinal energy deposition in $\nu_\mu N$ interactions [CDHS (Abramowicz *et al.*, 1986; Blondel *et al.*, 1990; CCFR (Arroyo *et al.*, 1994)]. Figure 52 illustrates the latter idea as implemented by CCFR in the form of an event length distribution. The essential idea is that charged-current events produce penetrating muons that deposit energy over a large distance in the detector, whereas neutral-current event lengths are characteristic of a hadron shower. CDHS employed a variant of this technique, which allowed the separation length to vary with energy (Fig. 53). Corrections must be made for the fraction of short events which are actually charged current, typically 5–20 %, and for the much smaller "punch-through" of neutral-current events into the long-event-length category.

The second most important experimental effect is the correction for ν_e and $\overline{\nu_e}$ in the beam. Both neutral-

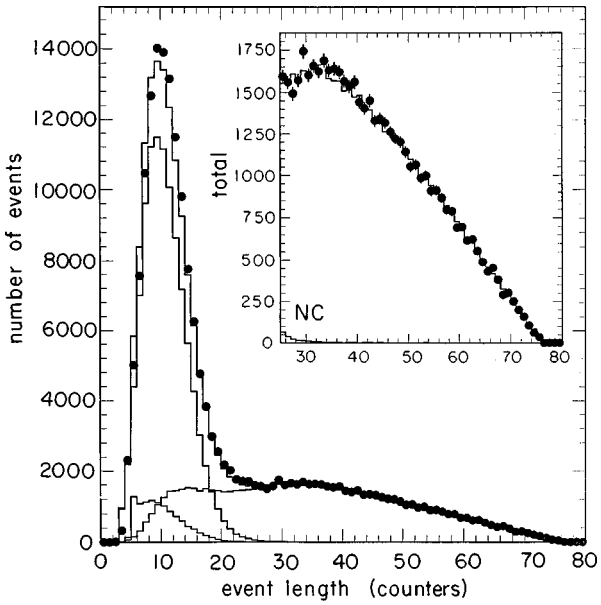

FIG. 52. Event length distribution for CCFR neutral-current analysis. Length is measured in units of scintillation counters exhibiting energy deposition in the event, with one counter corresponding to approximately 10 cm of steel. The large peak at short event lengths consists mainly of ν_μ neutral-current interactions, with a background of ν_e neutral-current and charged-current interactions and high y ν_μ charged-current interactions.

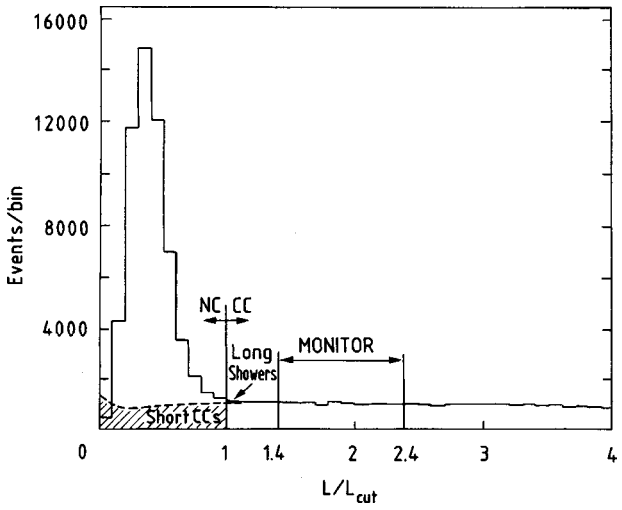

FIG. 53. Scaled event length distribution for CDHS neutral-current analysis. The shape of the plot is similar to that of CCFR, but the length separation is made energy dependent. MONITOR refers to the sample of (mainly) charged-current events with similar lengths to the neutral-current events that are used for neutral-current/charged-current normalization.

current and charged-current electron-neutrino interactions mimic the experimental signature of neutral-current ν_μ interactions, and their contribution to the apparent neutral-current sample must therefore be subtracted. The subtraction is estimated by a detailed Monte Carlo simulation of the neutrino beam. This simulation can be tuned to describe $\nu_e, \overline{\nu_e}$ produced from charged-kaon decay with high accuracy, since the $K^\pm$ decay contribution is tightly constrained by measurements of the $\nu_\mu, \overline{\nu_\mu}$ flux (Sec. II). The largest uncertainty in the calculated electron-neutrino flux comes from other sources of ν_e, such as beam scraping or K_L^0 decay. CCFR has recently directly measured the ν_e flux in their experiment using the difference in longitudinal energy deposition between electrons and hadrons (Romosan *et al.*, 1997); the result confirms the calculated flux used in electroweak measurements.

CHARM and CDHS attempted to extract values for R^ν and $R^{\overline{\nu}}$ and then infer $\sin^2\theta_W$, whereas CCFR varied the mixing angle in a parametric Monte Carlo approach to describe the data. Table IX compares properties of CCFR and CDHS/CHARM.[8] We focus on these three experiments in this section because other recent measurements (Bogert *et al.*, 1985; Reutens *et al.*, 1990) suffer from relatively poor statistical and systematic errors.

2. Standard model results

The most accurate determination of $\sin^2\theta_W$ from νN scattering is the recently updated final CCFR result (McFarland *et al.*, 1997):

[8]The latter pair ran in the same beam.

TABLE IX. Comparison of properties of CCFR and CDHS/CHARM experiments.

Property	CDHS/CHARM	CCFR
Mean neutrino energy	70 GeV	160 GeV
Minimum hadron energy	10 GeV	30 GeV
Mean Q^2	15 GeV^2	35 GeV^2
Statistics	2.0×10^5	8.1×10^5

$$\sin^2\theta_W(\text{on-shell}) = 0.2236 \pm 0.0027_{\text{expt.}} \pm 0.0030_{\text{model}} \quad (\text{CCFR}),$$

where the first error is the total statistical and systematic experimental contribution and the second represents uncertainties due to model corrections. This value was extracted from the ratio of neutral-current to charged-current events assuming values of $m_c^{\text{eff}}=1.31$ GeV, $M_{\text{top}}=175$ GeV, and $M_H=150$ GeV; the explicit dependence on these parameters is

$$\sin^2\theta_W(\text{on shell}) = 0.2236 + 0.0111(m_c^{\text{eff}} - 1.31\ \text{GeV}) + (2.1\times10^{-5})(M_{\text{top}} - 175\ \text{GeV}) - 0.0002\ \ln\left(\frac{M_H}{150\ \text{GeV}}\right) \quad (\text{CCFR}),$$

where the masses are in units of GeV. The significant dependence of the result on the effective charm quark mass and the weak dependence on radiative corrections in translating to the on-shell mixing angle are evident. A detailed breakdown of systematic errors is provided in Table X. The dominant contributions are from statistics, uncertainties in ν_e production (mainly from neutral-kaon sources), and charm quark production.

CDHS and CHARM extracted their values for the weak mixing angle from the Llewellyn-Smith formula. CDHS (Blondel *et al.*, 1990) obtained, using $m_c^{\text{eff}}=1.50$ GeV, $M_{top}=60$ GeV, and $M_H=100$ GeV,

$$\sin^2\theta_W(\text{on shell}) = 0.228 \pm 0.005_{\text{expt}} \pm 0.005_{\text{model}} \quad (\text{CDHS}),$$

and CHARM (Allaby *et al.*, 1987) reports a very similar result,

$$\sin^2\theta_W(\text{on shell}) = 0.236 \pm 0.005_{\text{expt}} \pm 0.005_{\text{model}} \quad (\text{CHARM}).$$

Unfortunately these results were published at a time when the top mass was thought to be lighter; hence one must undo some of the radiative corrections to compare to the more recent CCFR result. If a common set of model parameters is employed, CCFR, CDHS, and CHARM agree in detail (Bolton, 1995), with the charm production uncertainty dominating in all cases. The average value of $\sin^2\theta_W$ obtained is

$$\sin^2\theta_W(\text{on shell}) = 0.2256 \pm 0.0035 \quad (\text{average } \nu N).$$

This value is obtained by fitting the CHARM, CDHS, and CCFR mixing angles and the CDHS and CCFR charm mass measurements to a simple model that allows $\sin^2\theta_W$ and m_c^{eff} to vary. The fit has a χ^2 of 2.9 for 3

TABLE X. Uncertainties from updated CCFR extraction of $\sin^2\theta_W$.

SOURCE OF UNCERTAINTY	$\delta \sin^2\theta_W$
Data statistics	*0.0019*
Monte Carlo statistics	0.0004
Total statistics	0.0019
Charm production ($m_c = 1.31 \pm 0.24$ GeV)	*0.0027*
Charm sea	0.0006
Longitudinal cross section	0.0008
Higher twist	0.0010
Non-isoscalar target	0.0004
Strange sea	0.0003
Structure functions	0.0002
Radiative corrections	0.0001
Total physics model	0.0030
ν_e flux	*0.0015*
Transverse vertex	0.0004
Energy measurement	
Muon energy loss in shower	0.0003
Muon energy scale ($\pm 1\%$)	0.0004
Hadron energy scale ($\pm 1\%$)	0.0004
Event length	
Hadron shower length	0.0007
Vertex determination	0.0003
Detector noise, efficiency	0.0006
Dimuon production	0.0003
TOTAL EXPERIMENTAL	0.0027
TOTAL UNCERTAINTY	0.0041

degrees of freedom and also yields an estimate of $m_c^{\rm eff} = 1.37 \pm 0.19$ GeV. The contribution to the $\sin^2\theta_W$ error from charm production is ± 0.0023.

Within the standard model, the νN $\sin^2\theta_W$ measurement implies

$$M_W = 80.25 \pm 0.18 \ \text{GeV} \quad (\text{average } \nu N).$$

The latter agrees well with direct determinations at the Tevatron and LEP II. The most recent high-accuracy measurements are those of Abe *et al.*, 1995a; Abachi *et al.*, 1996 and Ackerstaff *et al.*, 1996, $M_W = 80.33 \pm 0.15$ GeV, and the indirect determination from global fits to e^+e^- data at the Z^0 (see, for example, Renton, 1995), $M_W = 80.359 \pm 0.056$ GeV.[9]

3. Model-independent results

The three collaborations have also attempted to present their results in a more model-independent form, and we summarize these results here. Where possible, the explicit dependence of a parameter on the effective charm quark mass $m_c^{\rm eff}$ is given, since correcting for charged-current charm production produces the largest systematic uncertainty in all results. In these cases, the charm mass contribution to the parameter is not included in the quoted error, but it can be easily calculated from $m_c^{\rm eff} = 1.5 \pm 0.3$ GeV used by CHARM/CDHS and $m_c^{\rm eff} = 1.31 \pm 0.24$ GeV used by CCFR.

CHARM and CDHS quote values of R^ν and $R^{\bar\nu}$, as well as separate extractions of $\Delta\rho$ and $\sin^2\theta_W$. CHARM obtains

$$R^\nu = 0.3093 \pm 0.0031 \quad (\text{CHARM}),$$

$$R^{\bar\nu} = 0.390 \pm 0.014 \quad (\text{CHARM}),$$

using $r = 0.456 \pm 0.011$ (CHARM), whereas CDHS extracts

$$R^\nu = 0.3135 \pm 0.0033 \quad (\text{CDHS}),$$

$$R^{\bar\nu} = 0.376 \pm 0.0016 \quad (\text{CDHS}),$$

using $r = 0.409 \pm 0.014$(CDHS). These cross-section ratios represent the most model-independent expression of νN electroweak results; only corrections for experimental effects and the nonisoscalar nuclear targets are applied. As such, they cannot be directly used for electroweak tests without further model corrections. CDHS has applied these corrections to get

$$R^{\nu 0} = 0.3122 \pm 0.0034_{\rm expt} - 0.009(m_c^{\rm eff} - 1.5 \ \text{GeV}) \quad (\text{CDHS}),$$

$$R^{\bar\nu 0} = 0.378 \pm 0.014_{\rm expt} - 0.019(m_c^{\rm eff} - 1.5 \ \text{GeV}) \quad (\text{CDHS}).$$

The 0 superscript denotes that these quantities have effects due to heavy quarks, radiative corrections, and other factors removed from the physical cross-section ratios. Application of these corrections requires slightly different ν_μ to $\bar\nu_\mu$ charged-current ratios to be used in the Llewellyn Smith formulas, $r^0 = 0.383 \pm 0.014_{\rm expt} + 0.004(m_c^{\rm eff} - 1.5 \ \text{GeV})$ for neutrinos and $\bar r^0 = 0.371 \pm 0.014_{\rm expt} + 0.004(m_c^{\rm eff} - 1.5 \ \text{GeV})$ for antineutrinos.

Because CDHS and CHARM took data in sign-selected beams, they could extract two electroweak parameters from their data without assuming the standard model. Translated to the notation of Eqs. (98) and (99), CDHS extracted values for these parameters (originally expressed as ρ and $\sin^2\theta_W$), using only their own data, of

$$\Delta\rho = 0.009 \pm 0.020_{\rm expt} - 0.023(m_c^{\rm eff} - 1.5 \ \text{GeV}) \quad (\text{CDHS}),$$

$$(1 + \Delta\kappa \sin^2\theta_W) = 0.218 \pm 0.021_{\rm expt} - 0.011(m_c^{\rm eff} - 1.5 \ \text{GeV}) \quad (\text{CDHS}).$$

The larger experimental error on the mixing angle simply reflects the weaker constraints of a two-parameter fit. The strong top-mass dependence of $\Delta\rho$ and $\Delta\kappa$ in the standard model allowed this measurement to be used to constrain $M_t < 200$ GeV well before the direct observation of the top quark. CDHS and CHARM weak-mixing-angle measurements also decisively ruled out the

[9] For a more detailed summary, see Barnett *et al.* (1996).

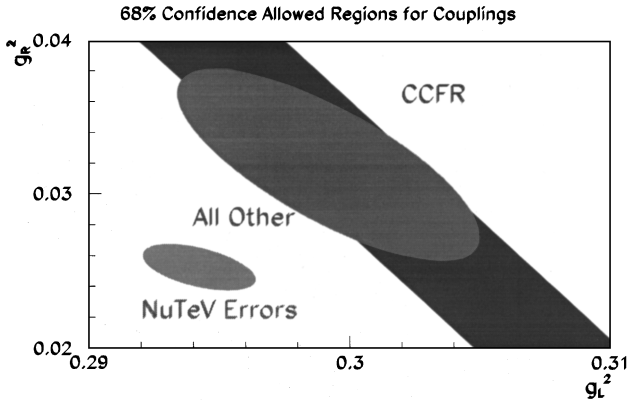

FIG. 54. Constraints on $g_L^2=\ell_u^2+\ell_d^2$ and $g_R^2=r_u^2+r_d^2$ from CCFR model-independent result and all neutrino data combined. Also shown are the projected constraints on these couplings from the NuTeV experiment.

once-promising grand unified theory based on minimal SU(5) (which predicted $\sin^2\theta_W=0.218\pm0.004$), corroborating results from proton-decay experiments (Marciano and Sirlin, 1980).

CCFR quoted an experimental value (McFarland *et al.*, 1997) for a sum of couplings that is closest to what it actually measured in its mixed $\nu_\mu/\overline{\nu}_\mu$ beam:

$$\begin{aligned}\hat{\kappa}\equiv&1.7897(\ell_u^2+\ell_d^2)+1.1479(r_u^2+r_d^2)\\&-0.0916(\ell_u^2-\ell_d^2)-0.0782(r_u^2-r_d^2),\\=&0.5820\pm0.0031\\&-0.0111(m_c^{\rm eff}-1.31\ \text{GeV})\quad(\text{CCFR}).\end{aligned}\tag{108}$$

This value can be used to constrain values of left- and right-handed couplings to quarks as shown in Fig. 54. Using this measurement and the standard model prediction of $\hat{\kappa}_{\rm SM}=0.5817\pm0.0013$, with standard model parameters fixed from other precision electroweak measurements of M_Z, M_W, and $M_{\rm top}$, CCFR set limits on some new physics processes:

(i) For "left-left" four-fermion contact operators described by a Lagrangian $-\mathcal{L}=\pm(4\pi/\Lambda_{LL}^{\pm})\overline{l}_L\gamma^\nu l_L\overline{q}_L\gamma_\nu q_L$,

$$\Lambda_{LL}^{+}>4.7\ \text{TeV at 95\% C.L.},$$

$$\Lambda_{LL}^{-}>5.1\ \text{TeV at 95\% C.L.}$$

The approximate equality of these limits reflects the equal sensitivity to destructive and constructive interference effects in νN scattering mentioned earlier and compares favorably with results set by CDF (Bodek, 1997). Limits on a set of other composite operators are also set.

(ii) For SU(5) leptoquarks that do not induce flavor-changing neutral currents and that have dominant left-handed couplings,

$$M_{LQ}|\eta_L|^{-1}>0.8\ \text{TeV at 95\% C.L.}$$

where M_{LQ} is the leptoquark mass and η_L the left-handed coupling parameter.

The CCFR result can be input into the formalism of (Langacker, Luo, and Mann (1992) to obtain parametric limits on a variety of new physics models. These results are summarized in Table XI.[10]

VI. SUMMARY AND OUTLOOK

High-energy, high-precision neutrino measurements have become an important tool for measuring the parameters of the standard model and for testing our understanding of the electroweak and strong interactions. This review has presented the current status of these measurements and has pointed out some of the open Uquestions. These topics are summarized below along with comments on future measurements, now underway or being planned, which will have even higher precision and be able to address some of these questions.

A. Structure functions and QCD tests

Precision neutrino experiments have made important contributions to our knowledge of nucleon structure and the strong interaction through the measurements of the structure functions F_2 and xF_3. Data have been taken over a wide range of targets and energies. The total neutrino cross section divided by energy has been found to be constant with energy, regardless of target. The structure-function measurements have different assumptions concerning R_L and radiative corrections, and are made on different types of target nuclei, making cross-experiment comparisons difficult. Iron data between CCFR and CDHSW can be directly compared, and a discrepancy exists, particularly in the low-x region and as a function of Q^2.

Neutrino-scattering studies yield important determinations of the parton distribution functions. These results are important inputs to the global fits due to the unique flavor differentiation of the neutrino measurements combined with the good precision. The xF_3 structure function is particularly important due to its close connection to the valence-quark distribution.

The recent neutrino measurements have comparable statistics to the charged-lepton structure-function measurements. Comparisons of the neutrino F_2 measurements to charged-lepton experiments allows an important test of the universality of the parton distributions measured in different processes. The comparison indicates general agreement over most of the kinematic region but a small discrepancy at low x after quark charge

[10]The values in Table XI are inferred from the CCFR measurement by the authors of this review; the experiment may publish more extended results that differ slightly from those presented here.

TABLE XI. Summary of limits on parameters for models of new physics beyond the standard model as described by Langacker *et al.* (1992) based on CCFR preliminary model-independent result.

Model	95% C.L.	Comment
$M_{Z(\chi)}$, $C=\sqrt{\frac{2}{5}}$	$M_{Z'}>691$ GeV	$Z(\chi)$ with $(g_2'/g_2)^2=\frac{5}{3}\sin^2\theta_W$
$M_{Z(\chi)}$, $C=0$	$M_{Z'}>215$ GeV	$Z(\chi)$ with $(g_2'/g_2)^2=\frac{5}{3}\sin^2\theta_W$
$M_{Z(\psi)}$, $C=\sqrt{\frac{2}{3}}$	$M_{Z'}>843$ GeV	$Z(\psi)$ with $(g_2'/g_2)^2=\frac{5}{3}\sin^2\theta_W$
$M_{Z(\psi)}$, $C=-\sqrt{\frac{2}{3}}$	$M_{Z'}>513$ GeV	$Z(\psi)$ with $(g_2'/g_2)^2=\frac{5}{3}\sin^2\theta_W$
$M_{Z(\psi)}$, $C=0$	$M_{Z'}>54$ GeV	$Z(\psi)$ with $(g_2'/g_2)^2=\frac{5}{3}\sin^2\theta_W$
$M_{Z(\eta)}$, $C=-\sqrt{\frac{1}{15}}$	$M_{Z'}>101$ GeV	$Z(\eta)$ with $(g_2'/g_2)^2=\frac{5}{3}\sin^2\theta_W$
$M_{Z(\eta)}$, $C=\sqrt{\frac{16}{15}}$	$M_{Z'}>879$ GeV	$Z(\eta)$ with $(g_2'/g_2)^2=\frac{5}{3}\sin^2\theta_W$
$M_{Z(\eta)}$, $C=0$	$M_{Z'}>87$ GeV	$Z(\eta)$ with $(g_2'/g_2)^2=\frac{5}{3}\sin^2\theta_W$
$M_{Z(3R)}$, $C=\sqrt{\frac{3}{5}}\alpha$	$M_{Z'}>988$ GeV	$Z(3R)$ with $(g_2'/g_2)^2=\frac{5}{3}\sin^2\theta_W$
$M_{Z(3R)}$, $C=-\sqrt{\frac{3}{5}}\alpha$	$M_{Z'}>189$ GeV	$Z(3R)$ with $(g_2'/g_2)^2=\frac{5}{3}\sin^2\theta_W$
$M_{Z(3R)}$, $C=0$	$M_{Z'}>244$ GeV	$Z(3R)$ with $(g_2'/g_2)^2=\frac{5}{3}\sin^2\theta_W$
Non-SM Higgs	$\Delta\rho<0.0049$	radiative correction parameter
SU(5) Leptoquark	$\lvert M_{LQ}/\eta_L\rvert>887$ GeV	RH coupling $\eta_R\simeq 0$
extra u_L fermion	$\sin^2\theta_L^u<0.011$	mixing with ordinary u_L
extra u_R fermion	$\sin^2\theta_R^u<0.037$	mixing with ordinary u_R
extra d_L fermion	$\sin^2\theta_L^d<0.009$	mixing with ordinary d_L
extra d_R fermion	$\sin^2\theta_R^d<0.074$	mixing with ordinary d_R
extra e_L fermion	$\sin^2\theta_L^e<0.043$	mixing with ordinary e_L
extra ν_{eL} fermion	$\sin^2\theta_L^{\nu_e}<0.043$	mixing with ordinary ν_{eL}
extra μ_L fermion	$\sin^2\theta_L^{\mu}<0.006$	mixing with ordinary μ_L
extra $\nu_{\mu L}$ fermion	$\sin^2\theta_L^{\nu_\mu}<0.043$	mixing with ordinary $\nu_{\mu L}$
4-Fermi plus	$\Lambda_+>4.1$ TeV	compositeness scale
4-Fermi minus	$\Lambda_-<4.0$ TeV	compositeness scale

and nuclear corrections are applied. At present, this difference is not understood. The discrepancy may be related to assumptions concerning nuclear corrections or to systematic errors in one or more of the experiments at low x. The difference is too large to be explained by uncertainties in the strange sea, which has been measured from neutrino charm production.

Precise tests of QCD are now possible with neutrino-scattering data. The CCFR E744/E770 data are the most precise, and the Q^2 evolution of the structure functions yields $\Lambda_{\overline{\rm MS}}^{\rm NLO-4}{}^f=337\pm 31(\exp)$ MeV, equivalent to $\alpha_s(M_Z^2)=0.119\pm 0.002(\exp)\pm 0.004(\text{scale})$. This is the most precise measurement of α_s at low and moderate Q^2 values. The agreement of the CCFR data with the QCD expectation is quite good. The Gross-Llewellyn–Smith sum-rule results have sufficient accuracy to test the predicted QCD corrections. Evaluation of this sum rule yields another measurement of the strong-coupling constant which is consistent with the CCFR α_s result from QCD evolution. Because of the inclusive nature of the Gross-Llewellyn–Smith and evolution measurements, these results have small theoretical errors and have been important in the past in establishing the QCD theory and more recently in making precise measurements of the fundamental parameters.

The NuTeV experiment (Bolton *et al.*, 1990) at Fermilab, which uses the upgraded CCFR detector and a new sign-selected beam (Bernstein *et al.*, 1994), began taking data in May 1996. This experiment will address many of the issues concerning structure functions raised in this review. Among the NuTeV goals are more precise measurements of α_s and R_L. In order to investigate fully the discrepancy in the F_2 measurements, more data in the low-x region are required, with improved systematic understanding. The NuTeV experiment is expected to obtain approximately equal statistical errors on F_2 with substantially reduced systematics. The most important systematic uncertainties are related to the absolute energy calibration of the detector. For the NuTeV experiment, precise hadron and muon energy calibrations will be obtained over a wide range of energies, using precision test-beam measurements throughout the run. With these improvements, the experiment should be able to measure the QCD scale parameter Λ to better than 25 MeV and improve significantly the uncertainties in the F_2 structure-function measurements at low x.

B. Measurements of the strange sea, charm sea, and $|V_{cd}|$

Neutrino charm production has been used to isolate the nucleon strange-quark distributions, $xs(x)$ and $x\bar{s}(x)$, and study the transition to the heavy charm quark. The CCFR next-to-leading-order analysis agrees

well with their dimuon data over a broad range of energies, with a charm quark mass $m_c = 1.70 \pm 0.19$ GeV. At next-to-leading order, the strange-quark distribution is found to have the same shape as the nonstrange sea but with a magnitude that is $(48 \pm 5)\%$ of an SU(3) symmetric sea. These measurements imply that an increased strange sea cannot be the explanation for the discrepancy between the neutrino and charged-lepton measurements of F_2 at low x. Investigations by the CCFR collaboration also indicate that the $s(x)$ and $\bar{s}(x)$ distributions are similar, as expected from a perturbative QCD source but inconsistent with nonperturbative models of intrinsic strangeness in the nucleon.

The CKM matrix elements $|V_{cd}|$ and $|V_{cs}|$ are determined from the neutrino dimuon data using an effective charm semileptonic branching ratio found from ν-emulsion and e^+e^- data. The combined CCFR/CDHS data yield a value of $|V_{cd}| = 0.232^{+0.017}_{-0.019}$, which is in excellent agreement with the value of $|V_{cd}| = 0.221 \pm 0.003$ found from other measurements combined with the unitarity of the CKM matrix. With the assumption that the strange sea must be smaller than the nonstrange sea ($\kappa \leq 1$), $|V_{cs}|$ is limited by the dimuon data to be >0.74 at 90% C.L. The parameter κ could possibly be determined in the future from a measurement of $xF_3^{\nu}(x,Q^2) - xF_3^{\bar{\nu}}(x,Q^2) = 4x[s(x,Q^2) - c(x,Q^2)]$. A 20% measurement of κ will provide a 10% measurement of $|V_{cd}|/|V_{cs}|$.

Present and future high-energy neutrino experiments should be able to improve these measurements significantly. The NuTeV experiment at Fermilab is running with a sign-selected beam that will eliminate the $\nu/\bar{\nu}$ confusion in the dimuon channel at low x with statistics similar to the CCFR (E744/770) sample. NOMAD (Astier *et al.*, 1991) and CHORUS (Armenise *et al.*, 1990; DeJong *et al.*, 1993) at CERN are presently running with a high-energy, horn-focused beam searching for neutrino oscillations. These experiments will also record a sizable number of charm production events (about 20 000 dileptons for NOMAD and 20 000 reconstructed charm particles for CHORUS.) As in the E531 experiment, CHORUS will be able to reconstruct exclusive channels, allowing precise tests of the theory. The ultimate neutrino charm production experiment is COSMOS (E803 at Fermilab; Kodama *et al.*, 1993). Like CHORUS, the experiment is a hybrid emulsion experiment that can reconstruct exclusive charm final states. The estimated data sample is 200 000 reconstructed charm events, which might allow a determination of $|V_{cd}|$ to $\sim 2\%$ (Bolton, 1997, 1994).

Wrong-sign single-muon production has also been used to probe the charm content in the nucleon through the neutral-current scattering of a ν_μ off a charm quark, which subsequently decays into a μ^+. From their wrong-sign single-muon data with $E_{vis} > 100$ GeV, the CCFR collaboration has set a 90% confidence level upper limit on the wrong-sign single-muon rate of 4.3×10^{-4}, which is much larger than the estimate of 1.4×10^{-5} for neutral-current charm scattering.

The currently running NuTeV experiment will have a substantially reduced $\bar{\nu}_\mu$ contamination in their new SSQT beam, which corresponds to a 2×10^{-5} wrong-sign single-muon rate for $E_{vis} > 100$ GeV. If additional cuts can be used to minimize the other backgrounds, the NuTeV experiment may be able to isolate a neutral-current charm scattering signal and make the first direct estimate of the charm sea in the nucleon.

C. Electroweak measurements with neutrinos

Experimental results on ν_μ scattering on electrons and nucleons confirm predictions of the standard model at low to moderate spacelike momentum transfer and, in some cases, provides interesting limits on possible new physics beyond the standard model.

CHARM II and earlier experiments have demonstrated from neutral-current measurements with electron targets that Z^0 couplings to neutrinos are independent of family number and that the Z^0 couples to electrons in processes with very small spacelike momentum transfer with precisely the strength specified by the standard model and precision measurements at very-high-energy collider experiments. CCFR and CHARM II measurements of charged-current scattering of neutrinos from electrons demonstrate conclusively that the charged-current process is uniquely V-A and set tight constraints on possible exotic couplings beyond the standard model.

Precision neutral-current measurements with nucleon targets by CDHS, CHARM, and CCFR allow an independent and competitive ($\Delta M_W = \pm 180$ MeV) prediction of the W boson mass within the standard model in a very different kinematic regime than direct and indirect collider determinations. The consistency of neutrino measurements with standard model predictions allows limits to be placed on a variety of possible new physics parameters, especially those involving light quarks.

The only way to probe for the expected new physics beyond the standard model is currently through precision electroweak tests, and this situation will likely persist at least until the LHC turns on and begins taking data. Because effects of new physics at low energies will be small and subtle, if they are there at all, it is desirable to perform as many cross checks as possible. Neutrino-nucleon scattering experiments are perhaps the only noncollider measurements that have the required sensitivity to provide these checks. And indeed, there are prospects for further gains from two near-term efforts that should improve electroweak measurements in the neutrino sector.

The NuTeV experiment is currently taking data with high-intensity sign-selected beams that will permit the first significant exploitation of the Paschos-Wolfenstein relationship, which will reduce the error due to heavy-flavor production by a factor of 4–5. The new beam design also eliminates much of the uncertainty attributed to K_L^0 production of ν_e. Depending on the total number of protons ultimately delivered, NuTeV should measure

$\sin^2\theta_W$ with an error of $0.002-0.003$, which is equivalent to a W mass measurement of 100–150 MeV.

High-sensitivity searches for $\nu_\mu \to \nu_\tau$ oscillations are now underway with CHORUS and NOMAD at CERN, soon to be joined by COSMOS and MINOS (Ables *et al.*, 1995) at Fermilab. While these experiments probably will not directly measure electroweak parameters to interesting precision, they should greatly improve our understanding of neutrino-induced charm production. It is possible that the error on the effective charm mass will be reduced by an order of magnitude or more, particularly by CHORUS and COSMOS, which will have unique abilities to measure inclusive charm production in their emulsion targets. With the largest systematic uncertainty in $\nu_\mu N$ perhaps nearly eliminated, one might envision a successor to the NuTeV experiment running at Fermilab with the higher intensity of the Fermilab Main Injector, or possibly even a new neutrino experiment at LHC or a muon collider.

ACKNOWLEDGMENTS

The authors wish to thank the members of the CCFR and NuTeV Collaborations for many valuable discussions and for making their results available for this review. This work was supported by the Department of Energy contract DE-FG02-94ER40814 and the National Science Foundation grant PHY-95-12810.

APPENDIX: COLLABORATIONS AND RESEARCH FACILITIES

15-ft BC	Fifteen Foot Bubble Chamber Collaboration at Fermilab
BCDMS	Bologna-CERN-Dubna-Munich-Saclay
BEBC	Big European Bubble Chamber
CCFR	Columbia-Chicago-Fermilab-Rochester
CDF	Collider Detector at Fermilab
CDHS	CERN-Dortmund-Heidelberg-Saclay
CDHSW	CERN-Dortmund-Heidelberg-Saclay-Warsaw
CERN	European Laboratory for Particle Physics
CESR	Cornell Electron Storage Ring accelerator
CHARM	CERN-Hamburg-Amsterdam-Rome-Moscow
CHARM II	Upgraded CHARM Experiment
CHORUS	CERN Hybrid Oscillation Research apparatUS
CLEO	Collider Detector at CESR
COSMOS	COsmologically Significant Mass Oscillation Search
CTEQ	Project on Collaborative Theoretical and Experimental Studies of QCD
D0	D0 Collider Detector at Fermilab
EMC	European Muon Collaboration
Gargamelle	CERN Liquid Freon Bubble Chamber
GRV	M. Gluck, E. Reya, and A. Vogt
H1	H1 Collider Detector at HERA
HERA	Hadron Electron Ring Accelerator
HPWF	Harvard-Pennsylvania-Wisconsin-Fermilab
LEP	Large Electron Positron collider
LHC	Large Hadron Collider
MINOS	Main Injector Neutrino Oscillation Search
MRS	A. D. Martin, R. G. Roberts and W. J. Stirling
NMC	New Muon Collaboration
NOMAD	Neutrino Oscillation MAgnetic Detector
NuTeV	Neutrino Experiment at the Fermlab Tevatron
OPAL	Omni-Purpose Apparatus at LEP
PDFLIB	Parton Distribution Functions Library Database
PDG	Particle Data Group
SLAC	Stanford Linear Accelerator Center
SLD	SLAC Linear-Collider Detector
SPS	Super Proton Synchrotron
UA1	CERN SppS Collider Detector
WHPFOR	Wisconsin-Pennsylvania-Fermilab-Harvard-Ohio State-Rutgers
ZEUS	ZEUS Collider Detector at HERA

REFERENCES

Abachi, S., *et al.* (D0 Collaboration), 1995, Phys. Rev. Lett. **74**, 2632.
Abachi, S., *et al.* (D0 Collaboration), 1996, Phys. Rev. Lett. **77**, 3309.
Abe, K., *et al.* (CDF Collaboration), 1986, Phys. Rev. Lett. **56**, 1107.
Abe, F., *et al.* (CDF Collaboration), 1994, Phys. Rev. Lett. **73**, 225.
Abe, F., *et al.* (CDF Collaboration), 1995a, Phys. Rev. D **52**, 4784.
Abe, F., *et al.* (CDF Collaboration), 1995b, Phys. Rev. Lett. **75**, 1397.
Ables, E., *et al.* (MINOS Collaboration), 1995, "A Long Baseline Neutrino Oscillation Experiment at Fermilab," Fermilab-Proposal P-875.
Abromowicz, H., *et al.* (CDHS Collaboration), 1981, Nucl. Instrum. Methods **180**, 429.
Abramowicz, H., *et al.* (CDHS Collaboration), 1982, Z. Phys. C **15**, 19.
Abramowicz, H., *et al.* (CDHS Collaboration), 1983, Z. Phys. C **17**, 237.
Abramowicz, H., *et al.* (CDHS Collaboration), 1984, Z. Phys. C **25**, 29.
Abramowicz, H., *et al.* (CDHS Collaboration), 1986, Phys. Rev. Lett. **57**, 298.
Ackerstaff, K., *et al.* (OPAL Collaboration), 1996, CERN Preprint CERN-PPE/96-141.
Adams, M., *et al.*, 1995, Z. Phys. C **67**, 403.
Adams, M., *et al.*, 1996, Z. Phys. C **71**, 391.
Aderholz, M., *et al.*, 1986, Phys. Lett. B **173**, 211.
Ahrens, L. A., *et al.*, 1983, Phys. Rev. Lett. **51**, 1514.
Ahrens, L. A., *et al.*, 1985, Phys. Rev. Lett. **54**, 18.
Aid, S., *et al.*, 1995, Nucl. Phys. B **449**, 3.
Aid, S., *et al.* (H1 Collaboration), 1996a, Phys. Lett. B **379**, 319.
Aid, S., *et al.* (H1 Collaboration), 1996b, Nucl. Phys. B **470**, 3.
Aivazis, M. A. G., J. C. Collins, F. I. Olness, and W.-K. Tung, 1994, Phys. Rev. D **50**, 3102.
Aivazis, M. A. G., F. I. Olness, and W.-K. Tung, 1990, Phys. Rev. Lett. **65**, 2339.

Aivazis, M. A. G., F. I. Olness, and W.-K. Tung, 1994, Phys. Rev. D **50**, 3085.
Akulinichev, S. V., *et al.*, 1985, Phys. Rev. Lett. **55**, 2239.
Allaby, J. V., *et al.* (CHARM Collaboration), 1986, Phys. Lett. B **177**, 446.
Allaby, J. V., *et al.* (CHARM Collaboration), 1987, Z. Phys. C **36**, 611.
Allaby, J. V., *et al.* (CHARM Collaboration), 1988, Z. Phys. C **38**, 403.
Allasia, D., *et al.*, 1985, Z. Phys. C **28**, 321.
Allasia, D., *et al.*, 1990, Phys. Lett. B **249**, 366.
Allen, R. C., *et al.*, 1990, Phys. Rev. Lett. **64**, 1330.
Allen, R. C., *et al.*, 1991, Phys. Rev. D **43**, R1.
Allen, R. C., *et al.*, 1993, Phys. Rev. D **47**, 11.
Allport, P. P., *et al.*, 1989, Phys. Lett. B **232**, 417.
Altarelli, G., and G. Martinelli, 1978, Phys. Lett. B **76**, 89.
Altarelli, G., and G. Parisi, 1977, Nucl. Phys. B **126**, 298.
Amaudruz, P., *et al.* (New Muon Collaboration), 1992a, Nucl. Phys. B **371**, 3.
Amaudruz, P., *et al.* (New Muon Collaboration), 1992b, Phys. Lett. B **295**, 159.
Amaudruz, P., *et al.* (New Muon Collaboration), 1995, Nucl. Phys. B **441**, 3.
Anjos, J. C., *et al.* (E691 Collaboration), 1990, Phys. Rev. Lett. **65**, 2503.
Armenise, N., *et al.* (CHORUS Collaboration), 1990, "A New Search for $\nu_\mu \rightarrow \nu_\tau$ Oscillations," CERN-SPSC/90-42.
Armenise, N., *et al.* (CHORUS Collaboration), 1993, "A New Search for $\nu_\mu \rightarrow \nu_\tau$ Oscillations," CERN–PPE/93.
Arnison, G., *et al.* (UA1 Collaboration), 1983, Phys. Lett. B **122**, 103.
Arnold, R. G., *et al.* (SLAC E87 Collaboration), 1984, Phys. Rev. Lett. **52**, 727.
Arroyo, C., *et al.* (CCFR Collaboration), 1994, Phys. Rev. Lett. **72**, 3452.
Astier, P., *et al.* (NOMAD Collaboration), 1991, "Search for the Oscillation $\nu_\mu \rightarrow \nu_\tau$," CERN-SPSLC/91-21.
Aubert, J. J., *et al.* (European Muon Collaboration), 1987, Nucl. Phys. B **293**, 740.
Auchincloss, P., *et al.* (CCFR Collaboration), 1990, Z. Phys. C **48**, 411.
Baker, N. J., *et al.*, 1983, Phys. Rev. Lett. **51**, 735.
Baker, N. J., *et al.*, 1991, Phys. Rev. D **43**, 2765.
Bardin, D. Yu., and V. A. Dokuchaeva, 1986, JINR-ER-86-260.
Bardin, D. Yu., and V. A. Dokuchaeva, 1987, Nucl. Phys. B **287**, 839.
Bardin, D. Yu., and O. M. Fedorenko, 1979, Sov. J. Nucl. Phys. **30**, 418.
Barish, B. C., 1978, Phys. Rep. **39**, 279.
Barnett, R. M., 1976, Phys. Rev. Lett. **36**, 1163.
Barnett, R. M., *et al.* (Particle Data Group), 1996, Phys. Rev. D **54**, 1.
Barone, V., *et al.*, 1994, Phys. Lett. B **328**, 143.
Baruzzi, V., *et al.*, 1983, Nucl. Instrum. Methods **207**, 339.
Bauer, T. H., R. D. Spital, D. R. Yennie, and F. M. Pipkin, 1978, Rev. Mod. Phys. **50**, 261.
Bazarko, A. O., *et al.* (CCFR Collaboration), 1995, Z. Phys. C **65**, 189.
Benvenuti, A., *et al.* (HPWF Collaboration), 1975, Phys. Rev. Lett. **34**, 419.
Benvenuti, A. C., *et al.*, 1987, Phys. Lett. B **195**, 91.
Benvenuti, A. C., *et al.*, 1990, Phys. Lett. B **237**, 592.
Berge, J. P., *et al.* (CDHS Collaboration), 1987, Z. Phys. C **35**, 443.
Berge, J. P., *et al.* (CDHS Collaboration), 1991, Z. Phys. C **49**, 187.
Bergsma, F., *et al.* (CHARM Collaboration), 1983, Phys. Lett. B **123**, 269 [Note: A correction factor of 1. 14 should be applied to F_2 and xF_3 to take into account new results on σ_T as described in Allaby *et al.* (1988)].
Bergsma, F., *et al.* (CHARM Collaboration), 1984, Phys. Lett. B **141**, 129.
Bernstein, R., *et al.* (NuTeV Collaboration), 1994, Fermilab-TM-1884.
Blondel, A., *et al.* (CDHS Collaboration), 1990, Z. Phys. C **45**, 361.
Bodek, A., and J. L. Ritchie, 1981a, Phys. Rev. D **23**, 1070.
Bodek, A., and J. L. Ritchie, 1981b, Phys. Rev. D **24**, 1400.
Bodek, A. (CDF Collaboration), 1997, in *Proceedings of the 28th International Conference on High Energy Physics (ICHEP96)*, Warsaw, Poland, 1996 (World Scientific, Singapore), p. 1438.
Bogert, D., *et al.* (FMMF Collaboration), 1985, Phys. Rev. Lett. **55**, 1969.
Bolton, T., 1994, in *Proceedings of the Charm-2000 Workshop* at Fermilab, 1994 (Fermilab, Batavia, IL), p. 267.
Bolton, T., 1995, in *Radiative Corrections: Status and Outlook*, edited by B. F. L. Ward (World Scientific, Singapore), p. 330.
Bolton, T., 1997, "Determining the CKM Parameters V_{cd} from νN Charm Production," KSU-HEP-97-04, e-print hep-ex/9708014.
Bolton, T., *et al.* (NuTeV Collaboration), 1990, "Precision Measurements of Neutrino Neutral Current Interactions Using a Sign Selected Beam," Fermilab Proposal P-815.
Bortoletto, D., *et al.* (CLEO Collaboration), 1988, Phys. Rev. D **37**, 1719.
Bosetti, P. C., *et al.*, 1982, Phys. Lett. B **110**, 167.
Botts, J., *et al.* (CTEQ Collaboration), 1993, Phys. Lett. B **304**, 159.
Braun, V. M., and A. V. Kolesnichenko, 1987, Nucl. Phys. B **283**, 723.
Brodsky, S. J., and B. Ma, 1996, Phys. Lett. B **381**, 317.
Brodsky, S. J., C. Peterson, and N. Sakai, 1981, Phys. Rev. D **23**, 2745.
Buras, A. J., and K. J. F. Gaemers, 1978, Nucl. Phys. B **132**, 259.
Burkardt, M., and B. J. Warr, 1992, Phys. Rev. D **45**, 958.
Callan, Jr., C. G., and D. J. Gross, 1969, Phys. Rev. Lett. **22**, 156.
Cashmore, R. J., E. Elsen, B. A. Kniehl, and H. Spiesberger, 1996, "Electroweak Physics at HERA: Introduction and Summary," preprint MPI/PhT/96-105 (hep-ph/9610251).
Close, F. E., R. G. Roberts, and G. G. Ross, 1983, Phys. Lett. B **129**, 346.
Collins, P., and T. Spiller, 1985, J. Phys. G **11**, 1289.
Cooper, A. M., *et al.*, 1984, Phys. Lett. B **141**, 133.
Dasgupta, M., and B. R. Webber, 1996, Phys. Lett. B **484**, 273.
Dasu, S., *et al.*, 1988a, Phys. Rev. Lett. **60**, 2591.
Dasu, S., *et al.*, 1988b, Phys. Rev. Lett. **61**, 1061.
DeJong, M., *et al.* (CHORUS Collaboration), 1993, "A New Search for $\nu_\mu \rightarrow \nu_\tau$ Oscillations," CERN-PPE/93.
Derrick, M., *et al.* (ZEUS Collaboration), 1995, Phys. Rev. Lett. **75**, 1006.
Derrick, M., *et al.* (ZEUS Collaboration), 1996a, Z. Phys. C **69**, 607.

Derrick, M., *et al.* (ZEUS Collaboration), 1996b, Z. Phys. C **72**, 47.
De Rujula, A. R. Petronzio, and A. Savoy-Navarro, 1979, Nucl. Phys. B **154**, 393.
Devoto, A., *et al.*, 1983, Phys. Rev. D **27**, 508.
Diemoz, M., F. Ferroni, and E. Longo, 1986, Phys. Rep. **130**, 293.
Dokshitser, Yu. L., D. I. Diakonov, and S. I. Troian, 1978, Phys. Lett. B **78**, 290.
Dokshitser, Yu. L., *et al.*, 1980, Phys. Rep. **58**, 269.
Duke, D., and J. Owens, 1984, Phys. Rev. D **30**, 49.
Dunne, G. V., and A. W. Thomas, 1986, Nucl. Phys. A **455**, 701.
Fisk, H. E., and F. Sciulli, 1982, Annu. Rev. Nucl. Part. Sci. **32**, 499.
Fogli, G. L., 1986, Riv. Nuovo Cimento **9**, 1.
Furmanski, W., and R. Petronzio, 1982, Nucl. Phys. B **195**, 237.
Geesaman, D. F., K. Saito, and A. W. Thomas, 1995, Annu. Rev. Nucl. Part. Sci. **45**, 337.
Geiregat, D., *et al.* (CHARM II Collaboration), 1990, Phys. Lett. B **247**, 131.
Geiregat, D., *et al.* (CHARM II Collaboration), 1993, Nucl. Instrum. Methods **325**, 91.
Georgi, H., and H. D. Politzer, 1976, Phys. Rev. D **14**, 1829.
Glück, M., S. Kretzer, and E. Reya, 1996, Phys. Lett. B **380**, 171.
Glück, M., E. Reya, and A. Vogt, 1992, Z. Phys. C **53**, 127.
Glück, M., E. Reya, and A. Vogt, 1995, Z. Phys. C **67**, 433.
Gomez, J., *et al.*, 1994, Phys. Rev. D **49**, 4348.
Gottfried, K., 1967, Phys. Rev. Lett. **18**, 1174.
Gribov, V. N., and L. N. Lipatov, 1972, Sov. J. Nucl. Phys. **15**, 438.
Gross, D. J., and C. H. Llewellyn Smith, 1969, Nucl. Phys. B **14**, 337.
Harris, D., *et al.* (CCFR Collaboration), 1995, in *Proceedings of the 30th Rencontre de Moriond*, FERMILAB-CONF-95-144.
Hasert, F. J., *et al.* (Gargamelle Collaboration), 1973, Phys. Lett. B **46**, 138.
Heagy, S. M., *et al.*, 1981, Phys. Rev. D **23**, 1045.
Hinchliffe, I., and C. H. Llewellyn Smith, 1977, Phys. Lett. B **70**, 247.
Holder, M., *et al.* (CDHS Collaboration), 1978a, Nucl. Instrum. Methods **148**, 148.
Holder, M., *et al.*, 1978b, Nucl. Instrum. Methods **151**, 69.
Jones, G. T., *et al.* (BEBC Collaboration), 1994, Z. Phys. C **62**, 601.
Jonker, M., *et al.* (CHARM Collaboration), 1982, Nucl. Instrum. Methods **200**, 183.
Kim, J. E., P. Langacker, M. Levine, and H. H. Williams, 1981, Rev. Mod. Phys. **53**, 211.
King, B. J., 1994, Ph.D. thesis (Columbia University), Nevis Report: Nevis-283, CU-390, Nevis Preprint R-1500.
Kodama, K., *et al.* (COSMOS Collaboration), 1993, "Muon-Neutrino to Tau-Neutrino Oscillations," Fermilab-Proposal P 803.
Krakauer, D. A., *et al.*, 1990, Phys. Lett. B **252**, 177.
Krakauer, D. A., *et al.*, 1992a, Phys. Rev. D **44**, R6.
Krakauer, D. A., *et al.*, 1992b, Phys. Rev. D **45**, 975.
Kramer, G., and B. Lampe, 1992, Z. Phys. C **54**, 139.
Krzywicki, A., 1976, Phys. Rev. D **14**, 152.
Lai, H. L., *et al.* (CTEQ Collaboration), 1997, Phys. Rev. D **55**, 1280.
Langacker, P., M. Luo, and A. Mann, 1992, Rev. Mod. Phys. **64**, 87.
Larin, S. A., and J. A. M. Vermarseren, 1991, Phys. Lett. B **259**, 345.
Leung, W. C., *et al.* (CCFR Collaboration), 1993, Phys. Lett. B **317**, 655.
Llewellyn Smith, C. H., 1983, Nucl. Phys. B **228**, 205.
MacFarlane, D., *et al.* (CCFR Collaboration), 1984, Z. Phys. C **26**, 1.
Marciano, W. J., and A. Sirlin, 1980, Phys. Rev. D **22**, 2695.
Martin, A. D., R. G. Roberts, and W. J. Stirling, 1993, Phys. Lett. B **306**, 145.
Martin, A. D., R. G. Roberts, and W. J. Stirling, 1996, Phys. Lett. B **387**, 419.
McFarland, K. S., *et al.* (CCFR/NuTeV Collaboration), 1995, Phys. Rev. Lett. **75**, 3993.
McFarland, K. S., *et al.* (CCFR/NuTeV Collaboration), 1997, "A Precision Measurement of Electroweak Parameters in Neutrino-Nucleon Scattering," FNAL-Pub-97/001-E.
Mishra, S. R., *et al.* (CCFR Collaboration), 1989, Z. Phys. C **44**, 187.
Mishra, S. R., *et al.* (CCFR Collaboration), 1990, Phys. Lett. B **252**, 170.
Mishra, S. R., and F. Sciulli, 1989, Annu. Rev. Nucl. Part. Sci. **39**, 259.
Morfin, J., *et al.*, 1981, Phys. Lett. B **104**, 235.
Mueller, A. H., and J. Qiu, 1986, Nucl. Phys. B **268**, 427.
Nachtman, O., and H. J. Pirner, 1984, Z. Phys. C **21**, 277.
Nikolaev, N. N., and B. G. Zakharov, 1975, Phys. Lett. B **55**, 397.
Novikov, V. A., L. B. Okun, and M. I. Vysotsky, 1993, Phys. Lett. B **298**, 453.
Oltman, E., *et al.* (CCFR Collaboration), 1992, Z. Phys. C **53**, 51.
Paschos, E. A., and L. Wolfenstein, 1973, Phys. Rev. D **7**, 91.
Perkins, D. H., 1975, in *Proceedings of Symposium on Lepton and Photon Interactions at High Energies* (Stanford University, Stanford, CA) p. 571.
Peterson, C., D. Schlatter, I. Schmitt, and P. M. Zerwas, 1983, Phys. Rev. D **27**, 105.
Pirner, H. J., and J. P. Vary, 1981, Phys. Rev. Lett. **46**, 1376.
Plothow-Besch, H., 1993, Comput. Phys. Commun. **75**, 396.
Pumplin, J., 1990, Phys. Rev. Lett. **64**, 2761.
Quintas, P. Z., *et al.* (CCFR Collaboration), 1993, Phys. Rev. Lett. **71**, 1307.
Rabinowitz, S. A., *et al.* (CCFR Collaboration), 1993, Phys. Rev. Lett. **70**, 134.
Reines, F., H. S. Gurr, and H. W. Sobel, 1976, Phys. Rev. Lett. **37**, 315.
Renton, P. B., 1995, in *Proceedings of 1995 Symposium on Lepton Photon Interactions*, Beijing, China (World Scientific, Singapore), p. 35.
Reutens, P. G., *et al.* (CCFR Collaboration), 1990, Z. Phys. C **45**, 539.
Romosan, A., *et al.* (CCFR/NuTeV Collaboration), 1997, Phys. Rev. Lett. **78**, 2915.
Ross, G. G., and R. G. Roberts, 1994, Phys. Lett. B **322**, 425.
Sakamoto, W., *et al.* (CCFR Collaboration), 1990, Nucl. Instrum. Methods Phys. Res. A **294**, 179.
Sandler, P. H., *et al.* (CCFR Collaboration), 1993, Z. Phys. C **57**, 1.
Sather, E., 1992, Phys. Lett. B **274**, 443.

Seligman, W. G., 1997b, Ph.D. thesis (Columbia University), Nevis Report-292.
Seligman, W. G., *et al.* (CCFR Collaboration), 1997a, Phys. Rev. Lett. **79**, 1213.
Sidorov, A. V., 1996, preprint JINR-E2-96-254, e-print archive: hep-ph/9607275.
Stuart, R. G., 1987, Z. Phys. C **34**, 445.
Taylor, G. N., *et al.*, 1983, Phys. Rev. Lett. **51**, 739.
Ushida, N., *et al.* (E531 Collaboration), 1988a, Phys. Lett. B **206**, 375.
Ushida, N., *et al.* (E531 Collaboration), 1988b, Phys. Lett. B **206**, 380.
van der Bij, J. J., and G. J. van Oldenborgh, 1991, Z. Phys. C **51**, 477.
Varvell, K., *et al.*, 1987, Z. Phys. C **36**, 1.
Vilain, P., *et al.* (CHARM II Collaboration), 1993, Phys. Lett. B **302**, 306.
Vilain, P., *et al.* (CHARM II Collaboration), 1994a, Phys. Lett. B **335**, 246.
Vilain, P., *et al.* (CHARM II Collaboration), 1994b, Phys. Lett. B **320**, 203.
Vilain, P., *et al.* (CHARM II Collaboration), 1994c, Phys. Lett. B **332**, 465.
Vilain, P., *et al.* (CHARM II Collaboration) 1996, CERN preprint CERN-PPE/96-01.
Virchaux, M., and A. Milsztajn, 1992, Phys. Lett. B **274**, 221.
Whitlow, L. W., *et al.*, 1990, Phys. Lett. B **250**, 193.
Whitlow, L. W., *et al.*, 1992, Phys. Lett. B **282**, 475.
Winter, K., 1990, Editor, *Neutrino Physics* (Cambridge University Press, Cambridge, England).
Yang, U. K., *et al.* (CCFR Collaboration), 1996, J. Phys. G **22**, 775.